ISTITUTO ITALIANO
DI TECNOLOGIA

POLITECNICO
MILANO 1863

DOCTORAL PROGRAM IN PHYSICS

XVIII cycle

Titanium dioxide hierarchical nanostructures for photonic applications

Ph.D. candidate:
Luca Passoni

Supervisor:
Dr. Fabio Di Fonzo
Tutor:
Prof. Guglielmo Lanzani
PhD Coordinator:
Prof.ssa Paola Taroni

December 2015

a Gae, Giusi, Peppa e Rigo,
a i miei genitori

CONTENTS

APPLICATIONS OF NANOSTRUCTURED TITANIUM DIOXIDE

CONCLUSIONS

METHODS

Preface

The content of this *PhD thesis* was partially published during the 3 years of PhD in scientific peer reviewed international journals. It is the result of the work done by *Luca Passoni* during the whole PhD program in collaboration with international institutions and industries. In this thesis the published contents are reported together with new unpublished results under a novel perspective. In the case a particular interest is raised by a part of this thesis, the candidate suggestion is to complement the reading with the list of publications reported below. There the reader will find detailed literature reviews about specific application of the treated materials and comparative analysis with the state-of-the-art in the respective fields.

List of publications
2015:

- *L. Passoni, F. Giordano, S.M. Zakeeruddin, M. Grätzel, F. Di Fonzo*
  Hyperbranched Self-Assembled Photoanode for High Efficiency Dye-Sensitized Solar Cells, *RSC Advances*

- *L. Criante, F. Di Fonzo, F. Fumagalli, G. Lanzani, L. Passoni, F. Scotognella, F. Simoni*
  Periodic nanostructures for tunable thin optics, *SPIE Proceding*

- *S. Varo, L. Criante, L. Passoni, A. Dalle Vedove, E. Aluicio-Sarduy, F. Di Fonzo, G. Lanzani, F.Scotognella*
  Control of the chemiluminescence spectrum with porous Bragg mirrors, *Advanced Device Materials*

- *A.Ghadirzadeh, L. Passoni, G. Grancini, G.Terraneo, A. Li Bassi, A. Petrozza, F. Di Fonzo*
  Hyperbranched Quasi-1D TiO2 Nanostructure for Hybrid Organic-Inorganic Solar Cells, *ACS Appl Mat.& Inter.*

2014:

- *L. Passoni, L. Criante, F. Fumagalli, F. Scotognella, G. Lanzani, F. Di Fonzo*
  Self-Assembled Hierarchical Nanostructures for High Efficiency Porous Photonics Crystals, *ACS Nano*

- *L. Passoni, G. Bonvini, A. Luzio, A. Facibeni, C. E. Bottani, F. Di Fonzo*
  Multiscale Effect of Hierarchical Self-Assembled Nanostructures on Superhydrophobic Surface, *Langmuir*

2013:

- *F. Di Fonzo, L. Passoni, L. Criante, F. Scotognella, F. Fumagalli*
  Fabrication Method for one dimentional photonic crystals
  TO2013A000975 November 29th, 2013
- *L. Passoni, F. Ghods, P. Docampo, A. Abrusci, J. Martí-Rujas et. al.*
  Hyperbranched Quasi-1D Nanostructures for Solid-State Dye Sensitized Solar Cells, *ACS Nano*

Prologue

"[…] I would like to describe a field, in which little has been done, but in which an enormous amount can be done in principle. This field is not quite the same as the others in that it will not tell us much of fundamental physics (in the sense of, "What are the strange particles?") but it is more like solid-state physics in the sense that it might tell us much of great interest about the strange phenomena that occur in complex situations. Furthermore, a point that is most important is that it would have an enormous number of technical applications. What I want to talk about is the problem of manipulating and controlling things on a small scale. […]"

From: There's plenty of space at the bottom
Richard P. Feynman
Caltech December 29, 1959.

The seminar "*There's plenty of space at the bottom*" held in 1959 by Richard Feynman,[1] from which the text above was extracted, is considered the first lecture on nanoscience. It was the first time nanoscience was described as a new and independent *field.* The pioneering and most remarkable aspect that made this talk a milestone in science and technology, was the fact that Feynman was the first to recognize and to join a set of phenomena under a common motive; they were all caused by a precise and *small* scale modification of their constituents. He also envisioned the general potential that a field in which the ability of "*manipulating and controlling things on a small scale"* would have been the source of advancement in a myriad of application.

Nano-materials however dates back to the 4th century A.D. when the Romans fabricated a glass cup, today exposed at the British museum (Lycurgus cup),[2] presenting peculiar optical properties that could change the colour depending on the incident light. It was only in the fifties' that thanks to advanced characterization techniques such as X-ray spectroscopy and transmission electron microscopy, gold and silver nanoparticles (and other materials) with characteristic size in the range of 50 nm were found to be responsible for this effect. The *Damascus* steel is another examples coming from the 13th century.

It gained a place in the history for its exceptional strength, resilience and to its ability to hold a sharp edge. [3] Today it is known and its properties were due to the inclusion of carbon nanostructures.

From observations of these and other phenomena, starting with the cited talk by Feynman, the scientific community has grown its awareness of the great potential that the science of the small can contribute to control fundamental material properties and perhaps to discover, and eventually control, phenomena that are yet to be observed.

After decades of fundamental research, nanoscience is now leaping into nano*technology.* This fading transition is driven by the fact that advanced techniques allow to control and characterized materials and to fabricate devices with properties enabled by nanomaterials. More and more products have been developed with increasing complexity. The initial employment of nanomaterials in paints, toothpastes and sunscreens has now moved to complex systems such as sensors, electronics and energy conversion devices.

Abstract

The work presented in this Ph.D. Thesis deals with the study of titanium dioxide hierarchical nanostructures fabricated by pulsed laser deposition (PLD) and some of their applications in the field of photonics. PLD technique is a bottom-up and room-temperature fabrication process that allows to transfer a material, evaporated through a focused pulsed laser beam, on another substrate. The process takes place within a vacuum chamber where the pressure is set-constant through the flux of a gas. The morphology of the transferred material can be engineered at the nano as well as at the micro-scale. In the first part of the Ph.D. Thesis PLD process is described. With scanning electron microscopy (SEM), Brunauer–Emmett–Teller (BET) and Barrett-Joyner-Halenda (BJH) techniques, the material structure and its dependence on deposition conditions is studied. In a certain pressure range it is shown that columnar and hierarchical nanostructures are formed. These are formed by nanometric clusters attached to larger structures departing from a main elongated trunk. While the nanometric features comprised within these structures are adjusted through pressure tuning, it is observed that it is possible to achieve high density and high specific surface area. The two latter characteristics contribute to the increase in the ratio of the effective over geometric surface area (roughness factor, RF) as it is confirmed by specific measurements. Upon thermal treatment crystallization can be induced. It is shown that, during crystallization, an energy minimization process eliminates high energy crystal facets imposing an anisotropic crystal growth and leading to hyperbranched structures with crystals as long as several tens of nanometers. The crystallization process is directly studied by X-ray diffraction and Raman spectroscopy as it evolves in time and with increasing temperature. Once again the crystallization carries structural modifications, such as densification due to Ostwald ripening, that are studied through the above mentioned methods. A change in surface to volume ratio is observed and it is responsible for a densification of the top part of the films. Individual nanostructures collapse on each other creating a "dry mud effect" on the surface of the deposited material also visible as micrometric cracks. The size of these is shown to be dependent on nanostructures height and density. As the morphology changes the effective refractive index of the

deposited film is affected. The latter characteristic coupled with the control over the deposition process gives the possibility to tune the photon-material interaction. In the second part of the Ph.D. Thesis it is shown how hyperbranced titanium dioxide can be employed to manage photon flux within photovoltaic devices, namely dye sensitized solar cells (DSCs). PLD nanostructures are shown to work as broadband light scattering elements and to enhance the DSC optical thickness. Long range anisotropic crystallinity improves charge transport. More efficient charge photo-generation and collection result in better photovoltaic performances. The optimization leading to this improvement is tested in systems with liquid electrolyte and solid polymeric hole transporting materials demonstrating how these structures can be beneficial for both systems. PLD versatility allowed the fabrication of a monolithic multi-stack of hyperbranched TiO_2, hierarchical Al_2O_3 and porous ITO. This multi-layered structure, once loaded with dye and infiltrate with a redox electrolyte is shown to work as efficient monolithic DSC with the same outstanding opto-electronical properties shown by the two above mentioned systems. The possibility of creating multi-layered structures, coupled with the periodic modulation of the effective refractive index, enables PLD as a tool for fabricating hierarchical one dimensional photonic crystals. The high surface area and interconnected porosity give to these photonic nanostructures advanced functionality envisioning optical sensors and other application in the field of optoelectronics. By physical masking it is possible to create pixels matrix as large as few microns paving the way to possible applications in the field of active matrix displays. Hierarchical photonic nanostructures are used to modulate photon flux with a DSC system decoupling the colour of the pigment used for the photovoltaic effect to the one of the overall device. Eventually, the fine control over PLD nanostructure morphology is employed to study transparent ultrahydrophobic materials thought to be useful for those application requiring self-cleaning properties.

Chapter 1

Introduction to titanium dioxide nanostructures

Titanium dioxide

Titanium dioxide, also known as titania, has been widely used in sunscreens,[4] pigments[5] and paints[6] since its commercialization in the early '20s. It is a metal oxide with a chemical formula TiO_2. Among its many advantages includes: a wide band-gap (rutile 3.0 eV and anatase 3.2 eV), high refractive index, high dielectric constant, as well as being inexpensive, abundant and non-toxic. [7] Since 1972 when *Fujishima and Honda* published their work on the mechanism of water splitting through the UV irradiation of TiO_2[8], titania has been widely investigated by the scientific community. Its outstanding properties, coupled with the possibility to manipulate its structure to make it interact with host materials such as other smaller band-gap semiconductors [9] or dyes, [10] led to the many application in the fields of photocatalysis,[11] photovoltaic[12] and sensors. [13]

It is clear that despite its interesting optical, electronic and structural intrinsic properties, nanoscience and nanotechnology are enabling its usage in a broader set of fields.[14] Size, shape and atomic configuration of nanomaterials are affecting their chemical and physical properties. Within nanomaterials, electron and holes move governed by quantum confinement and the transport of phonons as well as of photons can be controlled.

The surface-to-volume ratio can be precisely and broadly tuned boosting the number of reactions that exploits interfacial regions and enabling a wide set of technologies.

The methods used to synthetize titania nanostructures are many and can be incrementally combined to obtained more complex structures:

Sol Gel method	Hydrothermal method	Physical vapour dep.
Micelle method	Direct oxidation method	Electrodeposition
Microwave method	Chemical vapour dep.	Sonochemical methods

A complete review on the above mentioned methods can be found on reference 15. In the next paragraphs the structural, optical and electronic properties of titanium dioxide will be briefly described. Eventually a brief overview of TiO_2 nanostructures for photovoltaics and photonic applications

will be given. As the main application described in this *thesis,* as many other, involve the use of anatase, the focus will be on the properties this allotropic phase.

Structural and electronic properties

Anatase has a ditetragonal dipyramidal crystal structures resulting in twelve atoms and therefore four molecules per cell. Each titanium (Ti^{4+}) atom is surrounded by six O^{2-} atoms. Titanium is coordinated to six oxygen atoms and oxygen is coordinated to three titanium atoms. The resulting crystal structure of anatase TiO_2 are depicted in Figure 1.
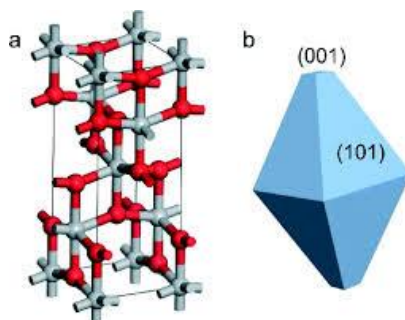

Figure 1 (a) Anatase TiO_2 crystal structure. Grey titanium atoms and red oxygen atoms. (b) Crystal shape of anatase TiO_2.[16]

The dipyramidal crystal shape is a result of a minimization in the surface free energy of the crystal facets. This is in turn related to the atomic arrangements of the facet itself. The 001 facet possesses a higher density of undercoordiantated titanium atoms compared to the 101 facet. [16] The average surface energy of 001 and 101 facets were calculated to be respectively 0.9 and 0.4 J/m^2. [17] Several studies were performed to control crystal facet exposure and thus material reactivity. [16, 18, 19] Despite rutile has always been regarded as the most stable crystal phase, the differences in free energy (~10 kJ/mole) between the three phases suggests that at normal pressures and temperatures also anatase is stable.[20] In anatase the octahedral units are slightly distorted resulting in a lower symmetry that effect material density and electronic properties. Each octahedron shares four corners and four edges and is thus coordinated with eight other

octahedral structures. As studied by *Jao van de Lagemaat et al.* [21] this coordination number is decreased in the case of nano-porous materials reaching values of 3 for porosity higher than 80 %. Several applications are benefitting from the higher surface reactivity given by the low coordination number characteristic of nanostructured materials.[22] The total and the ion decomposed electronic density of states, showing the 3.2 eV indirect band-gap of anatase, are reported in Figure 2.
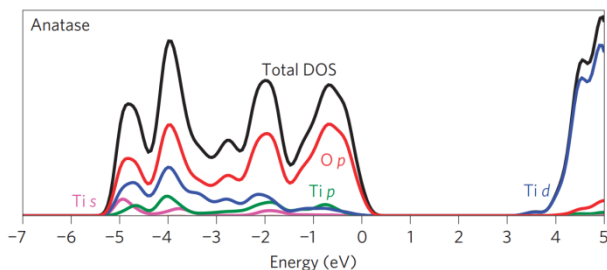
Figure 2 Electronic structure of anatase. [23]

Optical properties

In large band-gap indirect semiconductors light absorption is allowed only for photons with energy $h\nu \geq E_g + W_c$ (where E_b is the energy gap and W_c is the conduction band width). [15] In the specific case of titania, the band-gap above 3 eV allows absorption only in the UV region for wavelength below 350 nm. Below the transmission spectrum of a compact 100 nm thick TiO_2 fabricated by pulsed laser deposition is reported.

Figure 3 Transmittance spectrum of 100 nm thick compact film of titania anatase.

While energy gap determines the threshold energy required for a photon to be absorbed, the refractive index (n) represents another fundamental physical quantity related to the transparency of the material. [24] T.S. Moss in 1951 proposed an experimental relationship based on previous studies for which the product between n^4 times the energy gap was constant and equal to 95eV. [25] Since then a number of values and model have bee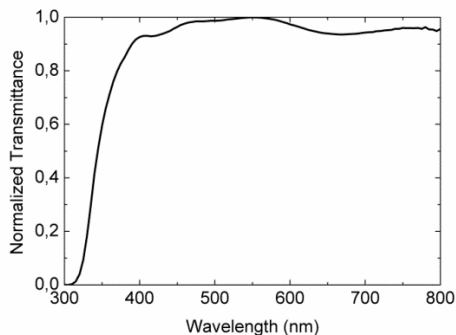n proposed.[26] As the energy gap is changing with crystallinity, the refractive index was also found to depend on the annealing temperature.[27] Anatase refractive index was measured by ellipsometer spectroscopy.[28] The dispersion relations of the real and imaginary components of the refractive index are reported in Figure 36.

Titanium dioxide nanostructures for dye sensitized solar cells

The possibility of modifying titanium dioxide morphology has boosted its potential applications. In particular, in the field of photovoltaic, titanium dioxide nanostructures have been used as scaffold material for dye molecules in dye sensitized solar cells (DSCs). These photovoltaic devices exploit the exciton formation occurring into the molecules of a dye chemisorbed onto a thin film of titanium dioxide upon light irradiation. Titanium dioxide has the role of hosting as many dye molecules as possible in order to maximise the charge generation and to favour charge transport once the electron is injected into it after exciton splitting. For a more detailed explanation of DSC working principles the reader is addressed to the *application* section. Below an overview of the main titanium dioxide nanostructures employed in dye sensitized solar cells.

Mesoporous nanoparticles

A mesoporous film comprising a random network of 20 nm large interconnected anatase nanoparticles is the standard choice for several applications due to their high specific surface area. For instance large uptake of dye molecules allow for high charge photogeneration in dye sensitized solar cells.[29] Besides working as dye scaffold and guarantee high optical absorption, anatase titania is the allotropic phase found to be the most efficient in terms of electron injection and transport. While this mesoporous

film, firstly introduced by Grätzel, was kept as standard reference, several architectures have been exploited to study the effects of morphology on the opto-electronic and photovoltaic performance of the device. As the first charge recombination phenomenon is due to electron trapping at the nanoparticle interconnection[30, 31], always increased interest is gained by elongated structures that offer a preferential pathway for electron transport minimizing nanoparticle-nanoparticle interfaces.

Nanotubes

Nanotubes are high aspect ratio hallow structures usually obtained by anodic etching. They offers vertical channels that allow dye and hole transporter infiltration.[32] The specific surface area is limited by their one dimensional structure. Nanotubes were used in the fabrication of DSCs with promising results. A complete review can be found at reference 33. To increase the surface area and therefore the dye loading, a bamboo-like array of nanotube was synthetized by changing cyclically the anodization voltage.[34] Nanotubes are obtained with a top-down approach, starting from a titanium sheet. For this reason, they are commonly seen as not applicable to transparent substrates. Recently however they were successfully anodized on flexible, light and transparent substrates making their application particularly suitable for photovoltaic and even portable applications.[35, 36]
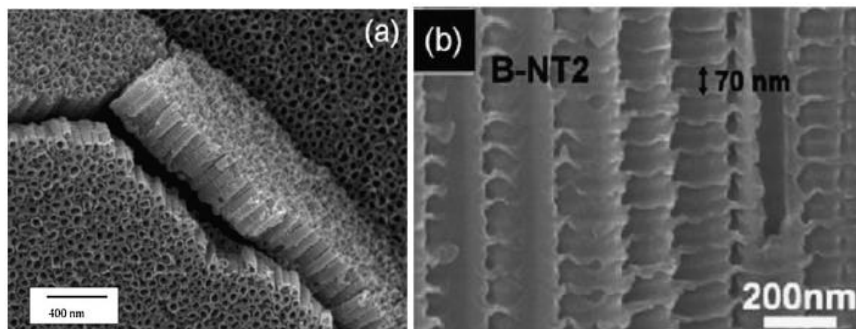

Figure 4 a) Nanotubes of TiO$_2$ and b) nanotubes bamboo-like for increasing surface area.

Nanowires and Nanorods

Nanowires present analogous characteristics of the nanotubes i.e. high but limited surface area and, due to their elongated shape favouring vectorial transport, good electron transport. Law M. et al. (2005) [37] estimated that the electron diffusivity of a single TiO_2 nanowire (D=0.05-0.5 cm^2s^{-1}) is several hundred times larger than highest electron diffusivity for simple TiO_2 nanoparticles.[38] Dye-sensitized solar cells were fabricated using both an ordered array of nanowires [37, 39] and a randomly assembled mesh.[40] In the first case nanowires are synthetized by hydrothermal treatment onto a FTO coated glass. In the latter case a colloidal suspension of nanowire was deposited on the substrate forming a thick nanorods mesh and resulting in an extremely rough surface. DSCs were fabricated using iodide-based redox mediator and sensitized with N719 dye leading to an efficiency of over 6.4%.[41]

200 nm
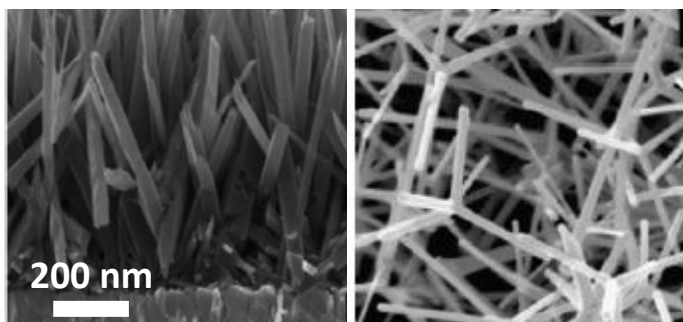
Figure 5 (left) Aligned Nanorods and (Right) Nanorods mesh.

Nanotrees and other 3D nanostructures

Quasi-one dimensional hierarchical structures are promising alternatives to the above solutions in order to fulfil the requirements previously highlighted, i.e. higher specific surface area to increase the active sites available for charge photogeneration, few inter-particle interfaces to avoid charge recombination and rough surface to enhance the light harvesting properties both through an increase in the chemisorbed dye and, through a more efficient light management given by the elements forming the film being large on the same order of magnitude of the incident light wavelength. Single hierarchical post can in fact scatter the light and enhance the optical path within the

photoactive layer. In this field nanotrees have shown interesting results as reported by *F. Di Fonzo et al.* (2010)[42]. Different densities and porosities, obtained by tuning the physical and chemical experimental conditions[43] , have been studied for their applications as photoanode in liquid electrolyte dye-sensitized solar cells and a trend in generated photocurrent and efficiency was found upon nanotrees morphology modification.[44] Just recently *S. H. Ko et al.* [45] presented a hierarchical architecture tree-like vertically aligned for high efficiency dye-sensitized solar cells. The nanotrees were grown using a hydrothermal growth approach.
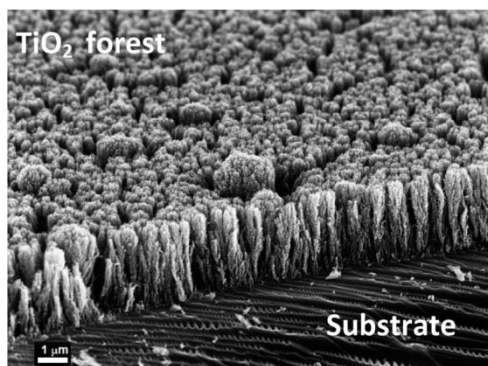
Figure 6 Hierarchical titanium dioxide nanostructures by pulsed laser deposition

Modified nanostructures for DSC

In the case of one dimensional materials to overcome the issue related to the low specific surface area nanowires [46] were decorated with smaller nanoparticles leading to a significant increase in the overall efficiency [47] from 1.58% to 4.24% and stressing further on the crucial role played by the high specific surface area.

Reducing charge recombination is important to enhance the photogenerated current and the open circuit voltage. For this purpose a core-shell morphology has been adopted by applying a barrier layer around the mesoporous structure. This shielding is done to retard the back electron transfer and therefore requires that the shell material has a more negative

conduction band compared to the core material. Materials such as Nb_2O_5, Al_2O_3, SnO_2 or $SrTiO_2$ have been tested. Nb_2O_5 gave better result with an increase in photocurrent, open circuit voltage and fill factor leading to an overall efficiency increase of 37% [48, 49].

Another method for light conversion energy devices, reviewed in by *Linic S. et al.* (2011)[50], exploits the plasmonic effect by decorating the mesoporous substrate with noble metals nanoparticle to enhance the photocatalytic efficiency of titanium dioxide and the electron injection. Significant improvement of over 25% were reported using silver nanoparticles thanks to surface plasmon resonance.[51] This technique has been also combined with the core-shell technique described above for the fabrication of dye-sensitized solar cells with a remarkable beneficial effect in terms of short circuit current density and overall efficiency [52].

Aim of the Work

In this *Thesis* the aim is to study how it is possible to tailor the structure of quasi-1D nanomaterials by physical vapour deposition to obtain useful materials in the field of photonic. In particular titanium dioxide, fabricated by pulsed laser deposition (PLD), and its morphological properties is studied. In the next chapter (*Nanostructured materials by pulsed laser deposition*) it is shown to what extent titanium dioxide morphology can be controlled by tuning experimental parameters in PLD set-up. The understanding and control over material properties is shown to be crucial for several photonic applications as it is shown in the chapter entitled *Application of nanostructured titanium dioxide.*

Chapter 2

Nanostructured materials by pulsed laser deposition

Pulsed laser deposition

Pulsed laser deposition (PLD) is a physical vapour deposition technique and it is in first approximation a simple method that involves the collection of the material ejected from a solid target irradiated by a pulsed laser. It allows transferring the stoichiometry of the source material on thin films that can be digitally controlled in thickness and density by tuning laser radiation and ambient conditions. The pulsed laser is focused within a vacuum chamber on the target material that absorbs photons and that is rapidly heated. Above a threshold laser power density, which depends on laser wavelength and on the physical-chemical characteristics of the target material, the target melts and eventually vaporizes. At this stage the strong electromagnetic radiation carried by the laser is coupled with the electrons of the target materials and a plasma is formed due to dielectric breakdown. [53] The plasma containing neutrals, ions, electrons and clusters expands away from the target along the major density gradient (between the melted material and the outer environment). [54] The expansion of the so called plasma *plume,* projects the ablated species at supersonic velocity. [55] After colliding among themselves and with the ambient gas they impact on the substrate that is placed face-on to the irradiated target material. Within a broad cone of angle acceptance the direction of the plasma plume expansion was shown to be perpendicular to the target. [56]
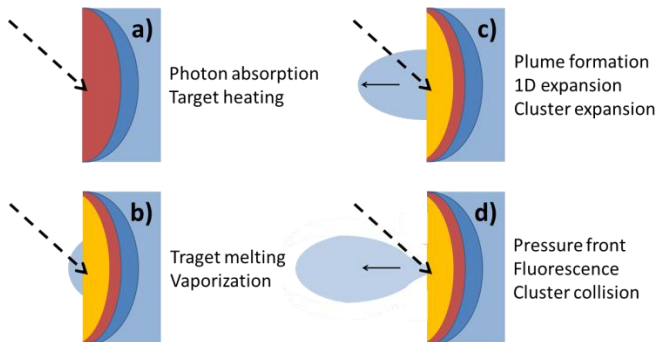

Figure 7 a) the laser is absorbed by the target material that is heated. b) The materials reach its melting temperature and a plasma forms on the surface. c) The plasma is accelerated away from the target due to density gradient.

d) The clusters contained in the plume meet a pressure front and reach the samples.

The pulsed nature of the deposition by PLD allows the control of the cluster diffusivity on the surface and other kinetic parameters. The laser pulse, in many cases few tens of nanoseconds long, initiates a plasma of ablated clusters that lasts for several microseconds. The actual deposition of the ablated material, when nucleation and growth takes place, instead occurs for a longer period of time between two pulses.[57]
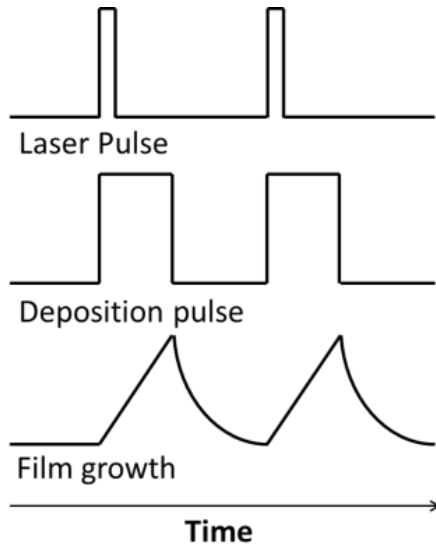
Figure 8 Schematic of pulsed laser deposition time evoultion

The plasma plume dynamics and the ablated species kinetics are determining the characteristics of the thin film formation. They involve diverse and interconnected phenomena and are affected by laser fluency, pulse duration, laser wavelength, target material properties and background gas composition and pressure. The deposited thin film possesses the typical thickness contour of thermal evaporated thin film ($cos\vartheta$) with a more peaked deposit. The profile can be fitted with a $cos^n\vartheta$, with 4 < n < 15. [58, 59] In the set-up used for the work object of this *thesis,* an KrF excimer laser, Coherent COMPexPro 200, (λ = 248 nm, pulse duration ~ 20 ns, maximum energy per pulse 700 mJ)

is focused by a 500 mm focal distance lens and directed through a quartz window in a vacuum chamber. The chamber is equipped with a vacuum system comprising a scroll pump and a turbomolecular pump that allow base vacuum in the order of 10^{-3} Pa. Through an inlet connected to MKS mass flow meters the chamber can be fluxed with any gas and the working pressure can increased from the base pressure and can be kept constant up to several hundreds of Pascals. The pulsed excimer laser is impinging on a target of the source material.
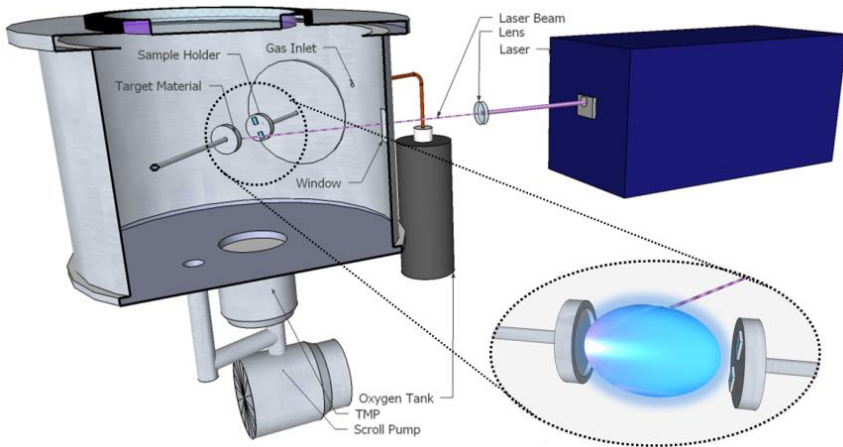
Figure 9 Schematic of the pulsed laser deposition set-up used in this *thesis*

The target is attached to a motion system connected through gearing to step-motors with magnetic liquid rotary sealing mechanism allowing fast movements. This prevents the laser to hit twice the same target spot reducing defects in the thin film formation. The movement is controlled by a custom made LabView software that impose a Archimedean spiral motion with a vertical translation to the target. Samples are place face-on to the target and the target to sample distance can be regulated from 0 to 250 mm. The sample holder is shifted off-axis with respect to the plasma plume and it is rotated (10 rpm) in front of it to increase the deposit uniformity. The tangential velocity of the samples with respect to the plasma plume is 2 cm per second. This way the area of uniformity is enlarged as schematically explained in the figure below. As previously mentioned, the characteristics

(namely the morphology and the stoichiometry) are strongly affected by several factors. In this work the pressure of the gas present in the deposition chamber was used to tune the ablated species kinetics and in turn morphology.
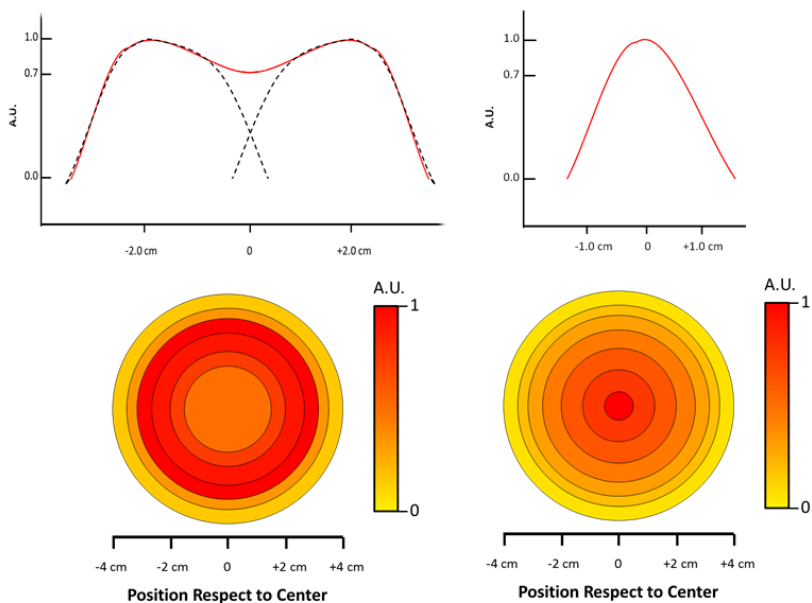

Figure 10 Thickness contour of the deposit (left) in the case of off-axis substrate movement and (right) in the case of centered substrate placed statcily in front of the plasma plume.

Titanium dioxide

Morphology and structural modification *versus* deposition background gas pressure

Controlled clustering and landing

The species ablated from the titanium dioxide target by the excimer layer, condense on the sample that are placed face-on to the expanding plume. A thin film is formed. The background gas is varied to induce clustering in the expanding plume, as described in the methods section. This is in turn affects the kinetic energy and the deposition mechanisms of the nanoparticles. As a consequence the pressure modulation controls the morphology of the deposit. In particular, in certain processing window, [60] the ejected clusters scatter on themselves and on the working gas, causing a reduction in their energy and a self-assembling in quasi-1D nanostructures. These are ordered in an array perpendicular to the surface of growth. Their typical diameter is in the range of hundreds of nm and their heights can be digitally controlled by setting a specific number of pulses (*i.e.* deposition time). [61, 62] Film obtained at different background pressures are shown below.
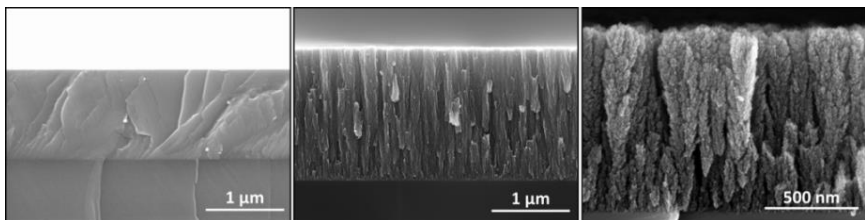
Figure 11 TiO$_2$ film deposited by pulsed laser deposition at 2, 5 and 20 Pa in oxygen.

As briefly described in the previous paragraph (*Pulsed laser deposition*) in this *Thesis,* the sample holder is place of axis with respect to the plasma plume and it is rotated to induce a linear velocity of the samples passing in front of the deposition area. Besides increasing the area of uniformity from few square millimeters to few square centimeters, this process allows access to a new growth mode that permit to obtain, even at lower pressures, dense and high surface area photoanodes, while maintaining the hierarchical structure.

Since the deposition angle at each point of the sample is continuously changed by the substrate rotation, a self-shadowing effect, that is naturally occurring in PLD high pressures process where high porosity film are formed, occurs also at lower pressures. For this reason the density that characterizes low pressure deposits can be coupled to the typical porosity of hierarchical nanostructures. This growth mechanism resembles the one of Glancing Angle Deposition. [63] However the need of high tilt angles and of sophisticated substrate motion control is no longer in place as a simple rotation suffices.
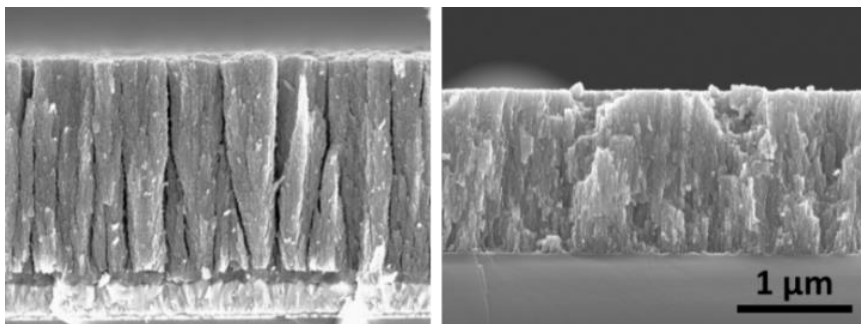

Figure 12 (Left) a film of TiO2 deposited at 7 Pa in an oxygen atmosphere moving the samples with respect to the plasma plume with a linear velocity of 2 cm/s and (right) a deposit of titanium dioxide obtained in the same condition as the former one but keeping the sample in a static condition.

In sum, the working gas pressure within the deposition chamber is used as primary morphology control parameter while the substrate rotation extends towards lower pressures the process window where it is possible to obtain hierarchical structures. In fact, similarly to previous works,[64, 65] with a stationary substrate holder, the background gas pressure at which the transition between low (dense) and high (hierarchical) surface area titanium dioxide films is set around 10 Pa in O_2. This is due the kinetic energy of the expanding species and reduced self-shadowing effect. In the case where the substrate is moved, the transition from dense to porous film shifts around 5 Pa, and at 7 Pa the film is already hierarchical. The rotating substrate lowers this threshold and the dense hierarchical structures are obtained down to 6 Pa. For very high pressures, the ablated species scatters among themselves and with the background gas molecules and form large clusters in gas phase.

These, diffusing through the background gas to the substrate, form highly disordered materials typical of low energy deposition processes.[66] This becomes clear looking at the opposite trend followed by the films density and their respective specific surface area (SSA) values measured by Brunauer–Emmett–Teller (BET) and by Barrett-Joyner-Halenda (BJH) technique and reported in Figure 13 below (see methods).
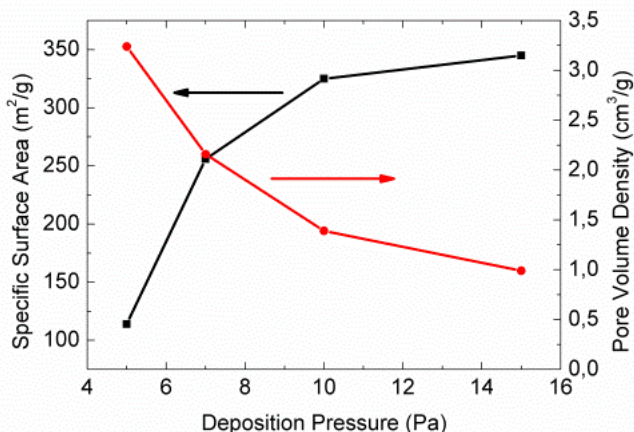
Figure 13 Specific surface area of film deposited at different pressure and their respective densities.

The SSA increases meaning that an higher surface to volume ratio is present. This is also due to more disordered structures as well as to an increase of voids that exposes material surface (lower density). The way nanoclusters are packed together is therefore changed. While the morphology of the film across thickness is affected as shown in the cross sectional SEM images, its surface is also modified. As reported in literature,[67, 68] the surface roughness is increasing with deposition pressure. This feature reflecting the disordered nature of films deposited at high pressure is also confirmed by AFM measurements reported below. For experimental consistency AFM measurements are performed on thin samples having the same thickness of 100 nm. Thickness is chosen to be low in order to reduce possible secondary effects arising at higher scale that could perturb the surface roughness. The scan area is chosen small enough to rule out possible defect occurring on

higher length scales. It is therefore now clear that during deposition, ablated atoms, aggregate in clusters upon scattering within themselves and with the background gas molecules.

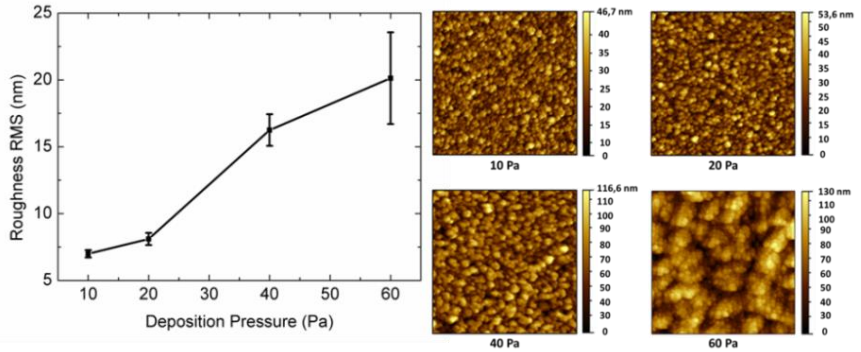**Figure 14 Roughness (RMS) measurements by atomic force microscopy performed on 100 nm thick samples deposited at different pressure by pulsed laser deposition**

At low pressure their energy allows the reorganization in compact and dense films while at high pressure the nanostructures composing the film are disordered and rare. More importantly there is a pressure range between these conditions where dense but still nanostructured morphology is present.

Morphology and structural modification due to thermal annealing

The Full changes the Void

In the previous section was described how the morphology can be determined on flight, by the ablated species aggregation after ablation and by the nanocluster kinetic energy once they have reached the sample substrate. In other words, the atoms arrangement is in that first stage controlled by controlling their kinetic energy throughout the plasma plume expansion and during its recondensation on the substrate. Once nanostructured films are formed, they are characterized by titanium dioxide in its amorphous phase and no kinetic energy is leftover. To further arrange the atoms with the quasi 1D nanostructures additional energy has to be provided. Thermal energy can be provided through thermal treatments to further reorganize the atoms into more stable or even crystalline structures. In the specific case of titanium dioxide, it is known that upon thermal treatment, above 350-400 °C [25] the

thermal energy is enough to permit the reorganization of atoms into a polycrystalline anatase matrix. To investigate the consequence of nanostructure crystallization on PLD nanostructures, a 2 hours thermal treatment at 500°C in air is used as first annealing condition. With this process, which ensures titanium dioxide crystallization, the morphology change of samples deposited at different background gas pressure is investigated. From BET analysis, it is clear that the atoms, reorganized into crystals and thus changing their surface to volume ratio, lead to a reduction in specific surface area (Figure 15). As previously discussed for amorphous materials, the density is still decreasing with pressure. With this in mind, in order to account for this opposite trend in the description of the material and of its surface it is worth to introduce a parameter that can describe the surface area accounting for the density of the material. The sample effective surface area in this case represents a straightforward figure of merit to determine the amount of area that can be exposed to the outer environment in a unit volume (sample geometric area over its film thickness). This is the roughness factor per unit thickness (RF), *i.e.* the ratio between effective and geometric surface area per unit of film thickness. It is affected simultaneously by the specific surface area (area per unit weight) and by the material density that determines how much material per unit volume is present. As briefly mentioned above, in the case of pulsed laser deposition materials, the quantity of surface per unit volume increases with the specific surface area as long as the density becomes too low.
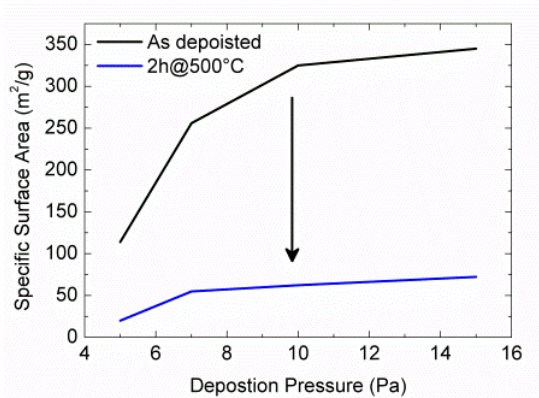
Figure 15 Reduction in SSA of samples as deposited and after 2 hours thermal annealing at 500°C in air.

At that point despite the increase in SSA, the quantity of material present in the considered volume will be very low and overshadows the increase in SSA. In Figure 16 the RF_{dye} measured directly by chromatographic analysis of the dye (N719) desorbed from the surface (see methods) is compared with RF_{BET} obtained multiplying the density and the SSA measured by BET method.
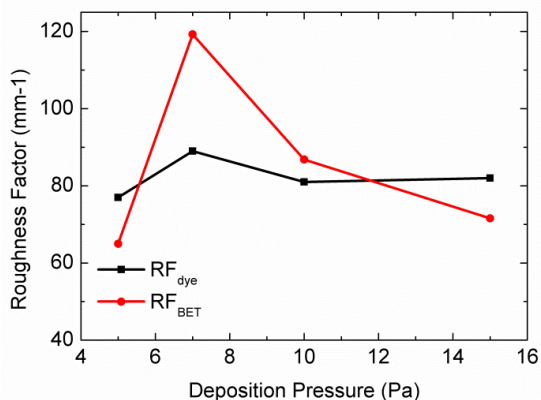
Figure 16 Roughness factor (RF_{dye}) measured by chromatografic analysis and (RF_{BET}) calculated from BET measurements.

RF_{dye} is expected to be always lower than RF_{BET} since, due to the large difference in probe size, dye and N_2 respectively, not all the surface accessible

to N_2 is accessible to the dye. The PLD nanostructures are characterized by a porosity comprising: (i) *channels* between the elongated nanostructures, (ii) voids between branches that are radially departing from the main vertical structures and (iii) eventually inter-particles spaces. While micrometric pores are clearly visible in the cross-section SEM images, nanometric pore size distribution is reported in Figure 17. Black curves show the pore size distribution of as deposited samples. As the pressure increases, the overall porosity (area underneath the curves) increases and the curve broaden towards larger pores diameters. From the graphs in Figure 17, it becomes clear that as the samples are treated at 500°C (i) the distribution peak moves to larger pore diameters and (ii) the overall pore volume (*i.e* the integral of the curves.) diminishes. As expected the atoms reorganize in bigger clusters (or crystals, as it will be shown further on) completely changing the pores configuration.
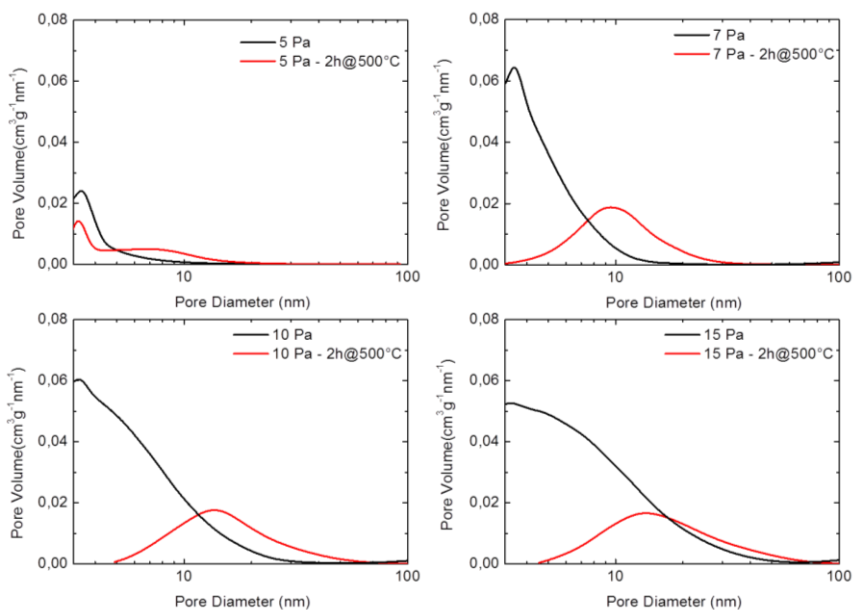

Figure 17 Pore size distribution for four samples deposited at different background gas pressure before (black) and after (red) thermal treatment.

The smaller pores are suppressed and the overall porosity is decreased as shown in Figure 18 right-hand side possibly due to suppression of inter-particles nanometric voids.
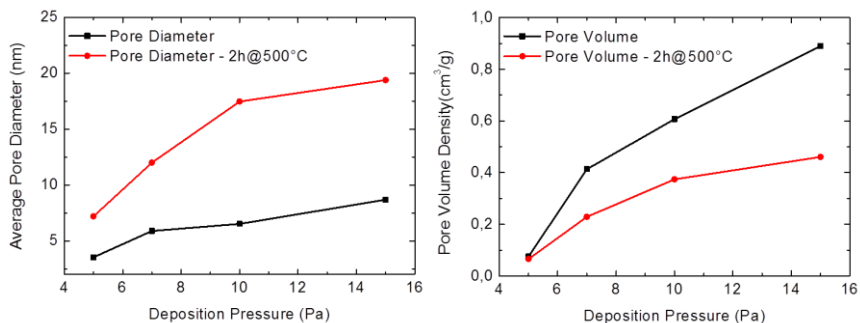
Figure 18 Values calculated from the BET analysis. (Left) Average pore diameters and (Right) overall pore volume density for samples deposited at different pressure before and after thermal treatment

On the contrary, but exactly for the smaller pores elimination, the average pore size is augmented. As it could have been expected, materials deposited at higher pressures do show a larger transformation especially regarding the overall pore volume. Indeed as the deposition pressure increases the nanostructures become more complex and their consequent reorganization is more significant.

Rearranging atoms in different nanostructures

The X-ray diffraction (XRD) after two hours thermal annealing at 500°C spectra of TiO_2 films are as shown in Figure 19. As expected given the annealing temperature, the titanium dioxide has turned in the anatase allotropic phase. More interestingly, the peak intensity ratio of (004) to (101) in XRD spectrum of anatase is equal to 1.19, 0.56 and 0.33 for the samples deposited at 7, 10 and 20 Pa that. These values if compared to the value of 0.20 relative to crystalline powder, are a clear indication of the preferential growth along the [004] direction.[19] The preferential growth along the *c* axis shown by XRD analysis is increasing with increasing film density (*i.e.* decreasing deposition pressure).
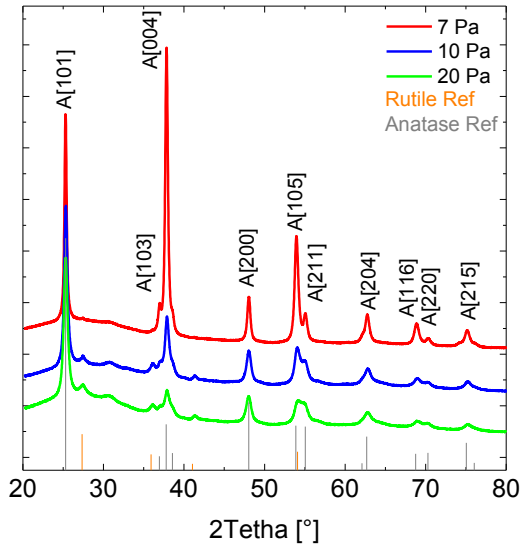
Figure 19 X-Ray diffraction spectroscopy for nanostructured samples showing high porosity and hierarchical nanostructures

The anisotropic growth along [004] is thought to be a phenomenon arising in order to allow the achievement of a minimum in the total free energy during crystallization in a mechanism similar to oriented attachment.[19, 69] The high film density in the case of the PLD 7 Pa sample allows primary crystal seeds to undergo a free energy minimization process which does not occur in the case of less dense morphology (higher deposition pressures).

Hyperbranching [70]

Figure 19 shows through XRD peak intensity analysis that a strong preferential growth along the *c* axis is present on hierarchical nanostructures deposited at 7 Pa. For this reason here after the analysis will be focus on this sample in order to reveal other features of this material. Transmission Electron Microscope (TEM *JEOL 4000EX* at 400 kV) images of the TiO_2 film deposited at 7 Pa are reported in Figure below. The high resolution TEM images show well that the nanostructures are actually hyperbranched in the sense that long and crystalline branches are splaying from the main vertical trunk of the structure. Highly resolved lattice fringes are present also at the outer surface, confirming the high crystallinity of the branches. The lattice constants in the

parallel and perpendicular directions to the length of the branches are respectively 9.39 and 3.74 Å, suggesting that the branches are also single-crystalline tetragonal-anatase phase TiO_2 growing along the [004] direction.[71]
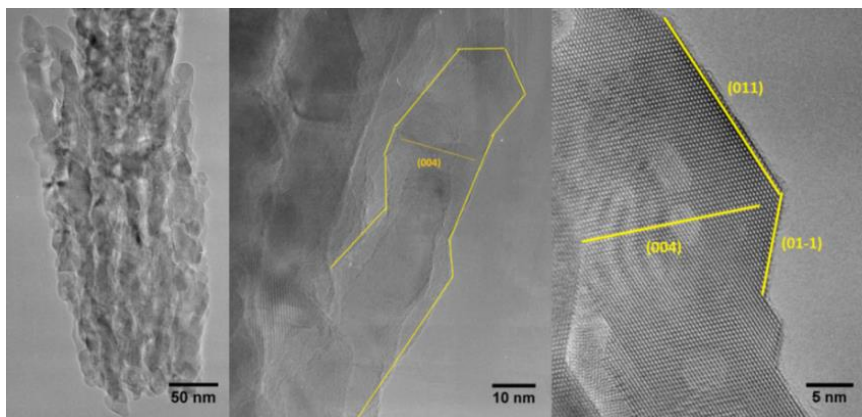
Figure 20 High resolution TEM images of PLD deposited film at 7 Pa. Here is possible to appreciate the hyperbranced structures (left-hand side), the single crystal branches (centre) and the preferential growth (right-hand side)

TEM and high resolution TEM images have shown single crystalline branches developing in the *c* direction with a characteristic size of 50 to 100 nm confirming the preferential growth already highlighted in Figure 19 reporting the XRD spectrum.

How they become crystalline: can they be tuned?
The atomic reorganization in nanocrystalline domains occurring in the PLD nanostructures as a consequence of the thermal energy fed during thermal annealing here is further explored on the samples deposited at 7 Pascal. This is to understand (i) how do the crystal growth evolve and (ii) if it can be controlled and to what extent.
In a first experiment the duration of thermal treatment is changed in order to investigate the dynamic of the crystallization process of hierarchical titanium dioxide. The temperature is kept at 500°C while samples are annealed for 1, 30, 60 and 120 minutes.
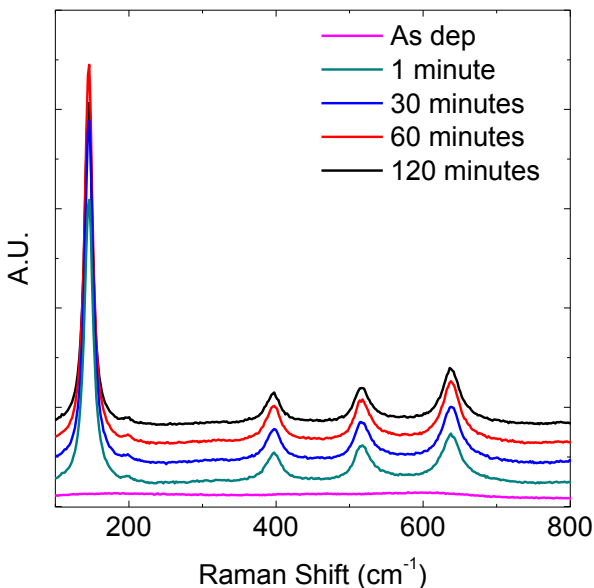
Figure 21 Raman spectra of samples deposited at 7 Pa and thermally annealed at 500°C in air for different time.

All the spectra reveal that, independently of the annealing time, the allotropic phase into which titanium dioxide is found after annealing at 500°C is anatase. This is expected as the atomic reorganization into a given crystalline structure it is prompted by a threshold (thermal) energy. Longer exposure time to thermal energy could play a crucial role in (i) determining the distance over which the atomic order induced by the thermal energy is affecting the structure and (ii) could highlight crystallization processes that at those temperature have a slow kinetic. In other words even if the crystalline phase it is initiated when a certain energy is provided, the crystalline structure evolve in time. This become clear in the XRD spectra reported below (to assign peak to crystalline facet please refer to Figure 19). The peaks related to anatase are present in all samples confirming the results obtained by Raman spectroscopy.
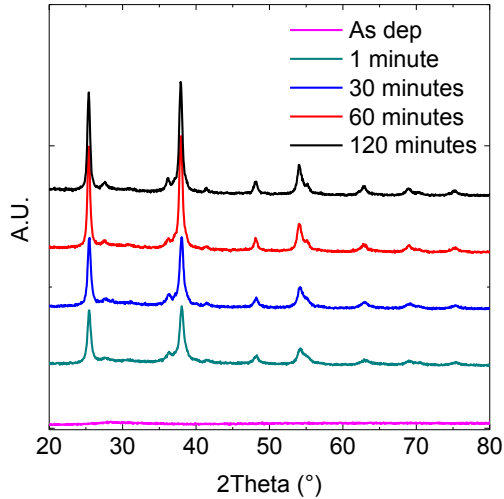
Figure 22 XRD spectra of samples deposited at 7 Pa and thermally annealed at 500°C in air for different time.

With a more accurate analysis it is possible to notice that the FWHM of XRD peaks is decreasing. This is an indication of the formation of larger crystalline grains as predicted by Scherrer's equation presented in the methods section.
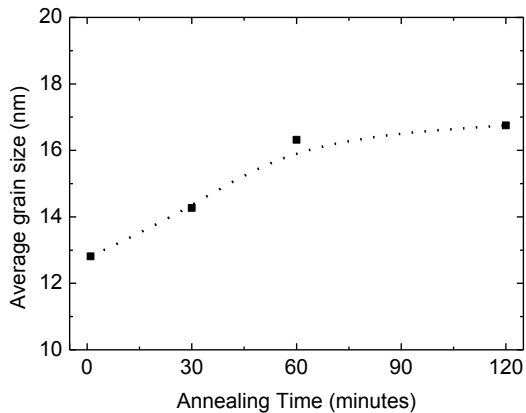
Figure 23 By averaging the grain size obtained through peaks fitting with Scherrer's equation, here a figure of merit of the crystals size of samples annealed for different time are plotted. The dotted line is only to guide in the plot interpretation.

The crystalline domain is notably increasing when the annealing time is taken from 1 to 60 minutes. Eventually the crystal growth stabilises after 2 hours. For all samples the peaks intensity ratio show as previously demonstrated an hyperbranching.
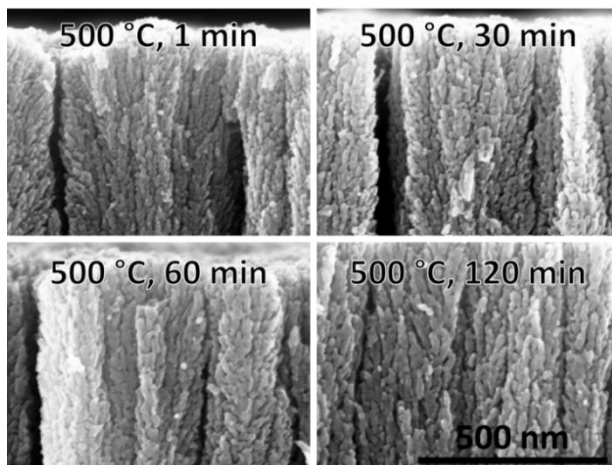
Figure 24 SEM images showing the increasing grains size in samples annealed for an increasing amount of time.

The average domain size is a figure of merit, as the dimensionality of the crystals is not a regular shape and its aspect ratio is changing with time towards crystalline and elongated structures well shown in the TEM images. In the SEM images reported in Figure 24 is however possible to notice an enlarging of the smallest constituents of the hyperbranched nanostructures confirming the calculations performed on the diffraction peaks. This reorganization in larger grains is affecting the volume to surface ratio of the nanoclusters. The roughness factor indeed it is shown to diminish with increasing annealing time. The RF variation reflect the one observed for the grain size as it is more distinct for shorter times while it is almost stabilized above 60 minutes.
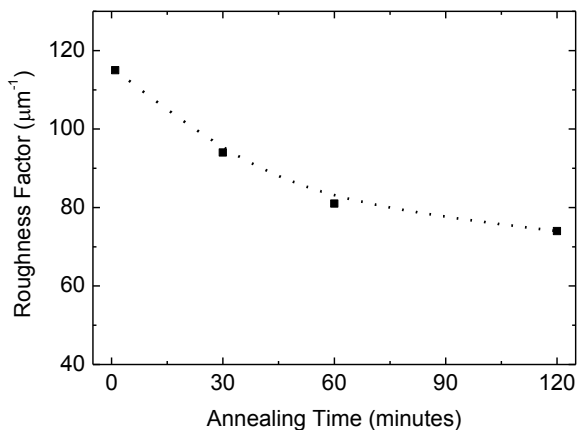
Figure 25 Roughness factor measured through chromatographic photo-spectroscopy of desorbed dye for samples annealed at 500 °C for 1, 30, 60 and 120 minutes

The change in surface to volume ratio it is also confirming the phenomenon observed through BET analysis. Atomic reorganization occurring during crystallization is actually decreasing the surface area onto which the nitrogen used as surface area prober during BET measurements, is supposed to adsorb. Once again the porosity modification is occurring at the nanometre scale. As expected, the phase transition kinetics, is strictly dependent on the temperature. In the case of thermal annealing at 500 °C, both the grain size and the roughness factor variation, are found to be almost stabilized after 2 hours of thermal treatment. In order to investigate the crystallization dynamics a similar experiment is run by changing the annealing temperature while keeping constant treatment time at 120 minutes. A 500 °C range is spanned (300-800 °C) in order to investigate crystallization process across those temperatures known to induce phase transitions. For treatments of 120 minutes, the temperatures at which almost complete phase transitions occur are namely ~350 °C for amorphous-to-anatase transition[19] and around 650 °C.[72] The latter it is not initiated below 650 °C and it is extremely fast above 750 °C. As first analysis Raman spectroscopy is used to assess the allotropic phase of these materials. As expected the samples annealed at 300 °C remains amorphous with a Raman shift spectrum as flat as one of the as

deposited samples. The samples annealed at 400 °C show anatase phase characteristic.
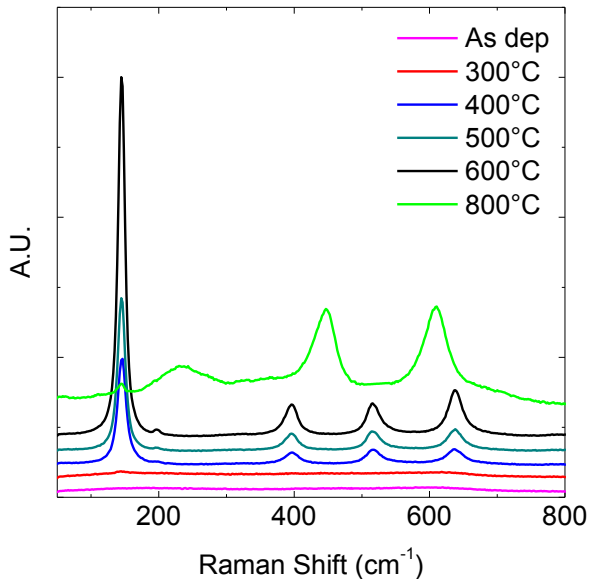
Figure 26 Raman spectra of titanium dioxide samples annealed at different temperatures.

Increasing the temperature leads to an increase in peak intensity and eventually to a full anatase-rutile transition on the sample annealed at 800°C. A partial anatase-rutile transition can be expected even within the 2 hours annealing for temperature between 650 and 800 degrees as described by Czanderna *et al.*[72] In this study however, as the target application requires the anatase phase, the next analysis is limited to this crystalline structures. Similarly to what was done for the samples annealed for different times, XRD analysis is performed on the anatase samples previously presented in Figure 27. Looking at the XRD spectra it is even clearer how the peaks with the lower characteristic intensity are growing and on average all peaks are sharpening. These phenomena are attributed to a better crystallization and the formation of larger grains.
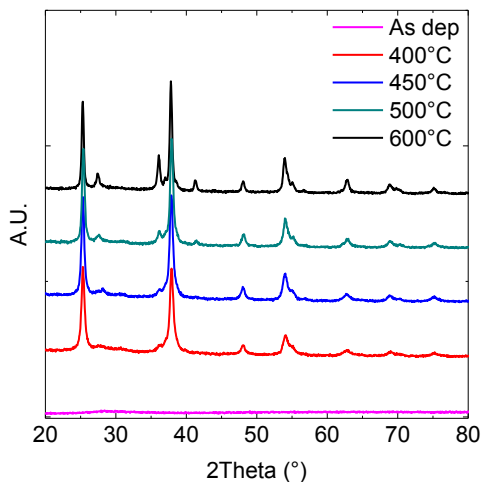
Figure 27 XRD spectra of samples deposited at 7 Pa and thermally annealed for 120 minutes in air at different temperatures.

The full width at half maximum of the XRD spectra was used (see methods) in the Scherrer equation to estimate the crystalline domain size that was found to increase with annealing temperature. This can be seen clearly in the SEM images reported below. The grain volume enlargement is again competitive with the surface area as testified by the roughness factor that is rapidly dropping with increasing temperatures.
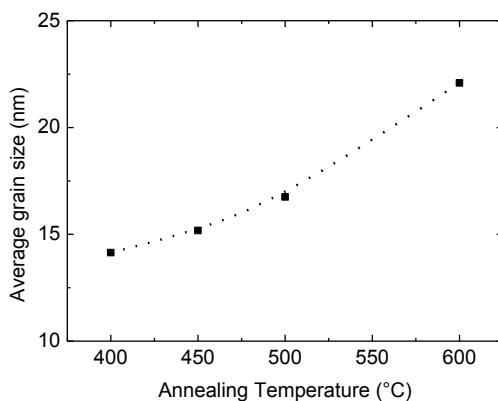
Figure 28 Peak fitting with Scherrer's equation here a figure of merit of the crystals size at different temperature is plotted.
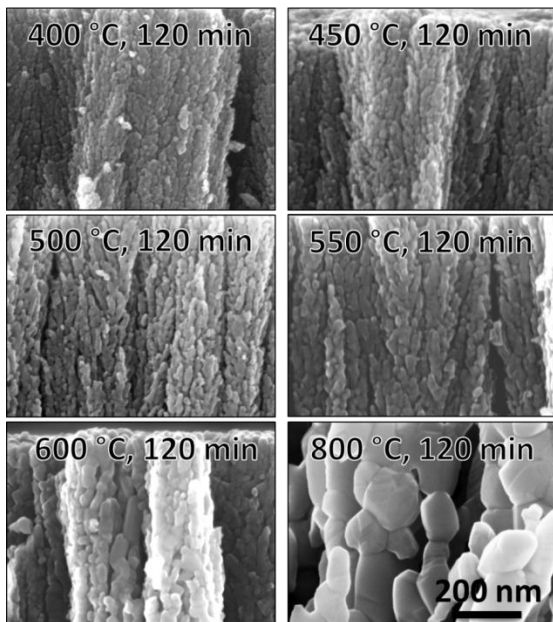
Figure 29 SEM images showing the increasing grains size in samples annealed at different temperatures.
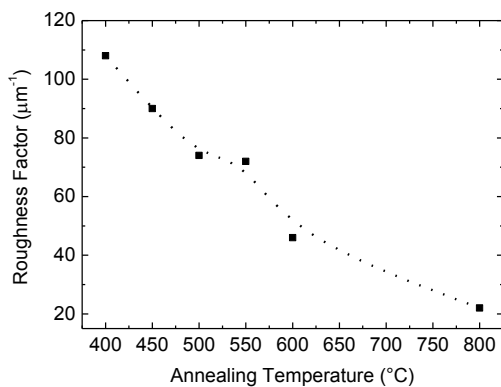
Figure 30 Roughness factor measured through chromatographic photo-spectroscopy of desorbed dye for samples annealed for two hours at different temperature.

Tuning micrometric features

It is plausible to think that as a morphological modification of the nanostructured materials involving nanoclusters packing density occurs, it will also affect their mechanical properties. PLD hierarchical nanostructures possess an inverse conical envelope as it is highlighted in the figure below.
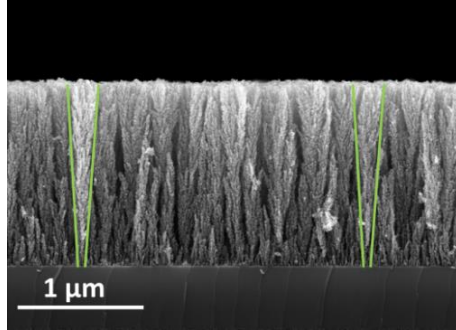
Figure 31 Inverse conical envelope of quasi 1D hierarchical nanostructures deposited by pulsed laser deposition at 20 Pa

As the density decreases the quasi 1D structures lose their stability and stiffness. This phenomenon was already reported in a previous work by Fusi *et al.* (2010). [73]

Their stiffness decrease and so does their stability. The stability induces a collapse of the nanostructures that aggregated in *island.* The island reorganization, which is schematically highlighted in the cross section images of Figure 32, can be induced by two processes (i) either by the capillary forces of a fluid desorbing from the nano-porous structures (*e.g.* in Figure 32 it was induced by soaking the films in ethanol and letting it evaporate) or (ii) by a densification occurring during the crystallization process induced by a thermal annealing. As the film grows thicker this phenomenon becomes more evident. Looking at the surface with an SEM (Passoni *et al.* (2014)[74]), it is possible to see how the dimensions of the cracks that are separating the island are increasing both with background deposition pressure and with thickness as a result of more pronounced collapse. To quantify this characteristic surface feature of PLD deposited nanostructures, a surface ratio (φ) is introduced as

the ratio between the area occupied by the film surface and the area occupied both by area and voids (see Methods).
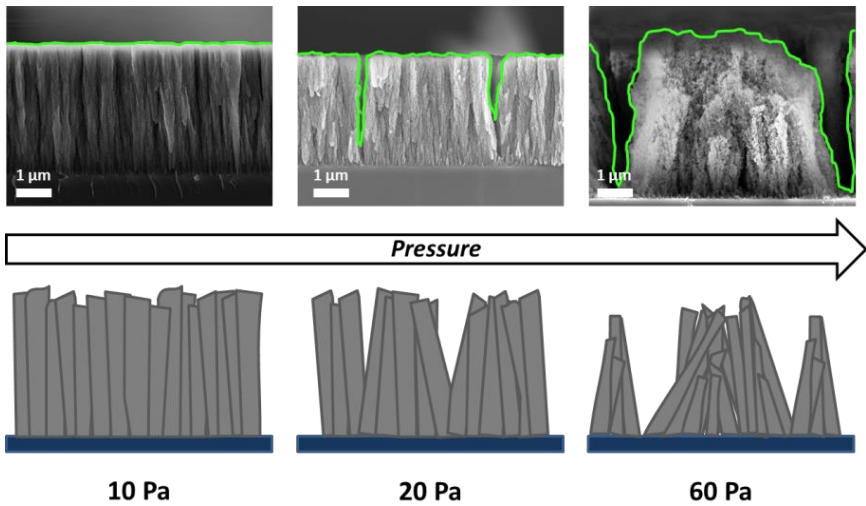
Figure 32 Island formation due to low density packing in quasi 1D nanostructures deposited at high background gas pressure.
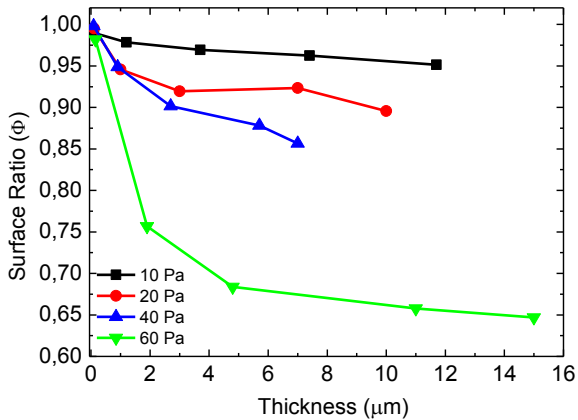
Figure 33 Surface ratios of PLD film surfaces deposited at different pressures with different thicknesses.

In summary by setting different background gas pressure in the deposition process it is possible to control cluster reorganization controlling feature both at the nanoscale (nano-pores and nanocluster size and how they are packed together) and at the microscale by passively inducing features in the micrometers scale length (aggregates of nanostructures). By changing these features is possible to control the density and the specific surface area of the material.
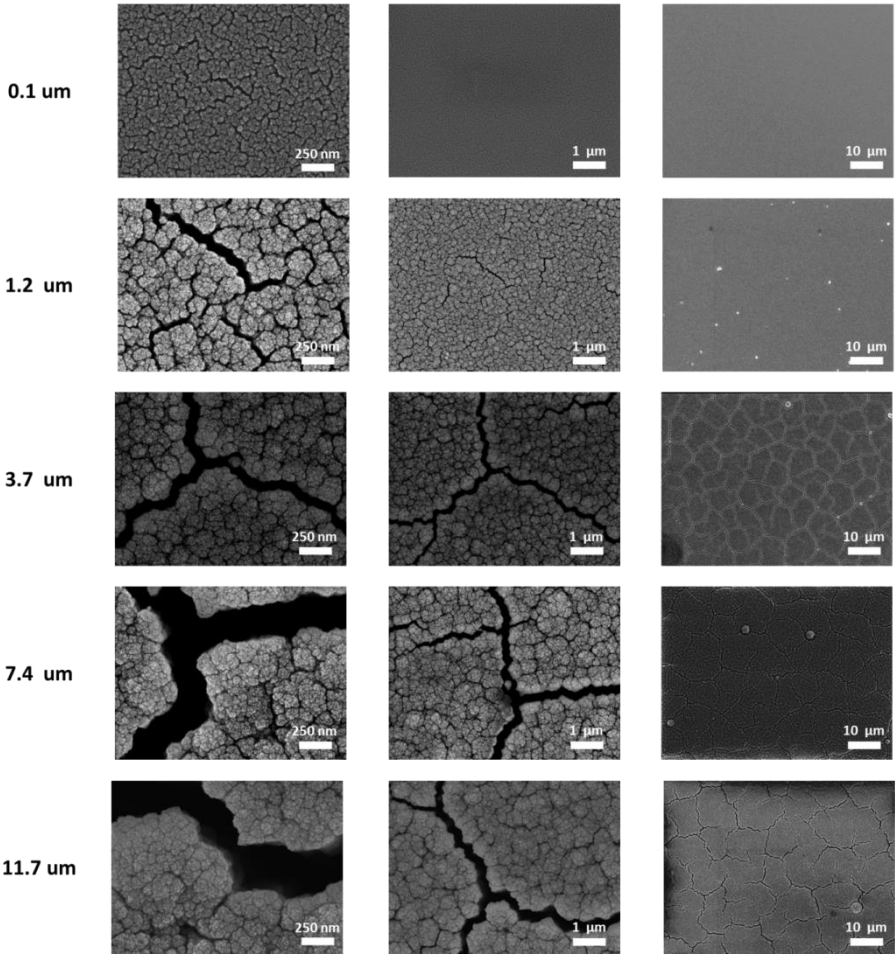
Figure 34 Top view SEM images of samples deposited at 10 Pa different thicknesses with decreasing magnification from left to right.
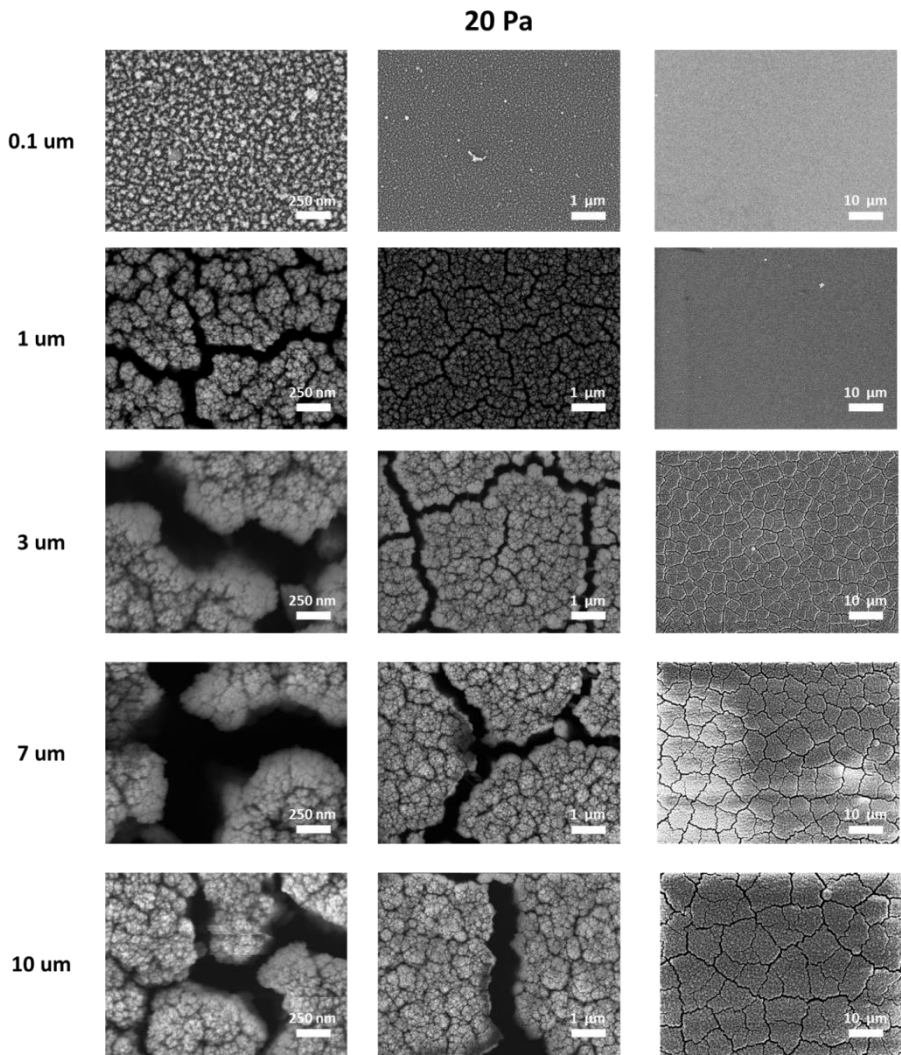
Figure 35 Top view SEM images of samples deposited at 20 Pa different thicknesses with decreasing magnification from left to right.
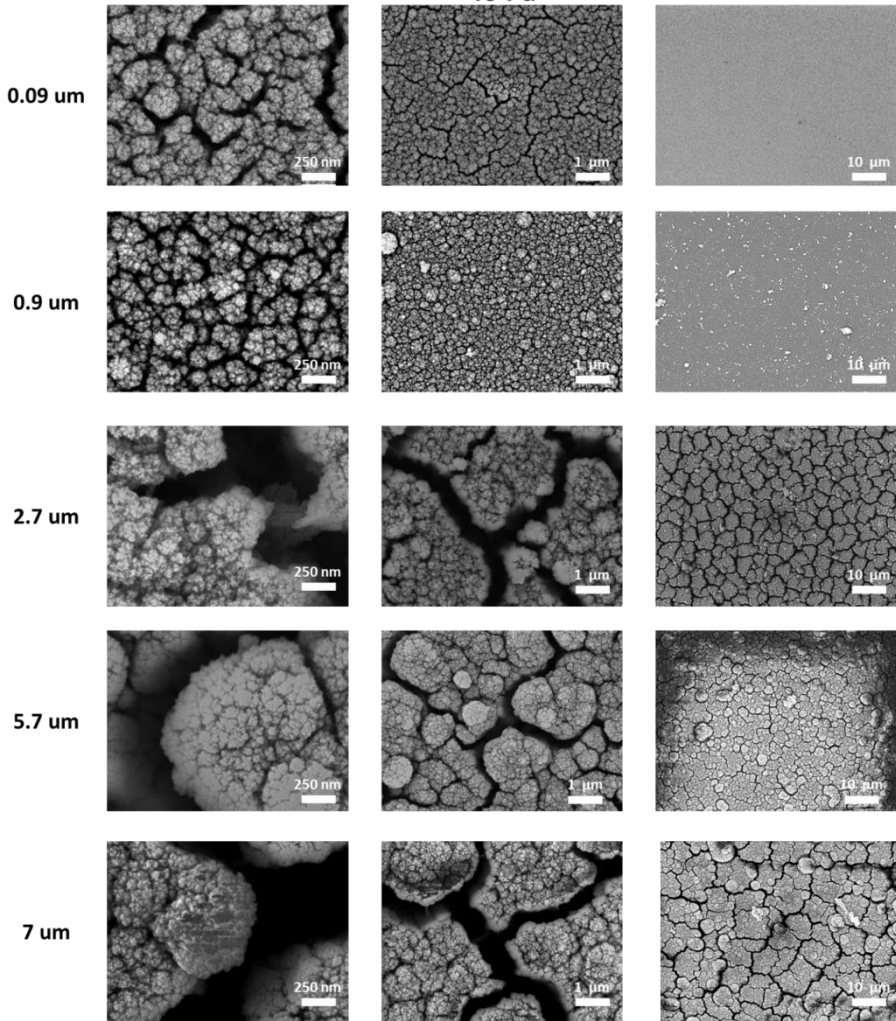
Figure 36 Top view SEM images of samples deposited at 40 Pa different thicknesses with decreasing magnification from left to right.

60 Pa

0.15 um			
1.9 um			
4.8 um			
11 um			
15 um			
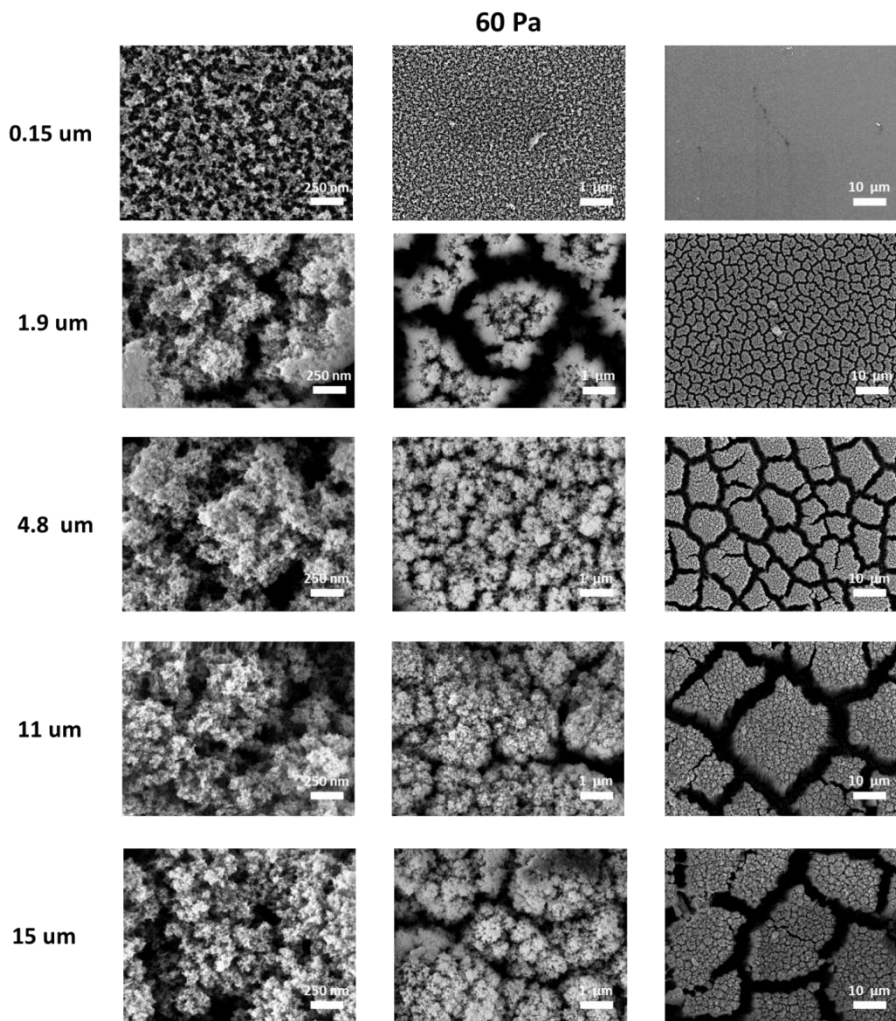
Figure 37 Top view SEM images of samples deposited at 60 Pa different thicknesses with decreasing magnification from left to right.
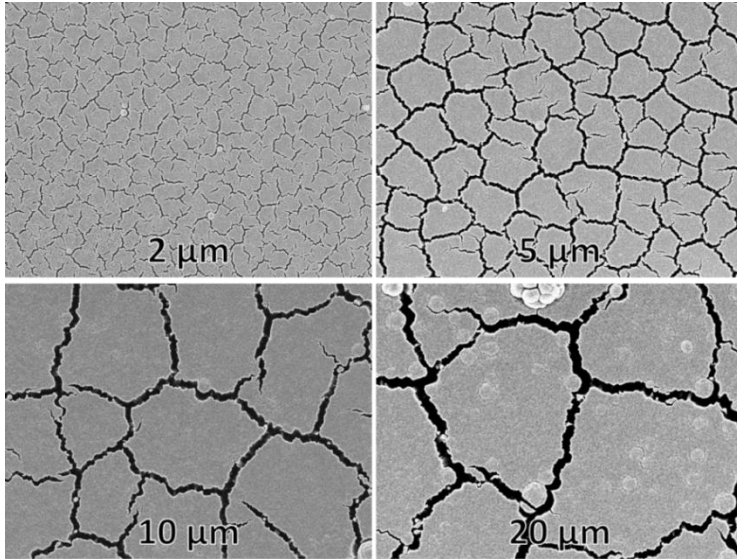
Figure 38 Island reorganization induced by 2 hours thermal treatment for 2 hours on nanostructured films deposited at 7 Pa with different thicknesses

As described by Fusi *et al.*[73], by Passoni *et al.*[74] and as described in this work, the capillary forces acting on the hierarchical nanostructures upon the evaporation of a solvent previously impregnating the film, induce a structural collapse that leads to the formation of microstructures comprising bundles of hierarchical nanostructures. The phenomenon occurs in a similar fashion to the *dry mud effect* for which mud cracks into plates when dries out. This highlights a stiffness failure of the structures that are therefore prone to collapse under certain forces. When thermal treatment is performed on these structures a similar effect is observed. In Figure 38 it is possible to note that the "*islands*" besides resembling the one occurring due to capillary forces, present sizes that are trending with film thickness in a similar manner to the one presented in Figure 34, 35, 36 and 37. In this case however, as there is no liquid evaporation involved, the forces causing the island reorganization are arising from the crystallization process that changes the porosity configuration increasing the grain size. The effect of the collapsing on the

hyperbranched titanium dioxide nanostructures (in this case deposited at 7 Pa of oxygen and annealed for 2 hours at 450 °C) is studied in Figure 39 through analysis of the roughness factor along the thickness of the nanostructures.
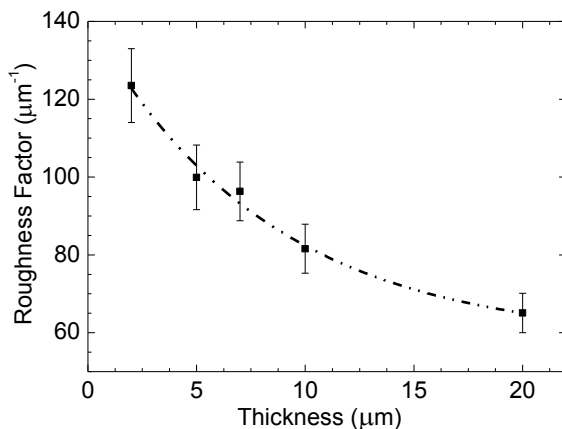
Figure 39 Roughness factor for thin films with different thickness after 2 hours thermal treatment in air at 450°C.

The RF decreases with increasing thickness as a consequence of a densification of the top part of the hyperbranched nanostructures.

In summary the morphology of hierarchical nanostructures was studied and peculiar characteristics were found. The complementary nature of voids and full is such that the hierarchy of the material is caused by and consequence of a hierarchy of the pores. For this reason the pore size distribution is not peaked around a single valued but it is rather broad and range from few to hundreds of nanometers. Similarly the nanostructured fabricated by PLD present a main elongated structures, formed by smaller structures comprising nanometric clusters, stretch out. Elements with different characteristic size react differently to deposition pressure, wetting and dewetting or annealing process. For this reason it is possible to tune the morphology from the atomic (clustering and crystallization) to the micrometric (dewetting and annealing) scale.

Effect of porosity on the refractive index of the material

The complex refractive index components of titanium dioxide are plotted in the graph below (Figure 40). The imaginary part, *i.e.* the absorption, is negligible at wavelengths above 350 nm where titanium dioxide results transparent. The real component of the refractive index is instead above 2 in the whole visible and near-IR spectrum.
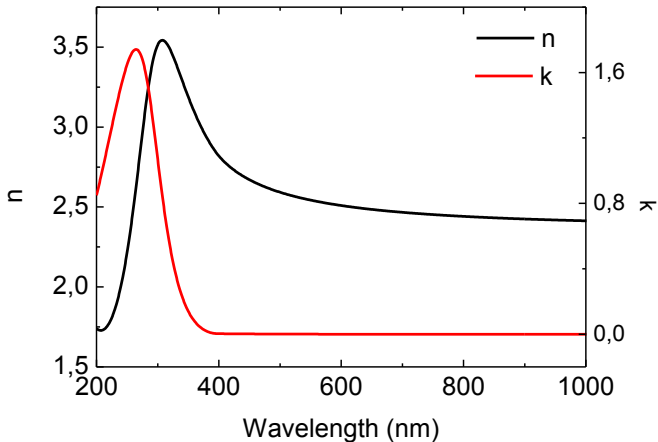
Figure 40 Components of the complex refractive index of titanium dioxide.[75]

In the case of porous materials however the regime is the one of inhomogeneous medium. The refractive index of the film is therefore subject to the effective refractive index approximation. The effective refractive index n_{eff} of the material is:

$$n_{eff} = p \cdot n_{voids} + (1 - p) \cdot n_{TiO2}$$

Where n_{TiO2} and n_{voids} are respectively the refractive index of the titanium dioxide and the refractive index of the medium filling the nanostructures voids and p is the porosity. This means that, as the pressure increases, the void fractions augment lowering the refractive index of the film. By fitting transmittance spectra of titanium dioxide thin films deposited at different pressure with *transfer matrix method,* it was possible to retrieve their effective refractive index.
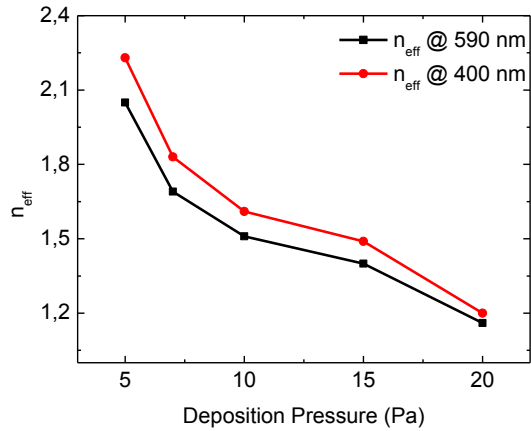
Figure 41 Effective refractive index at two different wavelengths as a function of film porosity calculated through transfer matrix method fitting of transmittance spectra.

Even if the decrease of the effective refractive index with increasing deposition pressure was expected, being able to quantify is magnitude is of paramount importance for several applications as will be shown in the next chapter.

Chapter 3

Applications of nanostructured titanium dioxide
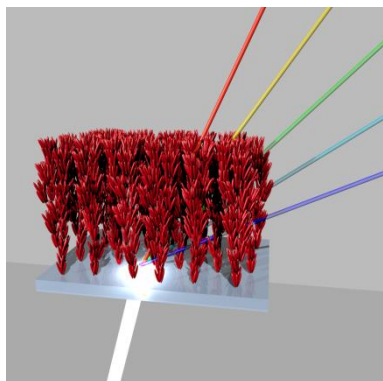
Dye Sensitized solar cells:
Performance enhancement through advanced morphological and optical properties

The world energy demand is increasing; the reasons behind this general trend are complex, diverse, often interconnected and they depend on political, social and geographical regions. Reasons can differ between developing [76] and rich [77] countries and can range from early stage industrial development to consumer electronics diffusion to population growth. This polyhedral scenario raises the attention also on the delocalization of the energy demand, on its disparate usage and on its nexus with economic growth and environmental impact. [78, 79] In fact, independently of where the reasons of the increase in energy request are rooted, it is of primary importance, in the knowledge society,[80] to give the opportunity to plan an energetic strategy that through diversification and globalization will minimize the effect of energy consumption on the environment while promoting welfare. This means going beyond political boarders and to be adaptable to the fast and continuous change in societal layout by wisely using natural resources. A synergetic effort must be put in place by academics and by policy makers to reach a solid and structural result. Fossil energy sources, even leaving aside the most popular argument of pollution[81] and the debate on their depletion, cannot single-handedly cope with the issues briefly introduced above. While, for different reason, singularly taken, nuclear, tidal, wind, solar energies are neither effective option, a viable route to achieve an appropriate energy production arrangement could be a synergetic action of all these sources. Surely mankind cannot disregard and must push towards the exploration and development of any scientific and technological asset that could serve this scope. In other word, no energy source should be regarded as alternative to another but rather as a complementary piece of a complex puzzle. Similarly this concept applies within each energy source; research cannot be exempt from investigating different technologies to make the best use of a resource. Solar energy is a remarkable example as it is

Figure 42 NREL efficiency chart.

converted in electricity either indirectly through thermal energy or directly by the photovoltaic effect. Within this major distinction also photovoltaics comprises a number of different technologies that allows the use of solar energy in diverse applications. For decades the scientific community has worked to find and improve new ways of converting solar energy into electrical energy. In Figure 42, the chart edited yearly by the National Renewable Energy Laboratory (NREL), shows the historical evolution of 24 subcategories of photovoltaics technologies. As the power conversion efficiencies compared on the NREL chart, there are several other parameters (cost, weight, durability, disposability, aesthetics *etc*.) that make each of these categories worth to be studied. Despite the often high investment cost and the isochronous power generation, still photovoltaics operate, like other renewable energy technologies, without emitting greenhouse gasses. It plays an important role in the reduction of pollution.

The advent of novel scientific discovery and technological advances has not only been beneficial for the existing photovoltaic technologies but was also responsible for the emergence of new and fascinating concept. This is the case of nanotechnology. The ability to study the dynamics occurring in nanoscale systems is today reinforced by the one to control the matter composition and structure at the atomic level. Thanks to nanotechnology it is possible to study and exploit effects that are not occurring in bulk materials. Among the photovoltaic technologies born and developed on the shoulders of nanotechnology, dye sensitized solar cells (DSSCs) are a particularly interesting example that, despite their discovery date back only 25 years, are already seeking their place in the market of the renewable energy generation systems. Since their invention in 1991 by professor M. Grätzel,[82] dye-sensitized solar cells have achieved a maximum power conversion efficiency of 13 % [83] at laboratory scale while module have shown a nominal efficiency of 5%[84] and products are already sold on the market. [85] Compared to other technologies they do not soar with high efficiencies but they do possess several advantages such as low fabrication cost, lightweight (they can be fabricated on flexible plastic material) and semi-transparent colourful design that can easily be integrated in building facades or in several devices.
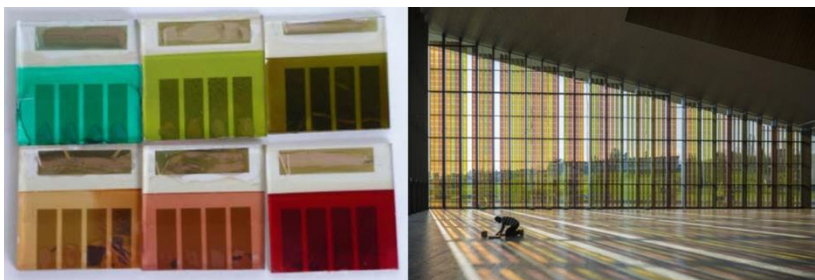
Figure 43 Left) Example of colour variation laboratory scale dye sensitized solar cells and Right) the application of dye sensitized solar cells in the façade of the conference palace at the EPFL in Switzerland.

Working principles

As dye sensitized solar cells are photovoltaic devices, they operates thanks to their ability of converting photons into electrons that are then made available for an external circuit which drives a load.
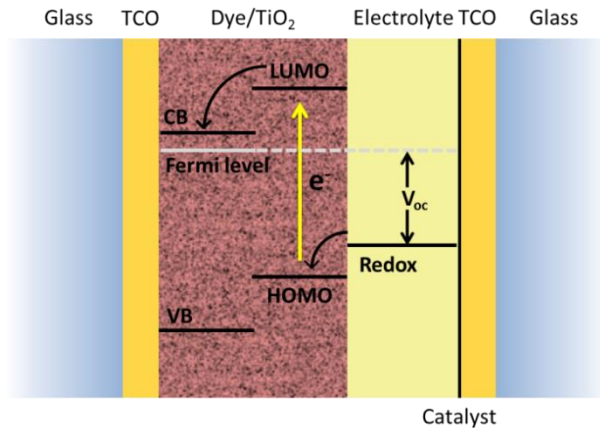
Figure 44 A DSSC standard architecture and the schematic of the ideal working principle of the device [86]

The architecture of these devices is shown in Figure 44. A large bandgap porous semiconductor, such as titanium dioxide, is covered by a chemisorbed monolayer of dye molecules (reddish mesoporous layer) and is filled infiltrating a hole conductor (yellowish in Figure 44). This structure is supported by a transparent conductive oxide (TCO) coated glass and sandwiched with a similar glass as counter electrode.

Thanks to its design the dye molecule, when it is shined by the light, undergoes transition from its ground state (*i.e. highest occupied molecular orbital* or *HOMO*) to an excited state (*lower unoccupied molecular orbital* or *LUMO*). In this HOMO-LUMO transition the electron orbitals of the dye molecule are delocalized closer to the dye anchoring group (typically a carboxylic group) where they are more luckily to be injected in the conduction band (CB) of the metal-oxide. An example of the electron

delocalization is shown in Figure 45 in a schematic taken from the Time-dependent density functional calculations in reference [87].
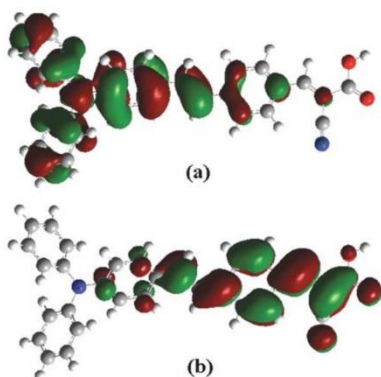
Figure 45 Time domain-density functional theory calculation of a dye molecule showing the (a) HOMO and (b) LUMO electron distribution. The red atoms on the right-hand side of the top figure are the carbon of the carboxylic anchoring group. A the light shine, the electron cloud moves towards the anchoring group (see b) favouring electron transfer into the titanium dioxide. Figure from reference [87]

In the LUMO state an unbalance in the charge distribution leads to the formation of a so-called exciton,[88] an electron-hole pair in a bound state. The exciton splitting into free charges, *i.e.* the overcoming of Coulombic attraction between electrons (close to the anchoring group) and electron-holes (left on the "other side of the molecule"), also called Exciton Binding Energy (EBE)[89], is thought to be driven by the potential difference between the CB of the metal oxide (or more precisely its quasi-fermi level) and the LUMO level of the dye. The electron injected in the TiO_2 is transported through the semiconductor[90, 91] towards the anode. This process leaves an electron vacancy in the dye which is *regenerated* by the hole conductor (or electrolyte) which turns into an oxidized state. Eventually the electron is taken from the anode to the cathode by an external load circuit and regenerates the electrolyte left oxidised by the dye. While the photogenerated current is thus determined by the capability of the system to generate and circulate the electrons, the maximum voltage of the device (also called open-circuit voltage or V_{oc}) is determined, in the ideal case, by the potential difference between the quasi-

Fermi level of the semiconductor (that can be approximated with the CB in the case of n-type semiconductor and in particular when electrons are injected) and the redox potential of the electrolyte. The interface between TiO_2 and electrolyte can be seen as semiconductor-semiconductor interface which leads to a current-voltage curve characteristic of a diode where for zero applied reverse voltage and under illumination condition the device will display short circuit current (I_{sc}) while for applied bias voltages opposite to the V_{oc}, electron circulation is impeded and the current is zero.

The deviation of this curve from the ideal rectangular diode curve is described by the fill factor (FF) which is defined by the ratio between the area of the rectangle defined by the voltage and the current density value at the maximum power output and the area of the rectangle having J_{sc} as height and V_{oc} as base (see Figure 46).
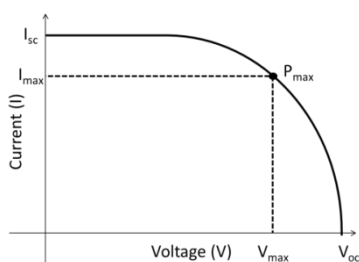
Figure 46 Current-Voltage curve of a photovoltaic device.

In each step of the energy conversion process competitive and detrimental processes can occur, leading to a less efficient energy conversion. These processes are mainly recombination process that leads to the loss of charge hampering the overall device performance[92, 93]. The photogenerated charges might indeed undergo the following process:

1. Electrons in the dye LUMO recombination with the electrolyte
2. Electrons in the dye excited state recombine with the vacancy left in the dye itself
3. Electrons from the CB of the semiconductor recombine back with the ground state of the dye or to the electrolyte

The ultrafast charge separation (few tens of femtoseconds) makes the above events, which are order of magnitude slower, less luckily to happen. For a good understanding of the timescale of each event described above and depicted in Figure 47 [94], the reader could refer to the review in reference[95].

1. Photon adsorption by the photoactive medium (dye);
2. Exciton formation and charge separation;
3. Charge injection from the dye to the metal-oxide;
4. Charge transport through the metal-oxide to the electron;
5. Dye regeneration by the electrolyte;
6. Electrolyte regeneration by the electrons
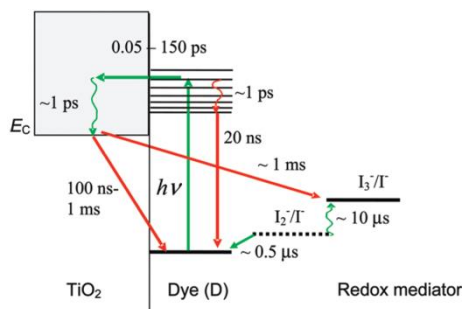
Figure 47 Timescale of the main photogeneration and recombination processes in DSSC. From reference [94].

Given the main events (summarized above) and their possible failure due to the recombination processes it is important to define quantities that help in determining the overall efficiency of the power conversion from sun power to electrical power. Indeed the power conversion efficiency (hereafter PCE) will be the ratio between power output and power input (namely incident light power). In turn the power output will be influenced by the power input adjusted for the light absorbance (η_{abs}, being the number of photons absorbed over the incident photons), the Internal Quantum Efficiency (IQE, being the number of photogenerated charges over the number of *absorbed* photons) and injection and collection efficiency (respectively η_{inj} being the efficiency of electron injection from the dye into the semiconductor and η_{col} being the efficiency of those electron to be collected by the anode electrode).

All these parameter will therefore include the effect of recombination and not efficient charge transport.

$$PCE = \frac{P_{out}}{P_{in}} = \frac{P_{in} \cdot IQE \cdot \eta_{abs} \cdot \eta_{inj} \cdot \eta_{col}}{P_{in}} = IQE \cdot \eta_{abs} \cdot \eta_{inj} \cdot \eta_{col}$$

Improving these efficiencies is the main task of researchers that design each component of the cell to work in synergy and optimize free charge photogeneration and transport. Key components that must be optimized are therefore: the dye to favour light absorption and electron generation, the metal-oxide (*e.g.* titanium dioxide) to reach a nearly 100 % efficient electron transport, the electrolyte to have a fast regeneration of the photoactive dye and last but not least the three above mentioned components interaction must be considered. The latter requirements involve mainly a proper energy bands alignment between dye and semiconductor to permit charge injection and prompt dye regeneration by the electrolyte so to make dye molecules always active for photogeneration, compatibility between the dye and the redox couple and stability of the system to thermal and photochemical stresses.

Sandwich-like dye sensitized solar cells
As already mentioned, dye sensitized solar cells are photo-electrochemical cells comprising two electrodes enclosing an active layer that has the function of generating free electric charges. This device architecture is often referred to as *sandwich-like* structure. Despite their scope does not change, the four major components of a dye sensitized solar cell (*i.e.* working and counter electrode, holes transporter and photoactive layer) can differ depending on the system. Two main configurations, essentially differing in the hole transporter phase, can be found: (i) liquid state dye sensitized solar cell and (ii) solid state dye sensitized solar cells. In the former case the hole transported is a liquid redox couple that is physically contained in the reservoir formed by the two electrodes spaced by a polymeric sealant. In the latter the hole transporting material is a polymer that is infiltrated into the mesoporous active layer and onto which the counter electrode is deposited directly. In the next paragraphs these two main categories will be explained in more details.

Liquid state dye sensitized solar cells[96]

Liquid redox electrolyte is the most widely used mean for the regeneration of the oxidized dye and DSSC based on this hole transporters are still the most efficient. The photoactive layer comprising dyed titanium dioxide is deposited on a transparent conductive oxide coated glass. A platinized counter electrode, matched on the opposite side of the active layer, is attached with a thermoplastic sealant that creates a reservoir that is eventually filled with the liquid electrolyte (see Figure 48). The liquid electrolyte in this case is filled through a hole previously drilled into the counter electrode and finally sealed back to avoid electrolyte evaporation or leakage. Typical power conversion efficiencies of this device architecture are set above 10 % with a record of 13 %. [83] Despite their leading position in terms of performances, DSSCs using this kind of mediator present however several drawbacks related to the liquid nature of the electrolyte. Indeed, corrosion, leakage and degradation are still today major issues related to this type of cells.[97]
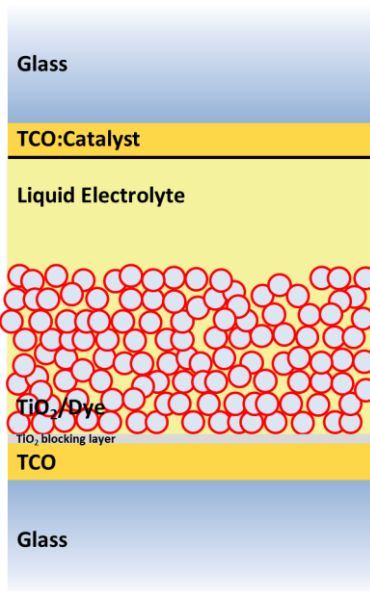
Figure 48 Schematic of liquid DSSC configuration

Liquid state DSC: Hyperbranched Photoanodes [96]

Five micrometers thick hyperbranched photoanode TiO$_2$ scaffold (h-PA in this paragraph) was sensitized using C106 dye and filled with an iodide/triiodide redox electrolyte. To study whether an optimal crystalline domain size and roughness factor could be found, a 200 °C temperature range was scanned in the thermal treatment of the titanium dioxide photoanode. An optimum was found at 450 °C. As shown in Table 1, the overall power conversion efficiency is decreased by the predominant effect of the photocurrent density (J) which decreases from 15.7 (annealing at 450 °C) to 14.0 mA/cm^2 (annealing at 600 °C). The sample comprising a photoanode thermally treated at 400° C show lower Jsc compared to the samples annealed at 450 °C in contrast to the trend found over the other annealing temperatures. This is attributed to poor photoanode crystallization.

Table 1 Photovoltaic performance of DSC based on h-PA annealed at different temperatuers

Samples	Voc (V)	Jsc (mA/cm^2)	FF	PCE (%)
h-PA 400°C	0.712	14.56	0.72	7.6
h-PA 450°C	0.737	15.7	0.75	8.7
h-PA 500°C	0.746	14.9	0.74	8.3
h-PA 550°C	0.749	15.0	0.73	8.3
h-PA 600°C	0.763	14.0	0.74	7.9
PA	0.724	12.5	0.72	6.7

The open circuit voltage (Voc) follows an opposite trend. The Voc of the samples annealed at 400° C is approximately 50 mV higher compared to those annealed at 600° C. The different surface areas available may also contribute to the Voc trend because the different amount of dye molecules adsorbed on the surface. It is worth noticing that all devices based on hyperbranched nanostructures (red lines) improves photovoltaic performances of reference

devices (black line) comprising mesoporous layer in the same dye/electrolyte environment.
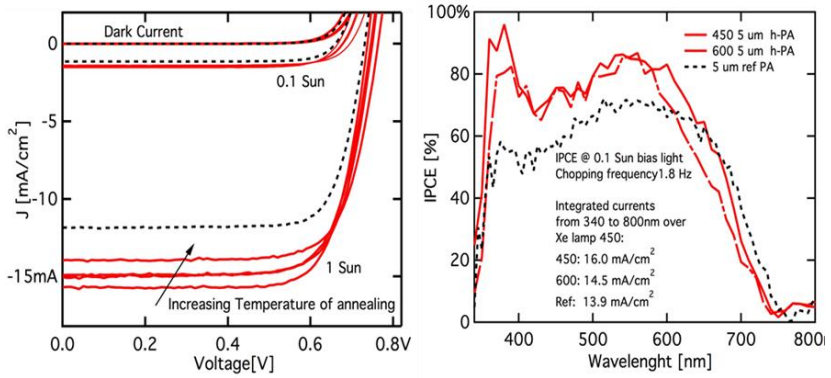
Figure 49 Performances of DSCs fabricated with photoanodes that underwent thermal treatments at different temperatures. (left) JV curves and (right) EQE.

The reason behind the performance improvement shown by devices based on hyperbranched photoanode (h-PA) is two-fold.
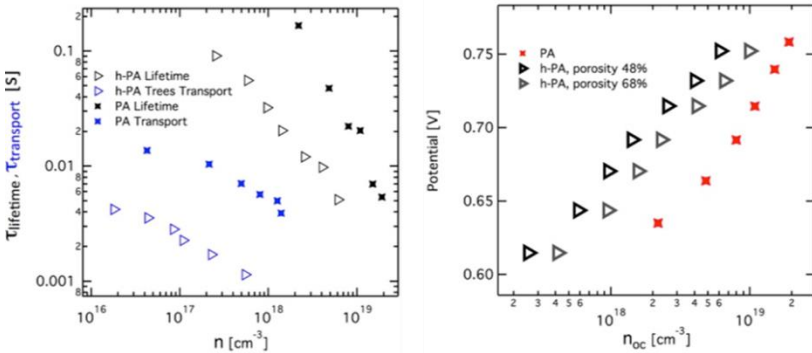
Figure 50 (left) Transient and (right) charge extraction measurements performed on standard mesoporous photoanodes and on h-PA based DSC.

Optimized hyperbranced nanostructures, as reported in Figure 50 show faster charge transport in comparison to standard mesoporous photoanode (PA) and they also possess peculiar optical scattering properties described in the optical analysis of the materials in the previous chapter. The higher incident photon to current efficiency (IPCE) reflects the increase in Jsc. In the spectral region where the dye extinction coefficient is lower, the quantity of up-taken dye on the photoanode determines IPCE broadness.

Table 2 Photovoltaic performances of h-PA annealed at 450 °C, 5, 10 and 15 micrometers thick.

h-PA Thickness (µm)	Voc (V)	Jsc (mA/cm^2)	FF	PCE (%)
5	0.724	14.6	0.76	8.1
10	0.712	16.4	0.74	8.8
15	0.692	16.6	0.72	8.4

To verify whether thickness increase could lead to higher power conversion efficiency, h-PAs as thick as 5, 10 and 15 µm were tested. JV curves and respective IPCE spectra are reported in Figure 51.
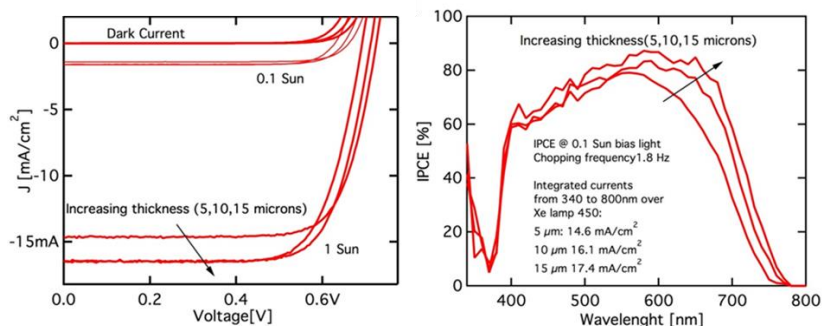
Figure 51 Photovoltaic performances of h-PA annealed at 450 °C, 5, 10 and 15 micrometers thick (left) JV curves and (right) EQE spectra.

A broadening of less than 50 nm in the near-IR region is observed in the IPCE spectra. The short circuit current density, measured with sun simulator, is calculated by multiplying the integral of the IPCE spectrum with the electron charge times the solar simulator lamp spectrum over the whole visible range (340-800 nm). The calculated current densities are 14.6, 16.1, 17.4 mA/cm^2, respectively for the 5, 10 and 15 μm thick h-PA. The current densities measured under solar simulator at 0.1 sun condition are 1.52, 1.68 and 1.72 mA/cm^2 while at full sun (98.8% of AM1.5) are 14.6, 16.4 and 16.6 mA/cm^2. The relative increment in the current density between the 5 μm and 10 μm thick h-PA is in good agreement for all the three measurements (respectively 10%, 10% and 12% for IPCE calculation and the 0.1 sun and 1 sun measurements). When passing from 10 μm to 15 μm thick photoanodes the relative increase of the photocurrent is lower. For the full sun measurement it is 1.2 % of relative increment is measured in contrast to the 2.4 % of 0.1 sun and the 8% of the IPCE measurement. There thus a saturation of photovoltaic performance of the device with h-PA 15 μm thick. This is attributed to the morphological modification occurring at the top part of hyperbranched nanostructures above a certain thickness and described in the last previous chapter and shown in Figure 38. As the film grows thicker, the previously described densification phenomenon occurs on the top part of the film of the hyperbranched nanostructures.
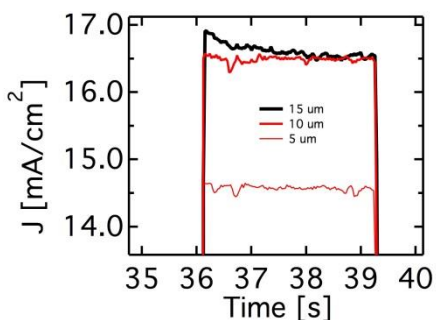
Figure 52 Current dynamics of samples comprising h-PA with different thicknesses.

As shown by roughness factor measurement, the porosity and so the equivalent surface area is not increasing linearly with film thickness and this might lead to saturation in current generation and to diffusion issue. In Figure 52 the current dynamic is reported for the three h-PA measured in Figure 51. Further process optimization is required in order to improve the control on film morphology along its thickness to avoid the densification occurring on thicker h-PA. A viable solution, yet to be explored in a complete device, could be to superimpose 5 micrometre thick film on a multi-stack to form a thicker film. Before depositing the next layer, a thermal annealing should be done on the previous layer inducing the densification on the 5 micron thick previous layer. This way the island reorganization could be frozen to the one characteristic of the 5 micrometre thick film while the thickness could be increased (see SEM image below).
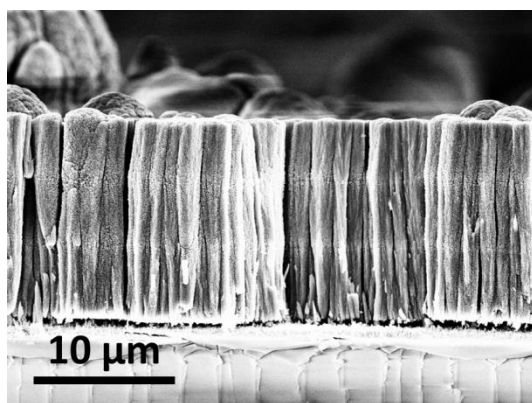
Figure 53 Three 5 μm are superimposed into a 15 μm thick film. a thermal annealing is performed before each layer deposition to freeze the island reorganization to the one characteristic of 5 micrometers thick layers

In a parallel experiment, a 17 μm thick h-PA device with a 17 μm standard device with scattering layer (12 μm mesoporous layer + 5 μm of scattering overlayer) were compared obtaining similar power conversion efficiencies (9.23 % vs. 9.21 % respectively). h-PA were successfully tested also with a cobalt electrolyte in a similar configuration as in reference [98] obtaining an overall efficiency of about 10 % at 1 sun illumination.

Solid state dye sensitized solar cells

To overcome the problems related to the use of liquid electrolytes, a so called solid-state DSSC type was engineered where the liquid electrolyte was replaced by a polymer working as hole transporting material (HTM). Besides an obvious excellent hole mobility a good hole transporting material, such as the most used _spiro-OMeTAD_, has to be able to fulfil other requirements. Indeed the intrinsic difficulty of the hole transporting material to percolate to the bottom of the photoanode creating a uniform interface with the porous semiconductor is the constrain that limits the development of thicker devices and preventing a further increase in light absorption. In 2004 _W. Feng et al._[99] reported an improvement in ss-DSSCs performances upon the increase in interface between the HTM polymer and the titanium dioxide. An optimum pore filling factor was found by _I-K Ding et al._ (2009)[100] upon spin coating rotational speed and spiro concentration. The influence on dye-sensitized solar cells performance of the polymer filling factor was extensively studied and an empiric law to determine ex ante the pore filling factor was studied.[100, 101] Attention must be paid on the difference between wettability of pores and pore-filling. If the pores are wetted by the HTM forming a monolayer, the charges will move towards the counter electrode following a tortuous path along the mesoporous layer. If the HTM is forming a thicker layer around the titanium dioxide/dye structure the charges could follow a straight path reducing the issues related to higher charge mobility.[102] Several methods to measure the quantity of HTM present in the device and therefore the level of pore-filling has been developed. However just at the beginning of 2013 _Docampo et al_.[103] developed a not destructive method to measure accurately the pore-filling by optical analysis. Spiro-OMeTAD has a refractive index of 1.92 and the optical response of the photoanode (having a refractive index around 1.5) is dependent on the quantity of HTM present inside the pores. Therefore through refrectometry they were able to precisely estimate the degree of pore-filling and thus optimize it. Considering the necessity of percolation channels for interface formation between HTM and TiO_2 and the limited thickness, Quasi-1D hierarchical nanostructure are currently widely investigated as possible solution for their elongated percolation paths and for their advance light management capability. Nowadays Solid-state dye sensitized solar cells have reached a power conversion efficiency over 10%.[104]
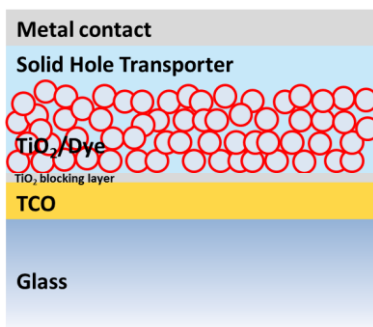
Solid state DSC: Hyperbranched Photoanodes [70]

In solid state dye sensitized solar cells (thereafter ss-DSC) a solid hole transporting material (HTM) is used in place of the standard liquid electrolyte.[105-107] Their usage solid structure is source of great versatility; however, despite their undisputed potential, their industrialization is still hampered by their low power conversion efficiency, resulting from photocurrent generation much lower than in the liquid DSC. As ss-DSC have photoanode whose thickness is limited below 2 μm to allow good HTM percolation and fast hole transport, their optical density is too low, resulting in poor current photogeneration. Several studies have been trying to enhance the power conversion efficiency of ss-DSC by addressing the attention to different physical phenomena and technical features. In particular novel semiconductor architectures to improve electron transport have been studied. [108, 109] To enhance light absorption, great effort was put in place to increase the optical path of the light within the photoactive layer beyond its physical thickness. Advanced light scattering and light trapping architecture were employed specially in liquid DSC and great variety of methods, reviewed in the literature,[69, 110] were adopted. The most common and employed strategy consists in using a scattering overlayer made of large size nanoparticles (from 200 to 400 nm).[111] Other materials with different shapes but with similar functionality were attempted (*e.g.* quartz fibers[112] and nanotubes,[113, 114]). One of the major issues associated to this solution is the parasitic light absorbance associated to the photoanode scattering overlayer not actually contributing to the charges photogeneration. To reach a compromise between light scattering and dye absorption large size and porous materials, such as hollow embossed-nanosphere with high surface

area[115] or particles having different size,[18] have been engineered. In a publication [116] a blend of few nanometers large particles, increasing the surface area, and large particles, enhancing light scattering is studied showing 28% of increased performance. One dimensional nanostructures (*e.g.* nanotubes[35, 64] and nanofibers[117, 118]) were studied to improve electron transport (thanks to electron channelled conduction) and to favor the HTM infiltration. Despite the fact that pore filling fraction is not a limiting factor in highly optimized photoanodes,[103] still novel architectures less with open and directional porosity could be beneficial for the development of high efficiency DSC. In this section ss-DSC with improved optical density are shown to increase power conversion efficiency were fabricated using a photoanode architecture comprising an array of hyperbranched nanostructures. The "*nanoforest*" is the one presented in the previous chapter and also used in the previous paragraph for liquid state DSC. The increased density of each single hyperbranched nanostructure increases their effective refractive index enhancing their scattering properties. As a result, nanotrees act as integrated broad band scattering elements having length scales as large as the visible light wavelength. The overall photoanode benefits from this with an improved optical absorption that in turn yields to higher short circuit current and higher power conversion efficiency with respect to the reference mesoporous photoanode.

The optical characteristics of the photoanodes after thermal treatment are evaluated with a UV/vis spectrophotometer on bare titanium dioxide deposited at different pressures to quantify their light scattering properties. A standard thickness of 1.7 μm typical of ss-DSC was chosen.

Diffuse transmittance of all devices fabricated with PLD at different pressures and with standard nanoparticle paste can be found in Figure 54a. After N719 dye sensitization the photon-dye molecule interaction and is increased leading to higher absorptance shown in Figure 54b[119] (37.5% higher than the one of nanoparticles reference). Being the roughness factor generally lower than the reference, (the 7Pa film has RF 8% lower than the one of nanoparticles reference), the enhancement in optical density was attributed to the peculiar light scattering of the hyperbranched nanostructured photoanode. The absorptance of the whole dyed photoanode subtracted by the one of glass, FTO, compact layer and bare TiO_2 is named hereafter light

harvesting efficiency (LHE, which is connected to charge photogeneration). The LHE (Figure 54b) was integrated across the visible range (350-750) and multiplied by the solar photon flux AM 1.5. Assuming an Internal Quantum Efficiency (IQE) (*i.e.* each absorbed photon is converted into charge carrier transported to the electrode) of 100%, the maximum expected photogenerated current density for can be estimated. From this calculation the hyperbranched and nanoparticles photoanodes could respectively generate 6 and 4.6 mA/cm^2 (+30% increase for hyperbranched photoanode).
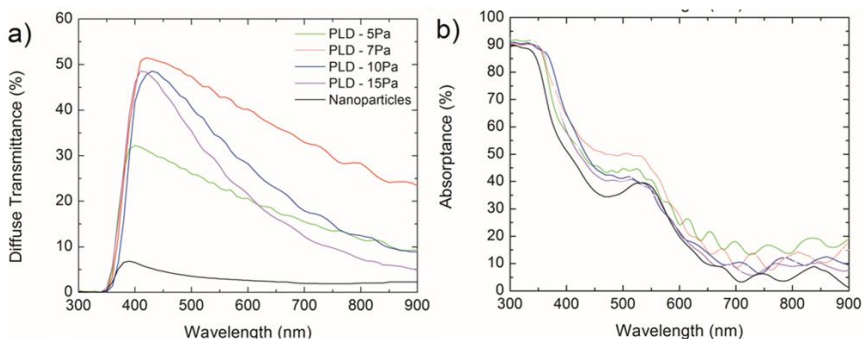
Figure 54 Optical analysis of devices fabricated at different pressures by Pulsed Laser Deposition is compared with standard nanoparticles mesoporous layer. (a) Diffuse transmittance and (b) absorptance.

In a preliminary experiment on hierarchical photoanodes comprising film deposited by PLD at different pressures (namely 5, 7, 10, 15 and 20 Pa) those samples with hyperbranched photoanodes (fabricated at 7 Pa) emerged as the optimum, coherently with the results of the optical characterization and with those of RF measurements. Table 3 shows the photovoltaic performance for the PLD optimized photoanode comprising hyperbranched nanostructures. In Figure 56b the champion device performance is presented. Due to a delicate fabrication process, that at lab scale is still left to an handcraft-level, ss-DSC present an high intrinsic variability in photovoltaic performance. For this reason the full statistic regarding photovoltaic performance of several samples is presented in Figure 55.
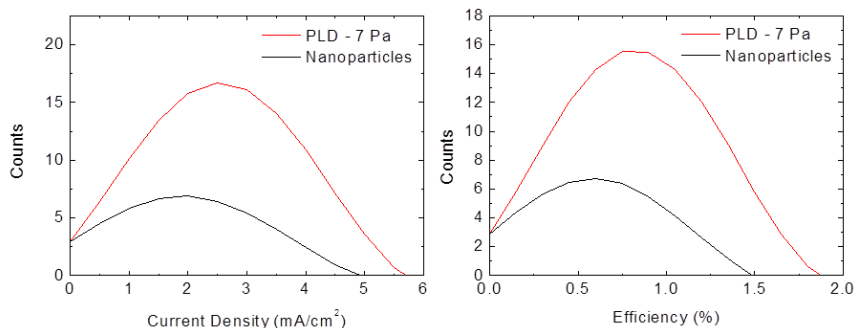
Figure 55 Current density and power conversion efficiency distribution across the fabricated set of samples (7Pa *vs*. Nanoparticles reference).

The EQE spectra of average performing devices were divided by the LHE spectra to derive the internal quantum efficiency of both the device types (Figure 56) with hyperbranched and with standard nanoparticles thin films.

Table 3 Best and average photovoltaic performance of the PLD-based devices sensitized with N719 dye and fabricated with the optically optimized photoanode anode, and of the nanoparticles standard device.

N719	Voc **(V)**	Jsc **(mA/cm²)**	FF **(%)**	η **(%)**
Nanotrees (7 Pa) **Best**	0.67	5.92	41.14	1.77
Nanoparticles Best	0.72	4.88	41.90	1.56
Increment (%)	-6.94	+21.31	+1.81	+13.46
Nanotrees (7 Pa) Average	0.70	2.70	45.55	0.86
Nanoparticles Average	0.72	2.00	44.38	0.64
Increment (%)	-2.72	+35.06	+2.65	+34.37
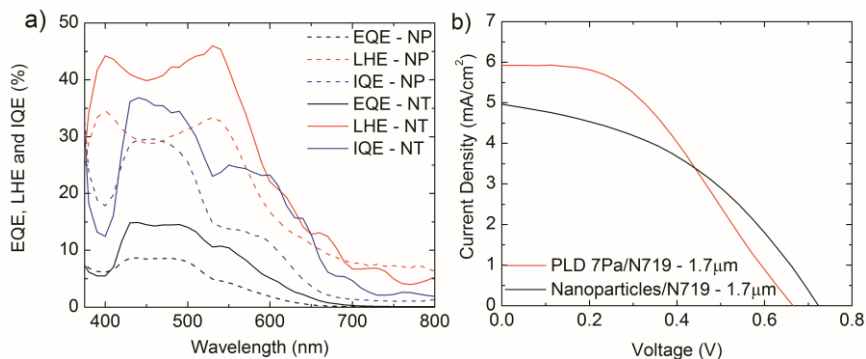
Figure 56 Light Harvesting Efficiency (red), EQE (black) and IQE (blue) spectra for nanotrees fabricated by PLD at 7 Pa (solid line) and for standard nanoparticles paste (dotted line). b) Champions devices J-V curves for device optically optimized nanotrees (red)

The higher IQE of the photoanodes comprising hyperbranched PLD film was a result of the peculiar elongated structure of the nanostructured material which is creating a preferential pathway for electron collection. To retrieve a mean IQE value the measured current density at short circuit was divided by the one calculated by the LHE spectra integration (*i.e.* assuming IQE equal to 100 %).
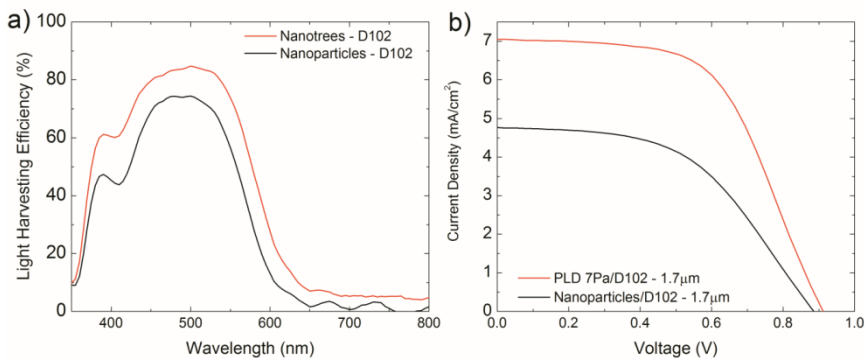
Figure 57 Light Harvesting Efficiency (LHE) (a) and JV characteristic (b) of the device sensitized with D102 dye.

For the nanotrees, between 350 nm and 750 nm, an average IQE of 35% compared to that of nanoparticles based devices of 27% (+30%) was

estimated. Devices with D102 organic dye (for experimental details see reference)[120] were fabricated to verify the outstanding performance increase in presence of an high extinction coefficient dye. In Figure 57 the LHE of the devices employing D102 dye are reported. When integrated, these spectra yield a maximum expected photocurrents of 9.22 mA/cm^2 and 6.87 mA/cm^2 for nanotrees based and for nanoparticles-based standard devices respectively (+34%). This is substantially confirmed in the actual value of short circuit current obtained in the best performing devices 7.02 mA/cm^2 and 4.76 mA/cm^2 for optimized nanotrees and standard nanoparticles respectively (+47%). Thanks to similar V_{oc} (0.91 V *vs* 0.89 V) and slightly better Fill Factor values (57.0% *vs* 50.5%) substantially higher (+66%) power conversion efficiency was obtained (3.96% *vs* 2.29%) in the case of devices fabricated with the nanotrees based photoanode architecture. It is worth to note that efficiency of PLD devices is among the highest reported for devices fabricated similarly with D102 dye and Spiro-OMeTAD.[121, 122] Moreover, it is even higher than the values obtained with volatile electrolyte DSSC in the previous works on similar photoanodes.[62, 65, 66] In order to probe the transport and recombination characteristics of the devices, measurements of photovoltage and photocurrent transient were performed on devices fabricated with D102 dye on 1.7 μm thick photoanode. In Figure 58 the charge lifetime as a function of charge density for standard nanoparticle-based photoanodes and for the PLD fabricated one is shown. The measurements are performed in open circuit and short circuit conditions. At open circuit the photogenerated charge decay represents the recombination characteristics of the devices; longer lifetime corresponds to lower charge recombination within the device. While the PLD nanotrees appear to exhibit slightly slower recombination at the same charge density, the differences are minor, and well within sample to sample variations. This is consistent with photoanodes exhibiting similar surface areas. At short circuit conditions, the photogenerated charge decay provides information about the time required for charges to exit the device. Again, the PLD-grown and the standard nanoparticle photoanodes behave very similarly, with overlapping points at high light intensities. This is likely due to the fact that despite the fact that larger crystalline domain size of PLD photoanodes should in principle boost electron transport, the high packing

density between the PLD branches, that also allows high surface area, is such that high number of interfaces between them is present.[90]
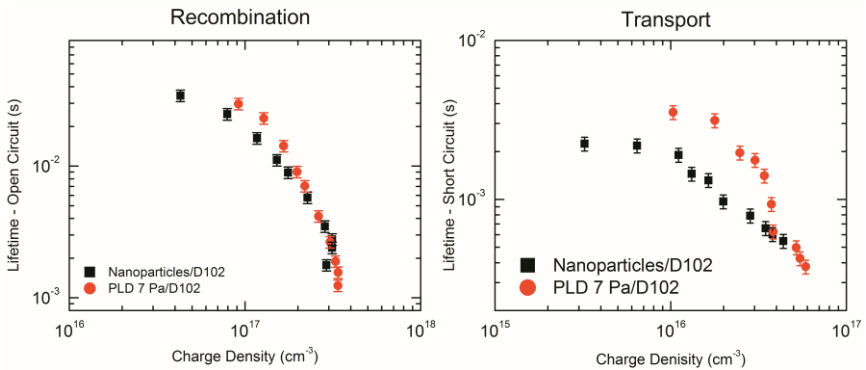
Figure 58 Photovoltage and photocurrent measurements of devices fabricated with standard nanoparticle photoanode and PLD fabricated one. The devices are 1.7 μm thick with Spiro-OMeTAD as HTM material and D102 dye.

Beside the similar behavior at equal charge density (chosen because of its more relevant physical meaning) at this point it is worth to note that, as a result of hyperbranced nanotrees higher optical density, the charge density at equal illumination intensity is increased for PLD photoanodes. This is thought to lead to better saturation of trap states and consequently to slightly faster electron transport. Enhanced optical properties are then leading to higher charge photogeneration and thus better photovoltaic performances.

Monolithic dye sensitized solar cells

Dye-sensitized solar cells (DSC), combining low fabrication costs and colourful design, [123] are making their way into the market as a design element with the added functionality of power generation rather than as a pure energy supply system. [124] DSCs have been demonstrated to work under diffuse [125] and artificial illumination and in non-standard condition of temperature. [126] They comprise dyed titanium dioxide thin film infiltrated with a redox electrolyte and enclosed within two transparent conductive oxide coated glasses (FTO-glass). [127] Even though in recent years power conversion efficiencies above 13% were achieved, [128] dye sensitized solar cells still struggle to breach into the market. Despite modules have reached power conversion efficiency in the order of 5 % dye sensitized solar cells are still struggling to break into the market of photovoltaic. A reduction in the costs of production, an increased power-to-weight ratio and a system capable of large scale fabrication are key to create successful commercial products. The monolithic dye sensitized solar (m-DSC) cells architecture offers several advantages. A monolithic device consists of FTO-glass coated with a porous multi-layered structure comprising a standard titanium dioxide film, an insulating spacer (typically Al_2O_3 or ZrO_2) [129] and a stacked counter electrode. The dye and the electrolyte are infiltrated once the solid structure has been fabricated. Only an FTO-glass support for the working electrode is needed since the counter electrode is directly deposited on top of the device. This design causes a consistent cost and weight reduction and a lower environmental impact. [130] [131] It also allow, through the control of the spacer thickness, to tune the inter electrode distance. Especially on large area, this could prevent ion diffusion issues that might arise on large areas due to electrolytes pockets formed by undulated glass. Since Grätzel and co-workers in 1996 have published his pioneering work, [132] several studies have reported on monolithic DSSC using both liquid electrolytes [133-135] and solid hole transporter. [136] The power conversion efficiency were respectively reaching values above 7% [134] and 3%. [136] In particular, liquid electrolyte m-DSC had a several micron thick black porous carbon film working as counter electrode (*i.e.* not transparent). Transparency was restored on these devices thanks to counter electrodes made of indium-doped tin oxide (ITO). This solution was adopted on solid state transparent m-DSC. ITO was deposited on top of a capping layer of solid HTM working in

place of the standard dielectric spacer. ITO was deposited either by sputtering [137] or by screen printing [138] and the obtained power conversion efficiency was close to 2%.
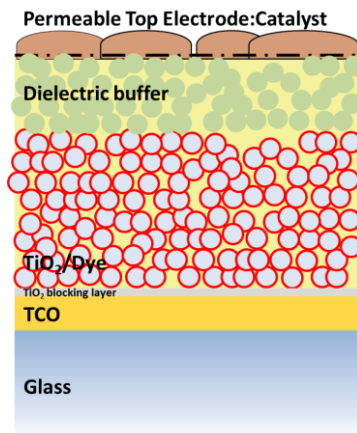
Monolithic DSC: Hyperbranched Photoanodes

In the case of the transparent m-DSC, ITO was deposited on top of solid HTM either by magnetron sputtering (using a semi-transparent metallic interlayer protecting the organic HTM from ballistic damage) [139] or by screen printing [138] obtaining power conversion efficiency close to 2%. Despite the wide variety of scaffolds studied in the literature of DSC, [32, 140] no one ever tried to implement more complex materials in order to improve m-DSC performances. In this section a hierarchical monolithic nanostructure entirely fabricated by physical vapour deposition methods is presented. The cell architecture is sketched in Figure 59 and is reported elsewhere in more details. [133] 8 μm thick film comprising an array of hyperbranched TiO_2 nanostructures (called hyp-TiO_2 in this section), as presented in previous sections and as used in other works for hybrid solar cells, [141] liquid [62] and solid state DSC, [142] is deposited by pulsed laser deposition (PLD) on a purposely etched FTO-glass. The film is covered with 9 μm of hierarchical Al_2O_3 (h-Al_2O_3) [143] by PLD onto which 800 nm thick ITO transparent conductive oxide and an ultra-thin (sub-monolayer) platinum films were deposited, by means of magnetron sputtering. This last FTO:Pt layer fulfils the roles of the counter electrode and

catalysts respectively. For the whole structure see field-emission scanning electron microscope, FE-SEM, image in Figure 59).
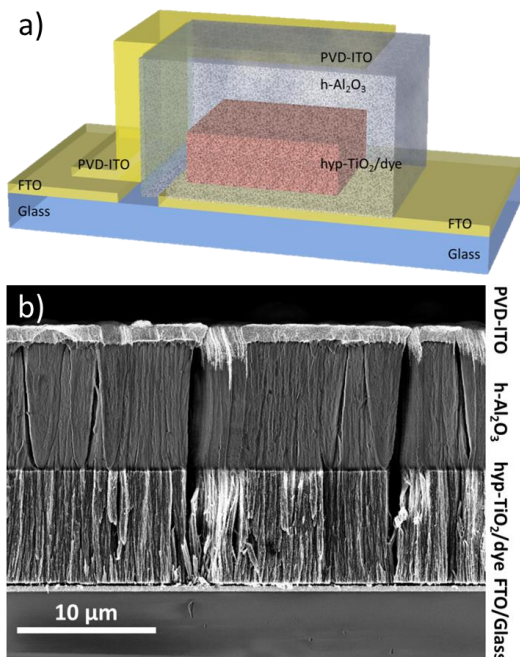
Figure 59 a) Monolithic DSC structural schematic b) Scanning electron microscope cross-section image of the monolithic transparent multilayer.

A set of electron microscope images can be found below. While magnetron sputtering is a well-established industrial technique, [144] pulsed laser deposition is often considered a fabrication technique for small-scale substrates. Recent advances in excimer laser technology [145] however have proven the true up-scaling potential. Treatable areas of laser deposition are limited only by the size of the vacuum chamber onto which the process occurs. [146, 147] With the devices studied presented here on the materials for m-DSC it is therefore envisioned the possibility of exploiting the precise control of physical vapour techniques over the morphology (*i.e.* functionality) of the nanostructures for photovoltaic applications.
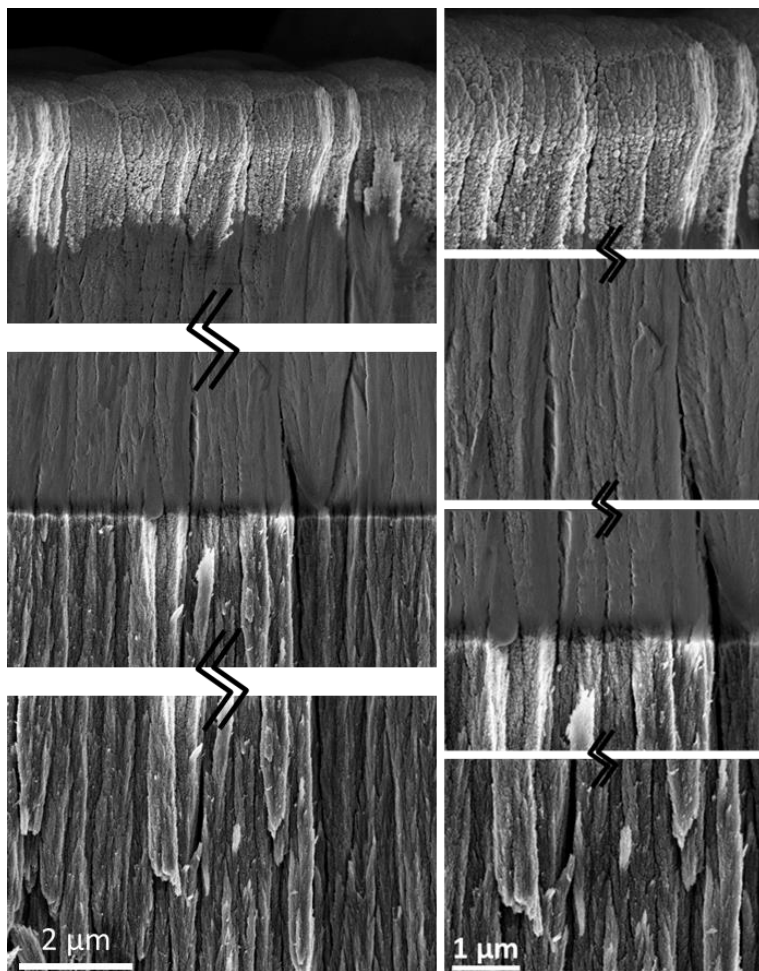
Figure 60 Details of the multi-layered structure in SEM images

The characteristic of hyp-TiO$_2$ were extensively described in the previous sections. h-Al$_2$O$_3$ instead porosity was optimized in order to (i) allow dye and electrolyte percolation, (ii) to avoid the contact between titanium dioxide and the ITO and (iii) to allow the deposition of porous-ITO still retaining good sheet conductivity necessary for electron transport. Oxygen-deficient and highly conductive ITO was deposited by means of magnetron sputtering in an

argon atmosphere [148] on top of the h-Al_2O_3 layer. ITO transparency is restored by post-deposition thermal treatment (2 hours at 500°C in air) [149].
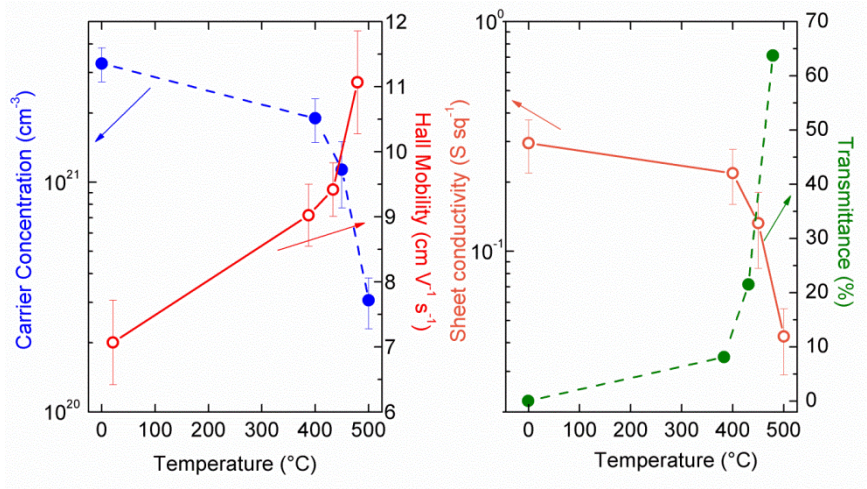
Figure 61 Optoelectronic measurements of Al_2O_3/ITO layers at different annealing temperatures.

Hall-effect set-up was used to carry out the electrical characterization on the 800 nm thick ITO film. The film of ITO was purposely deposited on an h-Al_2O_3 similar to that used in the m-DSC to make sure that the ITO morphology was the same of the one actually used in m-DSC. The values of resistivity, mobility and carrier concentration were found to be respectively 2.3×10^{-3} Ω/cm, 16 $cm^2V^{-1}s^{-1}$ and 1.62×10^{20} cm^{-3} (compared to 4.0×10^{-4} Ω/cm, 35 $cm^2V^{-1}s^{-1}$ and 3.0×10^{20} cm^{-3} of commercial, 250 nm thick, fluorine-doped tin oxide compact flat film). Despite the low mobility values resulting from to the presence of structural voids, the high carrier concentration allows the porous ITO to possess a comparatively low resistivity. As extensively described in the previous chapter for titanium dioxide, also the alumina undergoes an island organization. This dielectric buffer layer, acts as a template for the ITO which grows on top of its interconnected island[73, 74] leaving channels with sizes ranging from hundreds of nanometers to micrometers. The channels allow liquids infiltration when the DSC is fabricated.
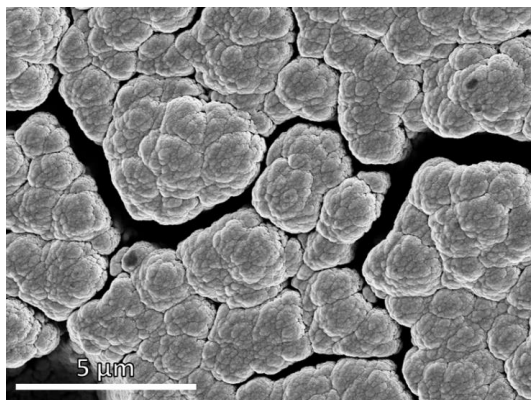
Figure 62 ITO deposited onto the alumina island. In this SEM top view image it is easy to see the cracks

Opto-electrical and morphological properties of the ITO are thus optimized and represent a trade-off between its conflicting roles in transparent m-DSC architecture. It has (i) good on plane conductivity, (ii) transparency and (iii) the possibility of dye-electrolyte system infiltration. Also here DSCs are fabricated using a commercial N719 dye and an iodide/triiodide liquid electrolyte from Dyesol.
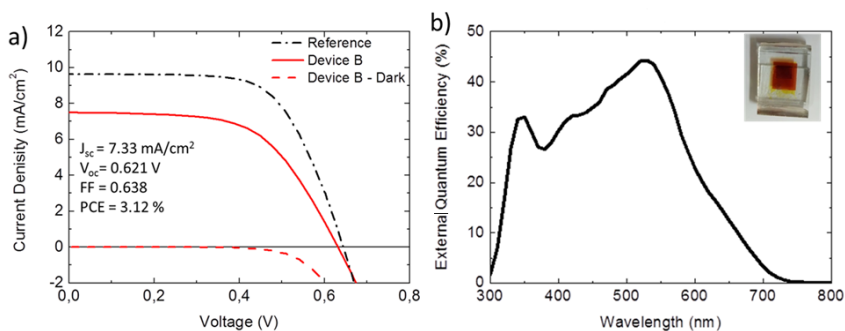
Figure 63 Photovoltaic performance of a transparent sensitized solar cell. a) JV curve under illumination AM1.5 of a monolithic device (red line, performance in the inset) compare to the one of a standard sandwich like DSC based on mesoporous nanoparticles and fabricated with the same dye and electrolyte. b) External quantum efficiency of the monolithic device.

The curve of J-V curve and the EQE are respectively represented in Figure 63. An overall efficiency above 3% (J_{sc} = 7.33 mA/cm^2, V_{oc} = 0.621 V, FF = 0.638) was measured achieving the highest efficiency ever reached with a transparent monolithic device (see picture of the device in the inset of Figure 63b). The dark current is plotted in Figure 63a (red dashed line) demonstrating the expected diode behaviour of the device. Remarkably the efficiency obtained with the monolithic architecture is only 25% lower than the one of a standard sandwich like counterpart (black dashed line) (J_{sc} = 9.63 mA/cm^2, V_{oc} = 0.660 V, FF = 0.651 efficiency = 4.07 %). More advanced systems employing higher extinction coefficient dyes and more efficient electrolytes [98] could allow the achievement of efficiencies in the range of 10%. Electrochemical impedance spectroscopy (EIS), measurements were performed at different illumination intensities with a sun simulator (AM1.5 solar spectrum) at the maximum power point of 0.48 V (see Figure 64). A series resistance (R_S) of 45 Ω was found proving the ITO counter electrode low resistivity. EIS measurements [138] at maximum power point under 1 sun illumination were modelled (see details in the methods section) and a charge transport time (τ_d) and a charge recombination time (τ_{rec}) of ~6 ms and ~48 ms were calculated. These two values led to an electron diffusion length (L) of about 21 μm. Increasing white light intensity, leads to a saturation of intra-bandgap trap states into the TiO$_2$ scaffold and thus, to an always faster diffusion time (Figure 64 solid lines). Recombination is less affected by light intensity and thus electron diffusion length increases (Figure 64 solid lines). Intensity modulated photocurrent spectroscopy (IMPS) and intensity modulated voltage spectroscopy (IMVS) were performed always at the maximum power point. These measurements were performed using a green (532 nm wavelength) monochromatic diode at different light intensities. As reported in Figure 64 diffusion and recombination characteristic time decrease with similar trends with illumination intensity. Despite the electron diffusion length of ~17 μm roughly confirms what found from EIS measurements, its trend with illumination intensity is not found for intensity modulated measurements. This behaviour, already observed in literature for this kind of measurements, [150] here can be due to the fact that the recombination is not affected by the green light as it does not photo-excite

the TiO$_2$ scaffold as the UV component contained in the AM1.5 spectrum directly does.
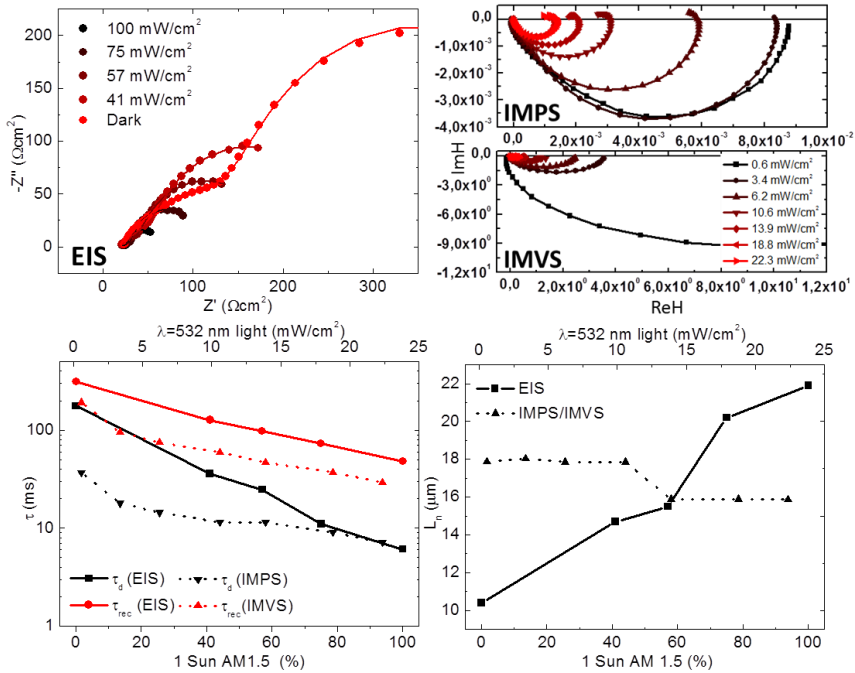
Figure 64 a) Electrochemical impedance spectroscopy (EIS) measurements performed under AM1.5 spectrum at different illumination intensities b) Intensity modulated spectroscopy (IMPS/IMVS) performed under 532 nm wavelength light at different illumination intensities c) Diffusion (τ_d) and recombination (τ_{rec}) lifetime measured by EIS and by IMPS/IMVS at different light intensities. d) Electron diffusion length (Ln) calculated from EIS and IMPS/IMVS measurements at different light intensities.

Differently from sandwich like device, the redox electrolyte in m-DSCs is impregnated within a 9 μm thick hierarchical Al$_2$O$_3$ film. This however does not hamper ion diffusion and mass transport of the redox reaction. The effective charge mobility within the device at higher illumination is preserved. The alumina spacer thickness can be further minimized, its porosity

maximised (reminding to avoid short circuit between the photoanode and counter electrode) to make ion diffusion more efficient. To quantify the influence of each layer on the overall transmittance UV/Vis spectrophotometer was used. The spectra shown in Figure 65 (normalized to the FTO glass transmittance) show that even after the deposition of a thin (≈ 3 nm) metallic Pt catalyst film above the ITO layer, the device still maintains a transmittance above 60%. The transparency of the whole multi-layered structure is strongly dependent on the selected dye and can be tuned to achieve the desired colour for the target application. [151-153]
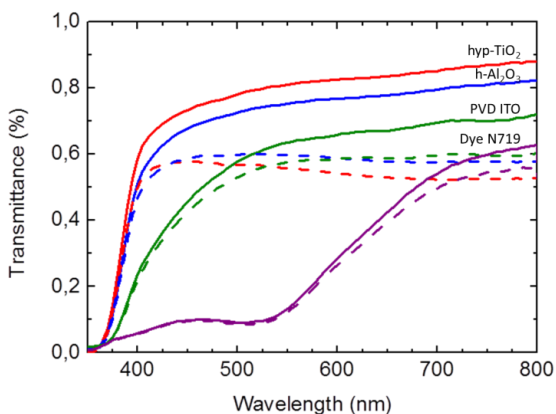
Figure 65 Optical analysis showing transmittance losses contributions for each component of the monolithic structure.
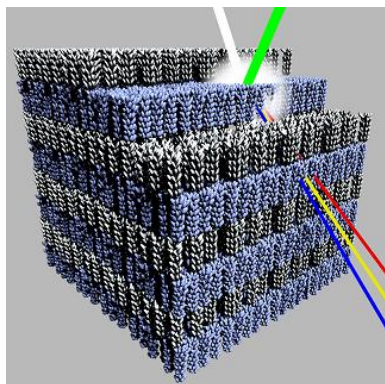
Photonic crystals:
Bright structural colour from functional morphology [154]

Butterfly wings, mother-of-pearls and opals are examples of natural photonic structures displaying structural colour. This arises from interference between light waves and a periodic or random sub-wavelength medium and determines a range of forbidden energies in transmission, known as photonic bandgap. When the structures are periodic, these materials are called photonic crystals. [155-161] Mimicking nature photonic structures with periodicity in one,[162, 163] two [164] and three dimensions [161, 165, 166] were realized. Several techniques (mainly spin coating, electrochemical etching, and physical vapour deposition, PVD) [165] can be employed to fabricate one-dimensional photonic crystals (also named as Bragg stacks). Refractive index contrast is obtained either varying the chemical composition of the layers or by controlling effective refractive index through the control of layers porosity. The realization of porous architecture represents a step forward in the exploitation of photonic crystals as it expands their potential function. Porous photonic crystals possess two great characteristics: (i) controlled mass transport of fluid analytes through interconnected porosity, and (ii) optical band structure engineering that enables the realization of tunable optical devices with potential applications in the fields of sensing, filtering, ICT (*e.g.* electro-optical switches), energy (sensitized solar cells), and photo-catalysis.[167, 168] The fabrication techniques of porous one-dimensional photonic crystals (p1DPCs) still lag behind the theoretical knowledge, and suffer for several limitations such as repeatability, scalability, and integrability. Fabrication methods for one-dimensional porous photonic crystals as well as for 2D, opals and 3D photonic crystals are reviewed in literature. [161, 169]

The most common top-down fabrication technique for p1DPC is anodic current modulation during electrochemical etching of conductive wafers (e.g. doped-Si, Al). [170-172] Pores size can be periodically changed from nanometers

to micrometers obtaining a multilayer structure. [173-175] This wet technique is limited to conductive materials and requires complex and multi-step fabrication achieving low refractive index contrast. To overcome this criticism a bottom-up assembly methods have been proposed to demonstrate what previously demonstrated by the theory. A number of different materials in nanoparticles colloidal dispersions [165, 167, 175, 176] were employed as p1DPC building blocks. Strong photonic bandgap efficiencies were obtained by using NP's material with intrinsically high refractive index and tuning particles size distribution with thickness of several micrometers (using two different materials) or of few millimeter (using structures based on opals). Spin coating processes, a cheap and flexible technique, was the preferred technique for the fabrication of these of devices. [177, 178] p1DPC was also fabricated from the gas phase via glancing angle deposition, [179, 180] a PVD technique capable of engineering different films architectures through shadowing of vapor atoms at highly oblique impact angles. Control over the porosity and thickness of individual layers is granted with the possibility to use different materials. In this paragraph, pulsed laser deposition is proposed as a novel fabrication technique for gas-phase self-assembled photonic hierarchical nanostructures. As the beetle cuticle, [181] self-assembly of different hierarchical porous materials is used to achieve refractive index variations and in turn the photonic bandgap. Hierarchical one dimensional photonic crystal (h1DPC) with 75% reflection efficiency in a 0.5 μm thick device and approaching complete reflection in a 1.5 μm thick device was fabricated using a single material (TiO_2). Structural density of hierarchical nanostructures can be controlled allowing fabrication of layers having different optical and morphological properties. When stacked onto each other they achieve peculiar optical functionalities. [62, 142] The hierarchical photonic nanostructures respond to fluid infiltration with photonic bandgap red shifting. PLD allow the realization of patterned photonic devices, on the scale of few μm, with interesting perspectives in the fields of solar cells, biochemical sensing, [182] photoelectrochemical water splitting, displays and photo-catalysis. The characteristic low thermal load of PLD process allows using even plastic or biological substrates. PLD decouples the chemistry from morphological parameters of deposited nanostructures that are controlled by the

background gas pressure.[62, 142, 183, 184] Refractive index contrast is obtained stacking layers of hierarchical nanostructures grown at pressures.
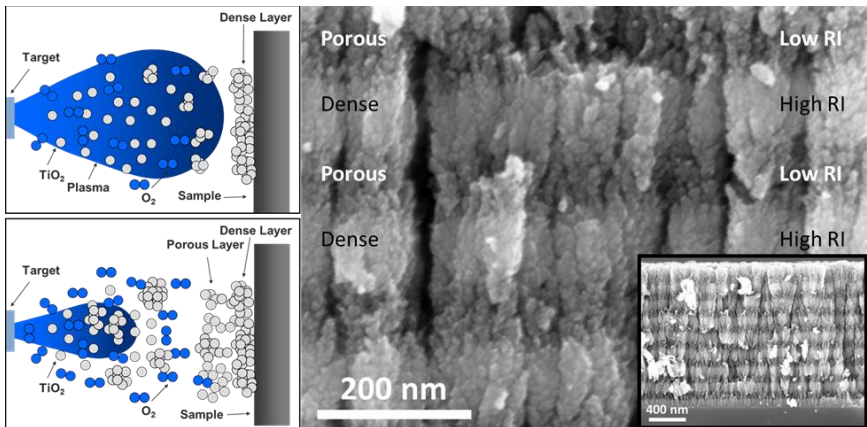
Figure 66 (Left) Schematic of layer formation by pulsed laser deposition. (top) In the case of low pressure a dense film is formed due to high energy species present in the plasma. (bottom) If the pressure is increased more porous material is deposited. (right) High resolution SEM showing details of the periodic layer stack constituent of the (inset) complete photonic crystals.

The SEM images of three h1DPCs fabricated modulating the effective refractive of porous titanium dioxide of self-assembled hierarchical structure are shown in Figure 67. The transfer matrix method (TMM) was used to simulate the transmission spectra of the three reported photonic crystals. The modulation of refractive index is due to the different porosities in the layers and it is fully accounted for by the simulations. h1DPC can be therefore designed and engineered with desired properties. The good agreement between measurements and simulations is testified by the matching between lateral fringes. If the substrate (glass-FTO) intrinsic losses (see dashed grey line) are taken into account, the reflection approaches 100% for sample c) which is only ~1.5µm thick. In Figure 67 the effect of porosity modulation on the two alternating, *i.e.* layer L1 (high n, low porosity) and L2 (low n, high porosity), comprising the photonic crystal repeating units are shown. The deposition pressure is kept constant for the layer L1 so to maintain constant

also its porosity in all the reported photonic crystals. The porosity of layer L2 was increased monotonically (increasing deposition pressure). This way the effective refractive index of L1 is kept almost constant, while the effective refractive index of the L2 decreases.
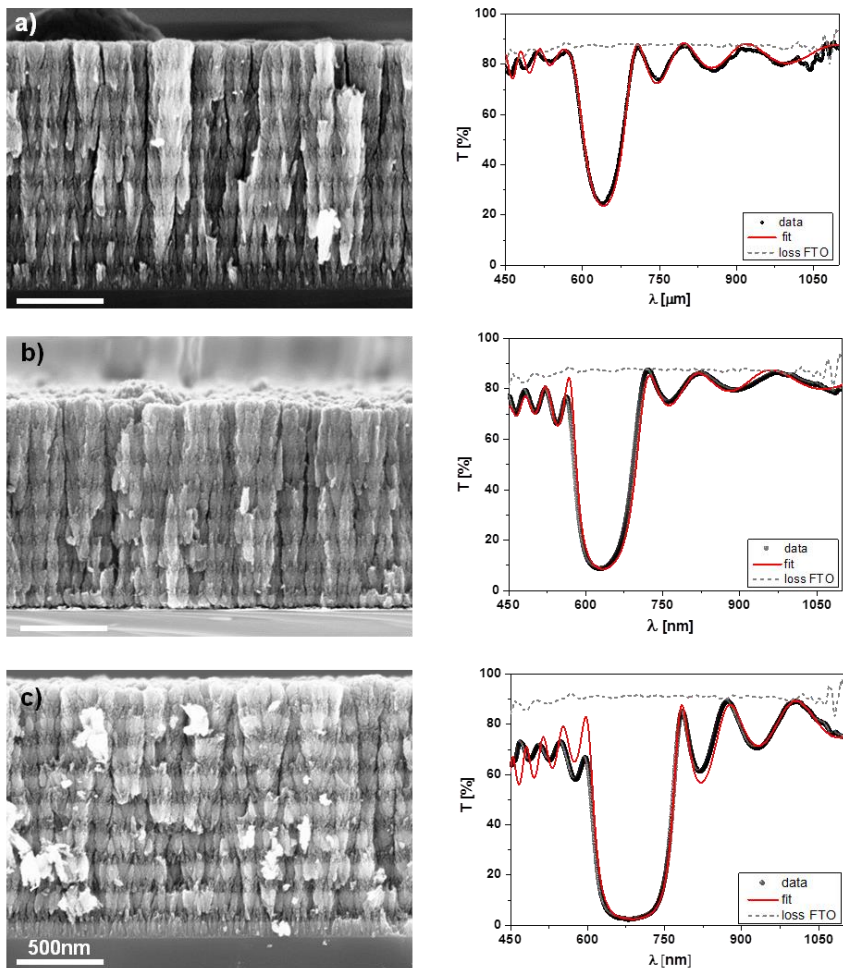
Figure 67 Scanning electron microscope images and transmission spectra (data and best fit) of three hierarchical photonic crystals in which the porosity of one of the two composing layers have been changed, by

changing the oxygen pressure in the deposition chamber. The pressure value are (5,7), (5,10) and (5,15) for sample *a)*, *b)* and *c)* respectively.

In Figure 68 the effective refractive index values and porosities are extrapolated from the TMM fit performed on experimental data are reported. The effective refractive index modulation approaches unity in the most extreme case of (L1, L2) being deposited at (5,20) Pa (not shown here) The refractive index contrasts $\Delta n_{(L1,L2)}$ reported in Figure 68 are $\Delta n_{(5,7)} \approx 0.4$, $\Delta n_{(5,10)} \approx 0.6$, $\Delta n_{(5,15)} \approx 0.7$ and $\Delta n_{(5,20)} \approx 0.9$). While the difference between the two effective refractive indexes increases, the reflection efficiency increases too and the photonic bandgap expands its bandwidth (FWHM).
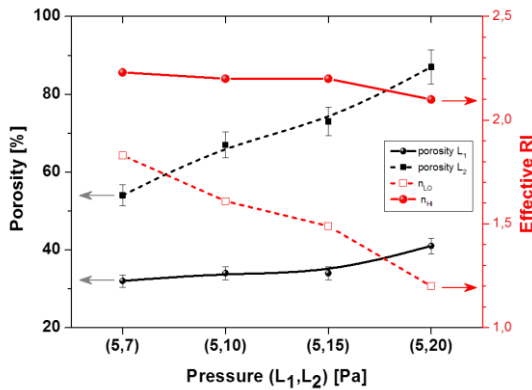
Figure 68 Porosity and effective refractive index (RI) of the two photonic crystal layers. L1 and L2 are the low and high porosity layer having respectively refractive index (nHI) and (nLO).

As reported in Figure 69a (SEM image) and Figure 69b (transmission spectrum), using the highest effective refractive index contrast, over 75% reflection efficiency is achieved with a ~460 nm thick TiO_2. The possibility of obtaining total reflection coupled with PBG tunability is demonstrated thanks to a white (reflection between 400 and 800 nm) h1DPC. This was realized by superimposing four TiO_2 h1DPC with complementary photonic bandgap (see Figure 69c and 69d). For all those applications (e.g. water splitting[185], perovskite and dye sensitized solar cells, sensors and optoelectronic switches)

in which the fabrication process implies high temperature steps the robustness of the optical characteristics of the photonic crystals is of great importance. h1DPC made by PLD were tested up to T=500°C without loss in their optical properties. Intensity was preserved while PBG position was subject only to a minor blue shift due to the structural shrinking occurring in the crystallization process (Figure 70).
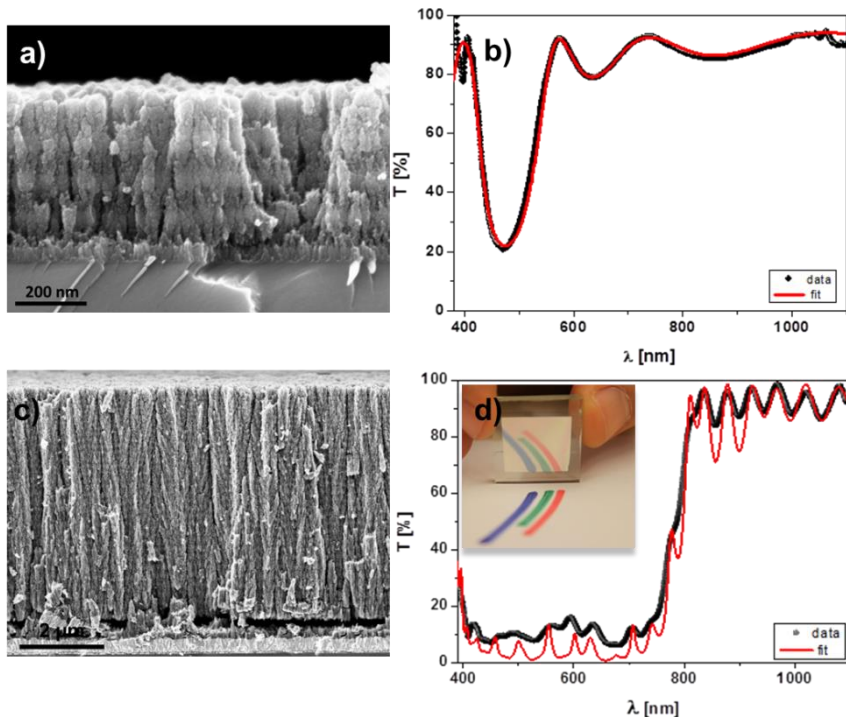
Figure 69 (a) Scanning electron microscope image and (b) transmission spectra (data and best fit) of TiO$_2$ hierarchical photonic crystals 460nm thick achieving over 75% efficiency. (c) Scanning electron microscope image and (d) transmission spectra (data and best fit) of TiO$_2$ porous photonic crystals with reflection band (R≈1) over the whole visible spectrum obtained by superposition of four different photonic crystals with different pitches. In the inset a picture shows the white mirror performance.

PLD however is a low thermal load process and therefore allow the deposition of h1DPC on flexible plastic substrate (Figure 70d). This could be interesting

for organic electronics. As shown in the previous chapter these nanostructures possess high RF. Always by chromatographic analysis on the desorbed dye The RF was found equal to 145 μm^{-1} for as deposited samples, while in annealed ones the RF decreased to 100 μm^{-1}.
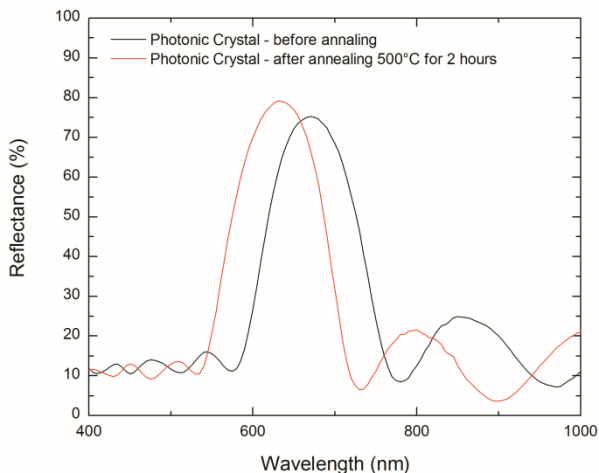
Figure 70 Effect of thermal annealing on the photonic bandgap of a PLD h1DPC.

With PLD is possible to realize patterned porous photonic crystals. In Figure 71a an example is reported where a h1DPC, placed off-axis with respect to the deposition source, was physically masked in such a way to obtain a letter pattern with a thickness gradient giving rise to a PBG red shift (from bottom to top) (Figure 71b). Using the same approach a pixel structure of h1DPC (pixel size of about 10 x 10 micrometers) was realized (Figure 71c). The pixel dimension is matching the requested pixel size in display technology and it could be appealing for achieving special sensing resolution.

The large oriented and interconnected porosity of h1DPC can be used for measuring refractive index of fluids, with possible applications in optoelectronic sensors[186]. In Figure 72a acetone (refractive index ranging from 1.354 and 1.364 in the considered spectral region) was causing a red-shift in PBG that in Figure 72b, upon its evaporation, was restored to its original position. In Figure 72c a similar effect is shown upon infiltration of E7 liquid crystal, that has an isotropic refractive index of about 1.575 in the

visible. The infiltration red-shifts the PBG and envisions the possibility to build devices for diverse optical applications, such as emitting diodes, lasing, sensors and photovoltaic cells.
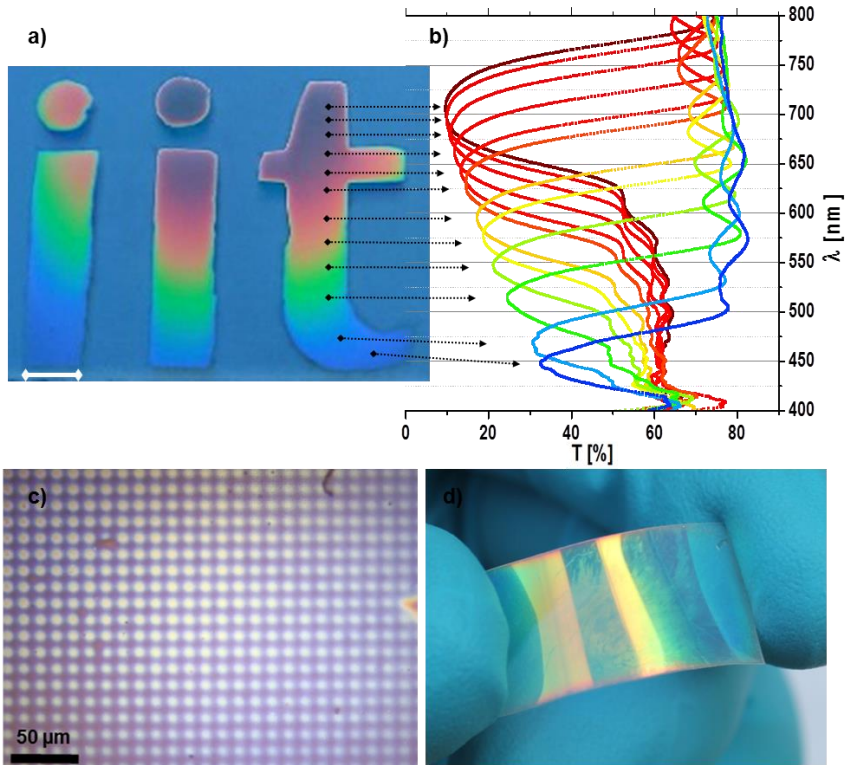
Figure 71 a) Patterned photonic crystal, fabricated with thickness gradient of the layers, by using a mask. Scale bar: 1cm. b) Transmission spectra of the photonic crystal along one of the letter, from top to bottom; a shift of the photonic band gap spectral position of few hundred of nanometers is shown. c) Pixel structure of hierarchical photonic crystal. d) h1DPC deposited on flexible plastic substrate.

The photonic bandgap can be widely tuned on a broad spectral range, notably down to the characteristic energy of telecom applications. A photonic crystal with bandgap centred at 1300 nm is reported in Figure 72d. High reflectivity photonic hierarchical nanostructures have been successfully fabricated by pulsed laser deposition. This was shown to be a new tool for nanophotonic

fabrication permitting: i) fabrication of photonic crystals with outstanding efficiency/thickness ratio; ii) optimal control of each h1DPC layer optical thickness; iii) patterning h1DPC structures with macro and micrometric dimensions simply by shadow masking iv) fabricating broadband dielectric mirrors. The process is compatible with thermal post-treatments as well as, being a low thermal low process, with plastic electronics.
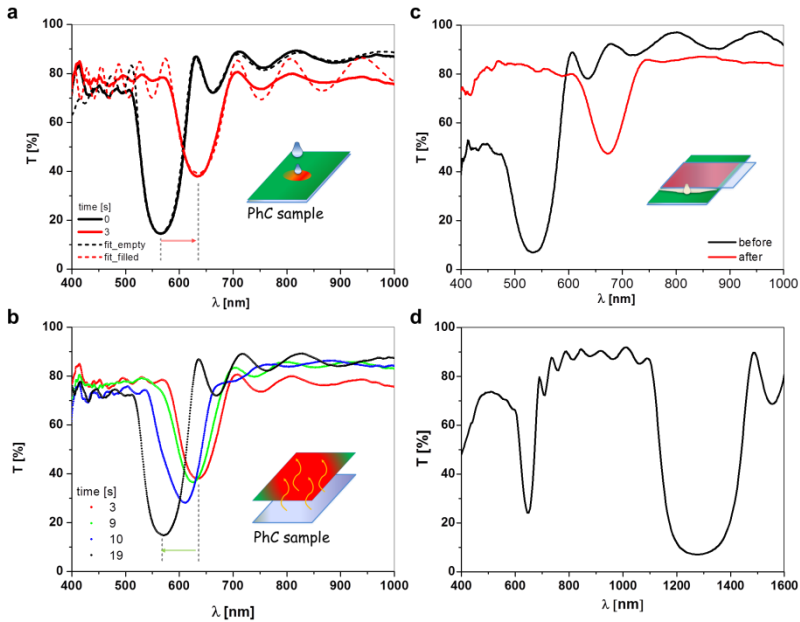
Figure 72 Measurements of transmission spectra of all TiO$_2$ hierarchical one-dimensional photonic crystal during the infiltration process a) with acetone (dashed lines denote transfer matrix simulations) and b) Transmission measurements of its subsequent evaporation; c) Measurements of the effect on the transmission spectra of the infiltration with liquid crystal; d) spectral response of sample with PBG in the IR spectral region.

Thanks to the control of the morphology of PLD materials, a vast number of applications, on both rigid and flexible substrates, and ranging from light harvesting to filtering to active materials such as lasers, or sensitized solar cells[187, 188] and colour pixels display technology [189] can be envisioned.
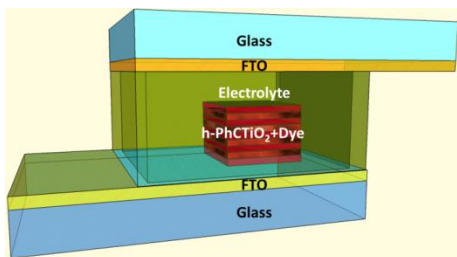
Figure 73 Scheme of a DSC fabricated with a photonic nanostructured photoanode

Structural coloured dye sensitized solar cells

In dye sensitized solar cells (DSC), photocurrent generation is carried out by the dye molecules chemisorbed on a mesoporous titanium dioxide photoanode. The dye molecules are regenerated by an electrolyte impregnated in the mesoporous photoanode and sandwiched between two transparent electrodes. [190] They represent an interesting alternative to traditional p-n junction solar devices not only for their lower fabrication cost and environmental impact but also for their interesting aesthetic. In fact, they are transparent and can be colourfully decorated by several types of dyes. [191] Generally the dye pigments have the role of absorbing the light, creating the characteristic colour of these devices, and of generating charges. The mesoporous titanium dioxide transports the electrons injected by the dye to the external circuit. This classical decoupling between light (dye) and electron management (titanium dioxide) was broken by the introduction of nanostructured materials [69] able to interact with visible light spectrum and affecting the light absorption of the device. [32, 70] Diffuse light scattering, [70, 192] controlled light back reflection [193, 194] and optical field confinement [195] have been exploited by introducing larger particles with high scattering cross section or by fabricating photonic nanostructures. One, two and three dimensional photonic crystals have been indeed used in dye sensitised solar cells. Three-dimensional photonic crystals such as inverse opals have been both as back reflector [196] or directly as sensitized photoanode [197] for dye sensitized solar cells. Despite these structures were able to enhance the light harvesting efficiency of the devices they showed low dye uptake due to a low specific surface area leading in fact to low photocurrent generations. Two dimensional photonic crystals have been demonstrated to increase light absorption through light channelling either by template patterning of the bottom of the TiO$_2$ photoanode [198] or by femtosecond laser ablation of a grating on top of the photoanode. [199] One-dimensional photonic crystals

(1DPhC) have been exploited with the aim of enhancing light-matter interaction to increase dye optical absorption and thus improve light-to-electron conversion efficiency. [200] Conductive 1DPhC counter electrodes, comprising alternating layer of ITO and SiO_2, were used as selective mirror able to reflect back in the dyed TiO_2 a desired portion of the visible spectrum enhancing the light harvesting efficiency while preserving overall transparency.[194] A similar effect was achieved by the monolithic integration of a TiO_2/SiO_2 1DPhC on top of the mesoporous titanium dioxide. [201] In this configuration the back reflection occurs immediately after the mesoporous layer avoiding parasitic absorption within the electrolytes in the previous case. 1DPhC being composed by densely packed nanoparticles can guarantee higher surface area and higher dye uptake. A more sophisticated photonic crystal, comprising only TiO_2 nanoparticles, was obtained by spin coating layers with periodic density (*i.e.* effective refractive index) variation. In this case the 1DPhC could be used directly as a dye scaffold. Optical field enhancement was studied to increase incident photon to current efficiency. [195] Photon flux management is key for performance improvement; [202] however as DSCs success lies also on their aesthetic, a SiO_2/TiO_2 photonic crystal overlayer has been used as source of structural colour. [203] Here it is demonstrated that it is possible to tailor structural colour of a DSC by tuning the spectral response of a photoanode comprising a hierarchical 1D photonic crystal (h1DPhC) fabricated by pulsed laser deposition (PLD). In Figure 74 SEM cross sections at different magnification of only one of this photonic crystal are reported as the bilayer thickness difference was not evident in the SEM images. It is shown how 3 µm thick h1DPhC photoanodes affect the devices optical characteristics without compromising their performances when compared to a device comprising standard mesoporous photoanode. In Figure 73 a sketch shows the device configuration. The refractive index (RI) periodic modulation (ΔRI≈0.6) [154] giving rise to the diffraction peak was achieved by changing the porosity of the hierarchical TiO_2. Material porosity in fact was varied between ~44% and ~58% (namely 5 and 10 Pa of pure oxygen of operating pressure). Porosities contrast was maximised to obtain a strong PBG while staying as close as possible to the value (7 Pa, 55% porosity) optimized in previous chapters. This was done in order to guarantee good electron transport properties and low charge recombination. [70] In Figure 75

the total transmittance spectra with a picture of the four samples are reported. Considering the FTO transmittance baseline the reflectance efficiency for all the h-1DPhC is higher than 75%.
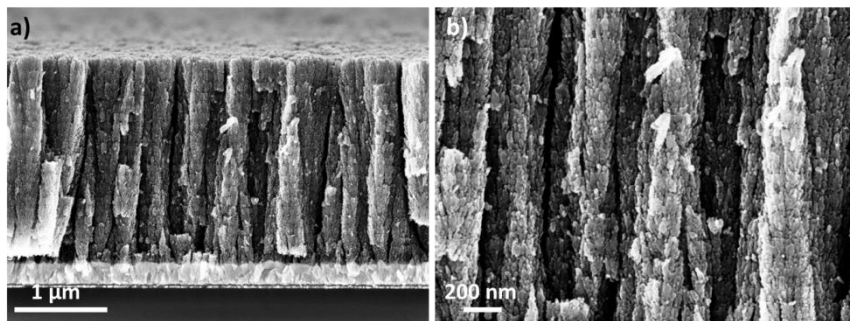
Figure 74 SEM cross section of a TiO$_2$ hierarchical photonic crystal used for the fabrication of dye sensitized solar cells.
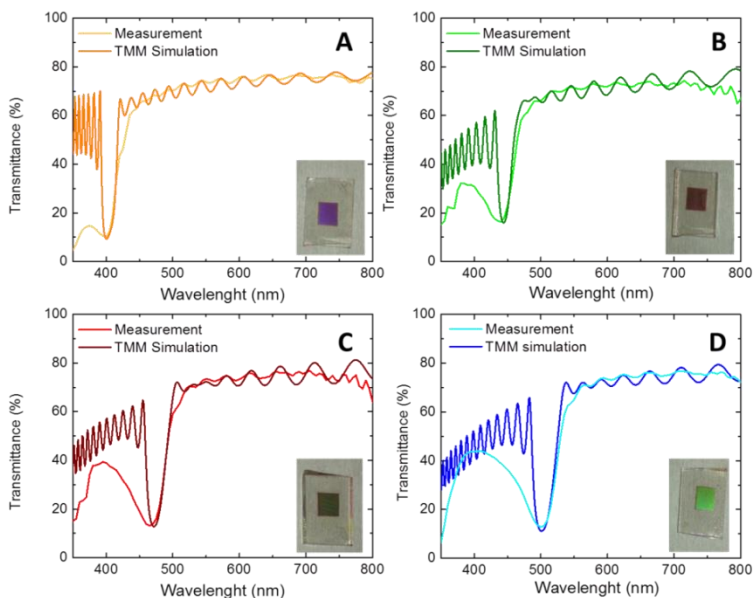
Figure 75 Measured spectra for four different h-1DPhC photoanodes with relative transfer matrix methods simulations. In the inset of each figure the sample picture is reported.

This PBG were measured in air (RI=1), as such it is important to have high optical efficiency in order to preserve a marked PBG also after electrolyte (RI≈1.3) infiltration. Transfer matrix (TMM) simulations were used to estimate the effective refractive index and thus the porosity of each layer. The numerical outputs of the simulations are reported in Table 4.

Table 4 Simulation parameters obtained by transfer matrix method (TMM) referring to the spectra in Figure 75

h-PhC Sample	Porosity high RI (%)	Porosity low RI (%)	Thickness high RI (nm)	Thickness low RI (nm)
A	44	56	23	81
B	46	57	24	99
C	46	58	30	102
D	46	58	35	107

Even though the scattering effect on the left-hand side of the photonic band gap is not accounted for in the TMM simulations, the accordance of the right-hand side PBG slope and the frequency matching of the interference fringes is testifying the accuracy of the simulations. [154, 195, 204] The porosities for the bilayer were found to be constant for each photonic crystal as expected from the fact that the same fabrication parameters were used among all h-1DPhC, varying only the bilayers thickness. In percentages they were found to be 45.5 ± 0.8 % and 57.3 ± 0.8 % for the high refractive index and for the low refractive index layer respectively. In order to obtain ~3 μm thick h-1DPhCs 25 bilayers were deposited for sample A as the pitch to obtain a PBG at 400 nm was thinner than those redshifted that were indeed fabricated using 20 bilayers. Despite the fact that focus of this study differs from maximising the power conversion efficiency, the photoanode thickness can be increased by increasing the number of bilayers. This will also result in a thicker and more efficient 1DPhC. [154] Device thickness and dye uptake were measured by scanning electron microscopy and by chromatographic measurements of the desorbed dye and were found to be respectively 2.8 μm and 0.97 nmol/cm^{2}μm for the reference photoanode and 2.7 ± 0.3 μm and 0.77±0.09

nmol/cm^{2}μm for the h-1DPhC photoanodes (details about device thickness, dye uptake and dye loading and unloading can be found in Table 5).

Table 5 Dye uptake per square centimetre per micron thickness, roughness factor, thickness, specific roughness factor and photonic band-gap of each photoanode compared to the reference

h-PhC	Dye uptake (nmol/cm^{2}μm)	RF	Thickness (μm)	RF/ μm	PBG (nm)
Ref - 3um	0.97	291.0	3.0	97 ref [70]	-
A	0.86	210.2	2.45	85.8	405
B	0.84	209.2	2.5	83.6	440
C	0.67	193.2	2.9	66.6	465
D	0.70	214.8	3.1	69.3	500

Dye sensitised solar cells were fabricated with N719 dye, iodide/triiodide electrolyte. Photovoltaic performances are reported in details in Table 6.

Table 6 Photovoltaic performance of dye sensitised solar cells fabricated with a photonic crystals with different photonic bandgap.

Device	V_{OC} (V)	J_{SC} (mA/cm^2)	FF	Efficiency (%)
Ref - 3um	0.640	4.93	0.75	2.4
A	0.686	4.95	0.67	2.30
B	0.673	5.76	0.67	2.63
C	0.676	5.79	0.68	2.69
D	0.673	6.90	0.70	3.26

DSC power conversion efficiency was 2.4 % for the reference device while was on average 2.7 ± 0.35 % for the h-1DPhC DSCs. The standard deviation (± 12

%) on device efficiencies can be related to that on photogenerated current (± 13 %) that is in fact related to the different dye uptake values (± 13 %). Despite the higher surface area of the standard photoanode, h-1DPhC photoanodes have higher power conversion efficiencies due to higher photogenerated current densities. This improvement was already observed in a previous work and can be ascribed to the scattering induced by PLD hierarchical structures. The PBG modulate the external quantum efficiency as shown in Figure 76.
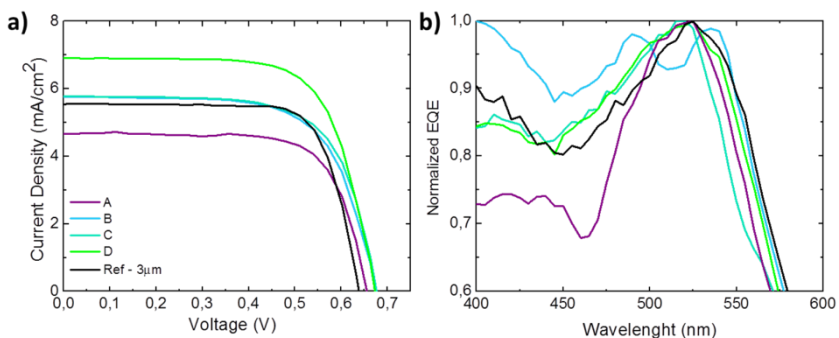
Figure 76 a) Current density versus voltage of the dye sensitized solar cells using photonic crystals as a dye scaffold are compared to a reference device 3 μm thick.

As can be noted all the diffraction peaks are redshifted and slightly less efficient than those reported in Figure 75. This was expected as the infiltration of the liquid electrolyte caused an increase in overall effective refractive index of the device. The EQE modulation demonstrates how it is possible to tune the spectral response of h-1DPhC photoanodes still obtaining better performances than a standard mesoporous photoanode. The reflectance of a green h-1DPhC DSC sensitized with red N719 dye is reported in Figure 77 together with a picture of the complete device. Once again the peak is less efficient than the peak shown in Figure 75 as a consequence of the electrolyte infiltration. The DSC colour is thus decoupled by the coloration of the dye pigment. This effect could be exploited to enhance aesthetical appealing of dye sensitized solar cells as well as possible light management tool.
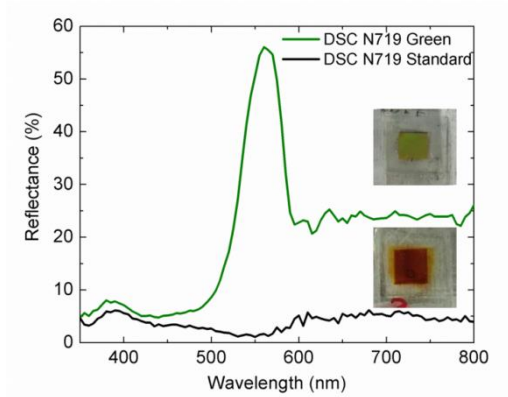
Figure 77 Reflectance spectra showing the structural colour of two DSCs comprising a 3 µm thick photonic crystal scaffold are compared to the one of a standard scaffold DSC.
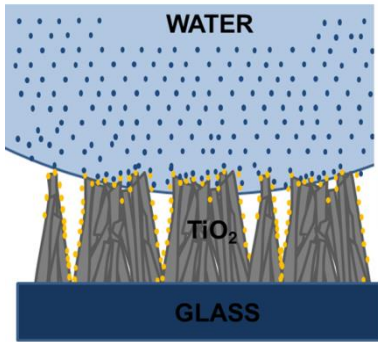
Superhydrophobic surfaces:
Exploiting surface modifications for wetting control[74]

Due to the large number of possible applications, in the last decades superhydrophobic surfaces have gained the attention of both the industries and of the scientific community. Self-cleaning surfaces, [205] microfluidic device,[206-208] anti-icing coating[209-212] and anti-fogging coatings, [213] are among the most common application. A liquid drop is deposited on a superhydrophobic surface forms a quasi-spherical drop and a high contact angle (CA) is observed. In this case a low interfacial surface area is present. Ideally the liquid does not wet the surface and it is free to roll-off. This property is caused by solid surface energy being lower than the one of the liquid droplet. The former condition is achieved either by acting on the chemical composition of the material or on its physical characteristic both by acting on the nanometric roughness and on its micro-sized features. An complete review of the descriptive models of this complex phenomenon together with fabrication methods of superhydrophobic surfaces are found in *Yan et al (2011).[214]*

The so called Wenzel[215] and Cassie-Baxter[216] models are the two most known models for describing superhydrophobic surface wetting modes. The former describe the interaction between a rough surface and a droplet that is wetting it down to its grooves, the latter, allows higher contact angles, and include the triple interface between the solid surface, liquid droplet and the gas trapped inside the surface groove. Cortese *et al* [217] reports the triple interface as a consequence of a dual scale groove allowing the coexistence of large surface area and voids for gas pockets formation underneath the droplet. At this occurrence the droplet is free to float on the surface with poor adhesion and thus it is free to roll-off.

In the field of nanostructured materials several nanostructured materials were studied to match the above requirements.[218] High surface area nano-materials have been engineered using raspberry-like nanostructures[219] or simply collecting candle soot eventually used as template for

superhydrophobic surfaces.[220] Lithography has been employed to fabricate materials having a controllable periodicity[221, 222], allowing the instauration of a robust Cassie-Baxter interfaces. *K-C Park et al. (2012)*[222] worked on the optical and wetting properties of silicon dioxide nanoposts. These were studied as a function of nanoposts aspect ratio and packing density. Hierarchical nanostructures with both large surface areas and the structural periodicity needed by Cassie-Baxter state have been obtained either by nano-sized particles[223, 224] decoration of lithography patterned structure template or by a multistep hydrothermal process [225] leading to film similar to the one obtained by PLD. In this paragraph an array self-assembled hierarchical architecture of TiO$_2$ fabricated by Pulsed Laser Deposition is sensitized with a fluorinated (perfluoro nonanoic acid, PFNA). The chemical sensitization was kept constant throughout the experiment while the morphology of several self-assembled PLD deposits are studied and related to hydrophobic behavior. This way the physical phenomena leading to different wettability mode are studied. Pulsed laser deposition allows the control of the surface morphology at both the nano and micro length scale. This paragraph explores how different surfaces can be exploited to induce different wetting behaviors. The aim is two-fold: to control superhydrophobic surfaces behavior through the understanding of how the morphology causes different wetting properties. TiO$_2$ samples are dipped in a 0.5 M solution of PFNA in ethanol for 30 minutes. PFNA is composed by a carboxylic group and by a hydrophobic fluorinated long chain. As described in the previous chapter, the films comprise an array of structures, resembling a tree shape. Long braches (tree-branches) comprising nanoparticles (leaves) stretch out from micro pillars (trunks). The two equations governing the Wenzel and Cassie-Baxter models are respectively:

$$\cos\theta^W = RF\cos\theta^*$$
$$\cos\theta^{CB} = \varphi_s\cos\theta^* - (1-\varphi_s)$$

θ^W and θ^{CB} are the contact angles in the case of Wenzel or Cassie-Baxter wetting mode respectively, θ^* is the Young CA, *RF* is the roughness factor and ϕ_s is the surface ratio described *Methods* in Figure 87. Wenzel mode is governed by a nanometric roughness *RF*, Cassie-Baxter is instead controlled

by ϕ_s which is more related to the grooving of the surface In the structures deposited by PLD the surface modifications involve either a change of the roughness (tuned by deposition pressure), or a micro inregualarity between nanostructures and void channels (tuned by nanostructures stacking density) or even a combination of these two effects. Wenzel surfaces are "sticky" surfaces while Cassie-Baxter surfaces allow the drop to float with no adhesion. In Figure 78a the CAs are plotted as a function of the film thickness for different deposition pressures. In Figure 78b the roll-off angles (*i.e.* the minimum sample tilt angle at which the droplet roll-off the surface) are plotted.
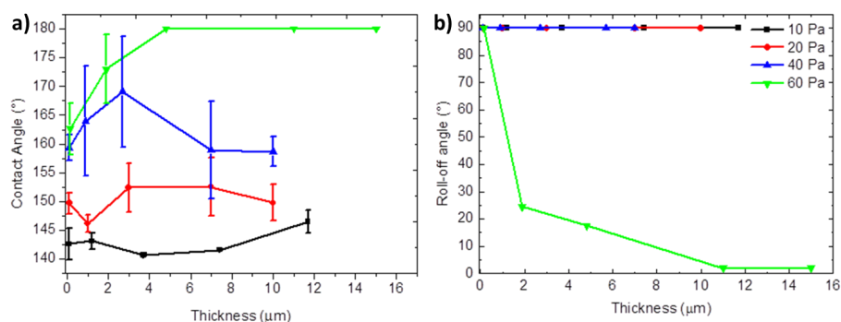
Figure 78   (a) Contact angles and (b) roll-off angles values of film with different thickness and deposited at different background gas pressure, namely (black) 10 Pa, (red) 20 Pa, (blue) 40 Pa and (green) 60 Pa.

Contact angles follow a general trend and increase with deposition pressure and film thickness. A sharp switch from no-roll-off and roll-off occurs above certain film thicknesses for samples deposited at 60 Pa (Figure 78b). As reported in literature[67, 68] and as studied in the previous chapter PLD deposition pressure is influencing the surface roughness. This justifies the dependence of wettability upon pressure changes. Passing from to 100nm to thicker film the difference in wettability increases suggesting that another structural modification (other than a simple nanometric roughness enhancement) is playing a role when film are grown thicker. This is the case of the already described island reorganization, as shown in the top view SEM images in Figure 79. Despite a nanometric roughness change is observable at high magnifications; micrometric features become evident on larger areas.

This can be seen in the complete SEM analysis reported in Figure 34, 35, 36 and 37.
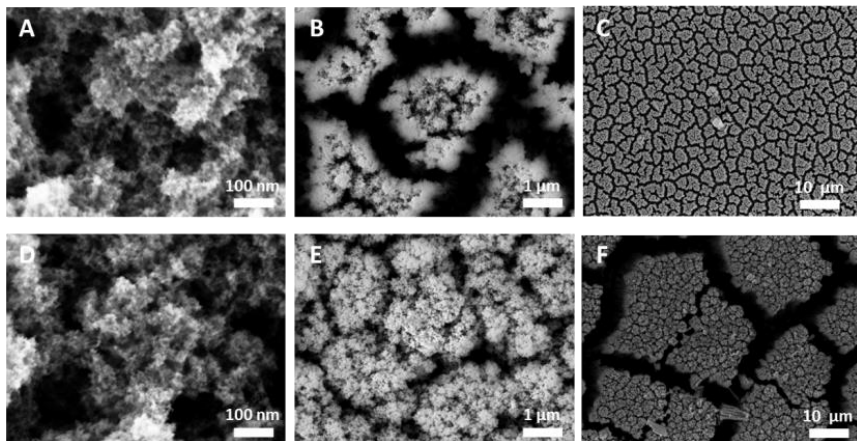
Figure 79 SEM top view images of (A, B and C) samples deposited at 10 Pa and (D, E and F) samples deposited at 60 Pa.
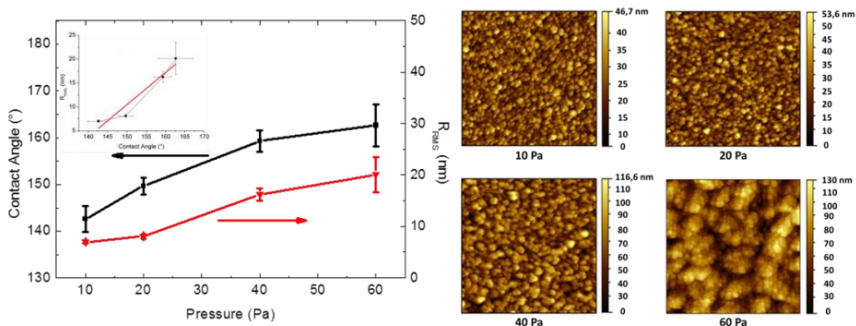
Figure 80 (Left) Contact angle (black line, left axis) and root mean sqaure roughness R$_{RMS}$ (red line, right axis) are plotted for 0.1 μm samples deposited by PLD at different background oxygen pressure, namely 10, 20, 40 and 60 Pa. In the inset the contact angle is plotted *versus* R$_{RMS}$. (Right) AFM images of the same sample surfaces. AFM scan area 1.5 by 1.5 μm. R$_{RMS}$ was estimated on a 500 by 500 nm area.

Nanometric roughness was quantified by means of an atomic force microscope. AFM measurements were performed on 0.1 μm thick samples

deposited at different pressures. In Figure 80 the root mean square roughness (RRMS red lines, right axis) is reported together with the contact angle values (black line, left axis). All these samples do not present micro grooves and are in a Wenzel wetting mode (as expected looking at SEM image of those surfaces). The curves are mostly parallel highlighting the linear relation existing between R_{RMS} and CA (see inset). The same characterization was performed for a similar set of samples this time 3 μm thick. The root mean square roughness (R_{RMS} red lines, right axis) is plotted in Figure 81 together with the contact angle values (black line, left axis). Despite the CA still has a positive trend with deposition pressure, the linear relation between contact angle and R_{RMS} is lost as the island reorganization is introduced. Overall this phenomenon is decreasing the wettability of surfaces.
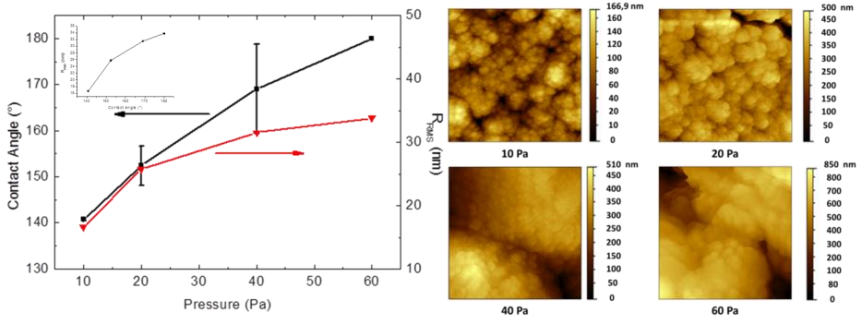
Figure 81 (Left) Contact angle (black line, left axis) and root mean sqaure roughness R_{RMS} (red line, right axis) are plotted for ~3 μm samples deposited by PLD at different background oxygen pressure, namely 10, 20, 40 and 60 Pa. In the inset the contact angle is plotted *versus* R_{RMS}. (Right) AFM images of the same sample surfaces. AFM scan area 1.5 by 1.5 μm, R_{RMS} was estimated on a 500 by 500nm area.

The change in wettability is not anymore caused simply by the R_{RMS}. As in *Di Fonzo et al.* (2010)[143] and as reported in the previous chapter at high deposition pressures a lowering in nanotrees stacking density is driving a reduction in structural hardness. Being denser packed they have less space to collapse and less pronounced void channels will form leaving a uniform surfaces. Decreasing density (*i.e.* lowering deposition pressures) a violent

collapse of the nanotrees upon sensitizer solution evaporation leads to a marked islands formation and to a micro cracking (micro voids formation). The power law correlation is found between nanotrees height and island average dimension[73] can be used to tune the surface ratio and in turn the wettability. This self-collapse phenomenon is depicted in Figure 32 in the previous chapter for matter of clarity. There a green line is used to underline the island formation. Cracks are indeed the regions where air pockets are formed inducing the transition between Wenzel and Cassie-Baxter wetting mode. Using the top view SEM images it was possible to assess the surface ratio (as described in the method section). The values of surface ratio are reported in Figure 82 for samples with thin films deposited at different thickness and deposited at different pressure. The surface ratio decreases with increasing pressure (*i.e.* decreasing packing density) and with thickness (*i.e.* decreasing structural stiffness).
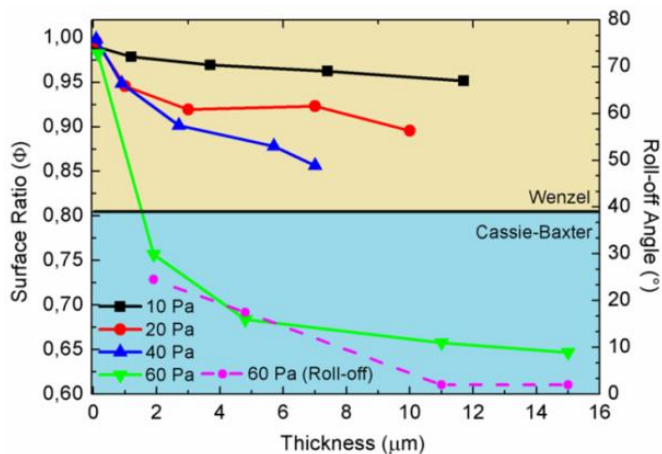
Figure 82 (Solid lines, left axis) Surface ratio values of samples with different thicknesses grown at 10, 20, 40 and 60 Pa. (Dashed line, right axis) Roll-off angle for samples deposited at 60 Pa. Other samples presents high water adhesion even at 90° tilt and for these reason are not plotted.

Only if void channels between islands allow the formation of triple interface (*i.e.* liquid-air-solid) the Cassie-Baxter wetting mode is forming and a roll-off angle is observable also at tilt angles below 5 degrees. The decrease in roll-off

angle can also be related to a decrease in surface ratio. Surfaces with low adhesion can be used to engineer self-cleaning materials. Brick powder was spread on top of a low adhesion and superhydrophobic surfaces and some water was poured. The water removed the powder rolling off leaving a clean surface behind. A snapshot sequence of the self-cleaning is reported in Figure 83 (right).
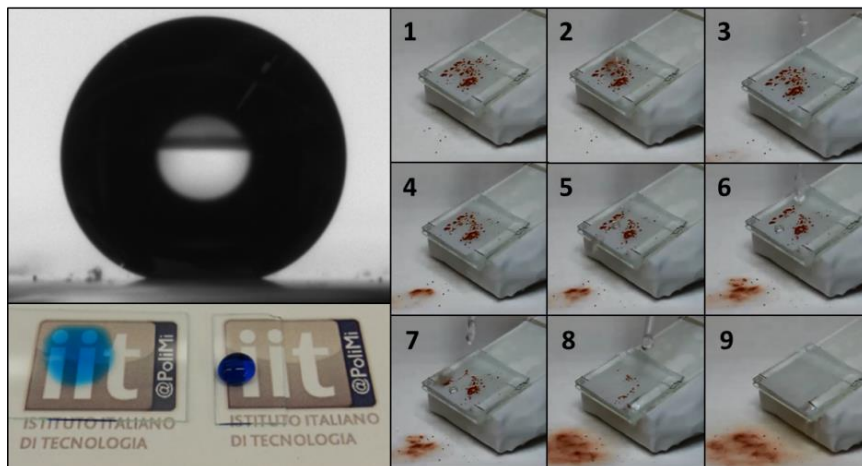
Figure 83 (Left top) Drop profile as seen at the contact anlge instrument, (Left bottom) two drops of coloured water are deposited on bare glass and superhydrofobic glass by PLD to demonstrate transparency of the PLD surfaces. (Right) Snapshot sequence of the cleaning process of a superhydrophobic surface

Self-cleaning properties is of paramount importance for photonic applications operating in outdoor or dusty environment in order to sustain their function with no alterations. For these reasons in Figure 84 the transmittance (total and diffused) spectra of samples deposited at different pressures are reported. Looking at the total transmittance (left column) it is clear that all the 100 nm thick samples are transmitting more than 90 % of the whole visible spectrum with the typical cut-off around 320 nm in the region of the absorption band of titanium dioxide. As the films grow thicker losses start occurring around 400 nm and the total transmittance appear to be lower

along the whole visible spectrum. Looking at the right column of Figure 84 a trend is reversed, in fact thicker films show stronger scattering properties. This could be the reason behind the lower total (*i.e.* direct plus diffuse transmittance) transmittance along the visible spectrum. This has to be attributed to measurement artefact occurring for diffusive film. The light is channelled in the glass substrates onto which the titanium dioxide films are deposited and is not collected by the sensors within the integrated sphere. The increase in scattering cross section with increasing thickness is thought to be due to the island reorganization described in the previous section. Micrometric islands in this situation act as scattering element diffusing the light. Thicker and less dense films promote island formation and enhance light scattering. This is clearly visible looking at the diffuse transmittance of 3 μm thick films and at how this is increasing for samples deposited at higher pressures. In the extreme case of very thin films (100 nm) island reorganization does not occur (or at least cannot occur at a micrometric level) and the films present very low scattering cross-sections. Transparent and hazy films can be thought as possible overlayer for photovoltaic device to enhance light interaction while keeping a clean interface.
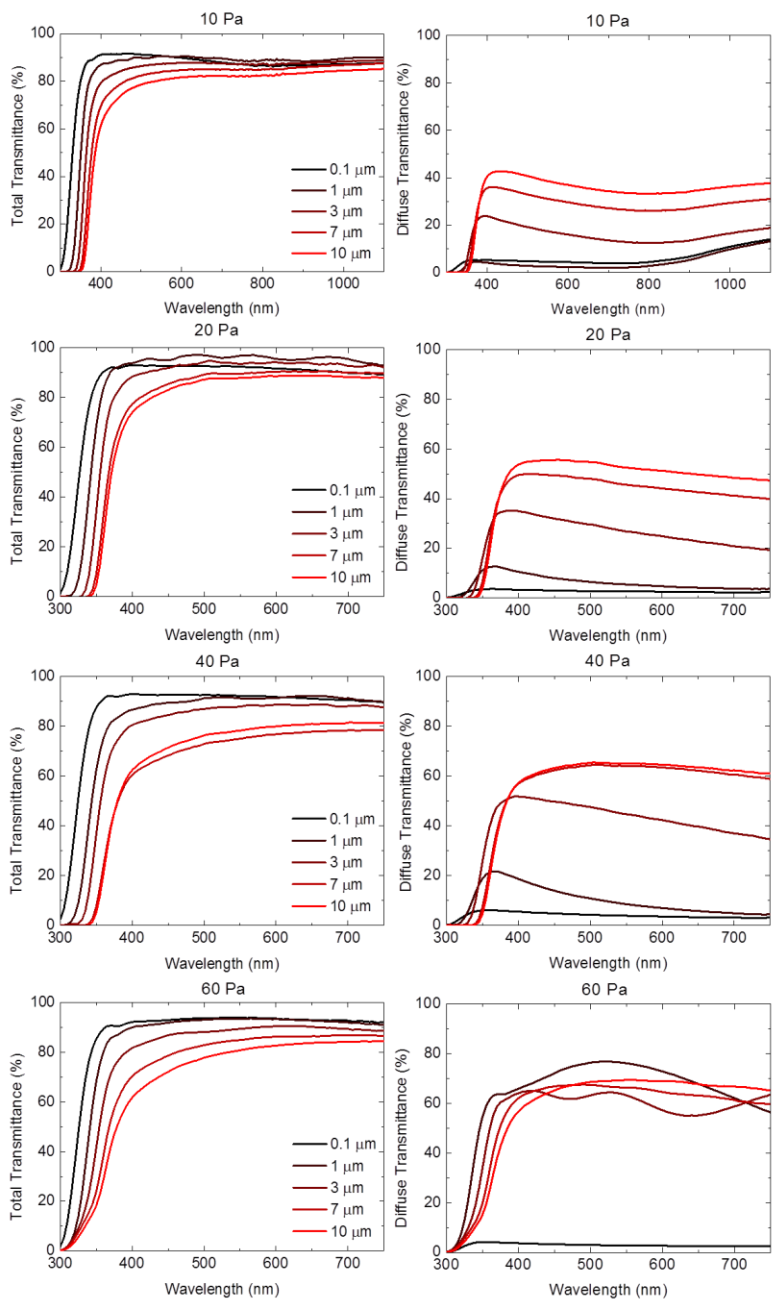
Figure 84 Spectrophotometry of titanium dioxide films deposited at different pressures. (left column) Total transmittance and (right column) diffuse transmittance spectra of samples with different thickness.

Chapter 4

Conclusions

Disruptive technologies enabled by nanomaterials are leading industrial innovation in fields ranging from agriculture and food, to drug and medicine, to energy and photonics. For examples, coloured and semitransparent photovoltaic materials work thanks to their active structure being as thick as the incident light penetration depth and the electron diffusion length, photonic crystal modulate light flow thanks to a dielectric constant spatial modulation in the order of a quarter of the wavelength, or superhydrophobic structures have reduced wettability as they can lower their surface free energy at the interface with the liquid at a molecular scale. In order to obtain nanomaterials, several fabrication techniques were implemented either following a top-down or a bottom-up approach. Among many techniques falling in the former approach, anodic etching has been widely used to selectively etch materials leaving elongated structures called nanotubes. Lithography, as well as, femtosecond laser ablation, can obtain complex micro patterning by precisely and selectively removing materials while leaving untouched other respectively by selective chemical reaction or physical ablation. Despite the industry still heavily relies on these techniques for several applications (e.g. microelectronic), top-down approach has a major drawback in the fact that it is intrinsically bound to a template material from which it must extract the desired micro or nanostructure. The fabrication and the properties of the template in turn limit the possibilities of the final product; anodic etching can only be applied to conductive materials, lithography to reactive layers and femtosecond laser ablation to a specific set of materials. These limitations are not present in bottom-up fabrication methods. The latter's are additive manufacturing techniques rather than subtractive and relate these in a similar fashion as 3D printing does with fabrication methods of standard objects. Among bottom-up approaches physical vapour deposition (e.g pulsed laser deposition) comprises a set of techniques that exploit evaporation to transfer a material in the gas-phase from a source to a target. In this context, *this Ph.D. thesis* entitled "Titanium dioxide hierarchical nanostructures for photonic applications" explored the potentiality of pulsed laser deposition (PLD) in material nanostructuring for photonic applications. Titanium dioxide (TiO_2) is a fascinating large band-gap semiconductor material. TiO_2 is abundant in nature, biocompatibility and possesses outstanding properties such as efficient electron transport,

transparency, photocatalytic activity. Pulsed laser deposition is used to tailor its structural properties. By changing process parameters it was shown that is possible to tune the kinetic of recondensation of the laser vaporized titanium dioxide. In particular it was demonstrated how the clusters ejected from the source materials upon laser ablation reacts to the oxygen partial pressure within the deposition chamber and how this can eventually be used to control the kinetic of cluster reorganization into different nanostructures. Materials were structurally characterized in order to study their characteristics and to gain insight of how process parameters were affecting them. A wide variety of characterization techniques such as SEM, TEM, XRD, RAMAN and BET were employed to fully characterize the materials. While in low oxygen conditions, highly energetic spices are forming compact films, high oxygen pressure are employed to induce cluster scattering and to control the consequent formation of more complex hierarchical nanostructures. Nanometric features attached to branches departing from a main vertical trunk give to these structures high specific surface that increase with porosity at higher deposition pressure. Higher effective surface area per geometric surface area (roughness factor) was found in dense hierarchical materials, that are therefore of interest for all those application where interfacial phenomena are crucial. Besides causing high roughness factor, material density is responsible for a particular crystallization. Thermal energy provided to dense hierarchical structures during thermal annealing was shown to start an energy minimization process leading to the formation of crystalline structures as long as hundreds of nanometers (hyperbranching). In turn crystallization process parameters were used to further tailor the nanostructures. Thermal annealing does not only change nanometric feature size but, dependently on initial morphology, it strongly effects the pores size distribution. The overall pore volume is decreased as an effect of thermally induced Ostwald ripening. In fact nanocrystalline average grain size increases driving a suppression of nanometric pores that increases the average pores size and reduce the overall volume. Exploiting the morphology control, hierarchical one dimensional photonic crystals are obtained by periodically modulating the nano-structural effective refractive index through the modulation of the density. Alternatively if the porosity is left constant hierarchical nanostructures grow with an inverse conical envelop with lateral dimension

of few hundreds of nanometers and they act as an array of Mie scattering elements forming a hazy film. Hyperbranched nanostructures were employed as photoanodes in standard liquid and solid state dye sensitized solar cells. Scattering hyperbranched nanostructures are shown to improve photovoltaic performances thanks to an enhanced optical density and more efficient charge extraction. Similar structures upon effective refractive index modulation form hierarchical one dimensional photonic crystal and are used as photoanodes for structurally coloured solar cells. Hierarchical photonic crystals are also envisioned in light of possible applications in the field of active matrix displays, sensing devices and optical materials for telecommunication. Eventually it is shown how the study and the control over hierarchical nanostructures morphology had a fall-out in the wettability control. Transparent self-cleaning surfaces are studied as a possible overlayer for those opto-electronic devices operating in outdoor environments such as photovoltaic solar cells that might be operated in outdoor or dusty environments.

Outlook

The characterization of several nanomaterials fabricated by PLD led to the good knowledge and the full control over titanium dioxide nanostructures morphologies. The implications of different morphology on optoelectronic properties were shown through the study and development of a set of applications ranging from photonic devices such as solar cells to ultrahydrophobic self-cleaning transparent materials. Among the vast number of studies that could be performed along the same research path I personally envision three main directions: (i) fundamental research, (ii) additive research (iii) technology transfer. Fundamental research can be done to understand how crystalline domains evolve from the plasma to the final state and how they can be modified to enhance surface reactivity through the induced exposure of facets with higher surface energies. Additive research can exploit what was reported in this *Ph.D. thesis* or published in the related works, to apply these materials to more complexes (*e.g.* photonic/plasmonic coupling) or to different technologies (*e.g.* water splitting or light emitting transistor). The know-how can finally be transferred to other materials (*e.g.* WO_3, MO_2, Al_2O_3, ITO) possibly more suitable for different applications (*e.g.* electrochromic devices, dielectric materials, transparent electrodes).

Chapter 5

Methods

Fabrication

While the details on the fabrication process of the specific thin film for each device and the respective device assembly routine were reported in their corresponding sessions, on this session a general description of the fabrication of the thin films employed in the fabrication of the different type of dye sensitized solar cells is provided.

Thin film fabrication

Titanium dioxide
Titanium dioxide is deposited by pulsed laser deposition on FTO coated soda-lime glass from a solid target of TiO_2 99.999% pure from Kurt. J. Lesker. [70] The vacuum chamber is taken to a vacuum base pressure of 5 x 10^{-3} Pa and then it is filled with pure oxygen to reach the working pressure about three orders of magnitude above the base pressure. The target to sample distance is set to 5 centimetres. The samples are placed in front of the plasma plume and are moved with a linear velocity of 2 cm/s to increase deposition uniformity and to modify the nanostructures formation. In fact, at a given working pressure if the samples are kept steady with respect to the deposition centre, the growth rate will increase and the deposit will result denser. The laser was set-up to operate at a fixed energy of 400 mJ per pulse with a frequency of 20 Hz. Fluency was approximately 2 mJ/cm^2. The thin film thickness was digitally controlled by setting the number of laser pulses. The porosity of the layer to be deposited instead was tuned by changing through a mass flow controller the amount of gas fed into the chamber, with higher gas pressure resulting in a less energetic species and a more porous material. *Viceversa* a lower pressure was letting more energetic cluster to impact on the sample with higher energy forming a denser film. Film growth rate is controlled and changes with the background gas pressure present in the chamber during deposition. Growth rate at different deposition pressures are reported below. All the films were deposited at room temperature and thermally annealed after deposition to reach crystallization. The deposition rate is therefore increasing with pressure. As it is clear from the graph above it trends similarly to the pore volume fraction. This means that in first approximation the

growth rate is controlled by the fraction of voids that are formed upon clusters reorganization during the deposition process.
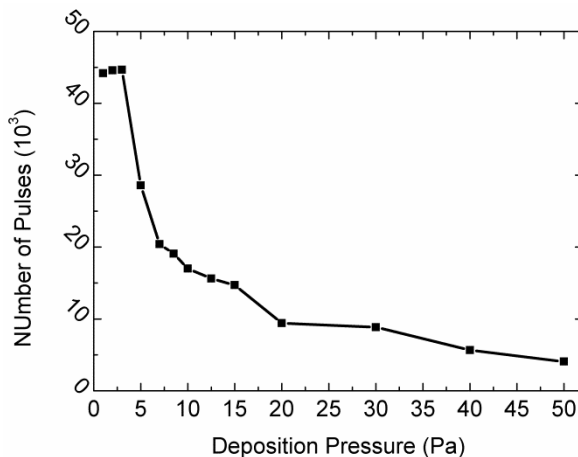
Figure 85 Number of pulses needed to achieve 1 mm thick titanium dioxide film at different background gas pressure in the deposition chamber
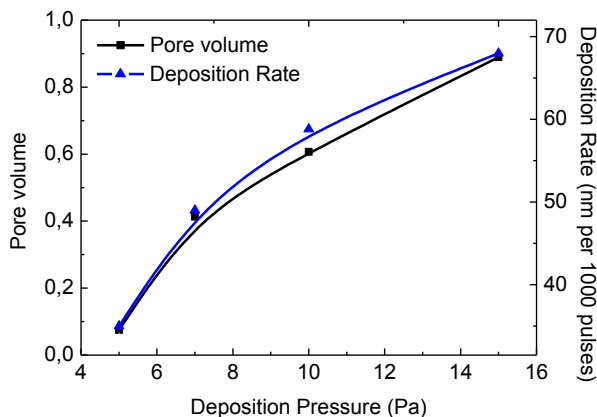
Figure 86 (Black squares) Pore volume and (Blue traingles) deposition rates at different deposition pressures.

Monolithic structure

The monolithic assembly was fabricated by depositing a layer of aluminium trioxide and a layer of indium tin oxide (ITO) on top of a layer of titanium

dioxide deposited as previously described. The aluminium oxide was fabricated by pulsed laser deposition in oxygen from a target of 99.999 % purity Al2O3 from Kurt J. Lesker. It was made porous enough to allow the percolation of the hole transporter redox couple while electrically insulating the top ITO from the TiO2 photoanode. The ITO layer was fabricated by magnetron sputtering in argon at 1 Pa from a target of ITO from Kurt J. Lesker. To restore ITO stoichiometry and to crystallize the TiO_2 photoanode laying underneath, the multi-layered film was thermally treated in air at 500°C.

Photonic crystals

One dimensional photonic crystals are nanostructures comprising a spatial periodic variation in their refractive index with the periodicity being in the scale range of the visible wavelength region. As it was demonstrated [154, 226] the modulation in effective refractive index can be induced by periodically varying the film porosity. Changing vacuum chamber working pressure during the deposition process one can induce the growth of layers with alternating porosity and thus refractive index. While details on these materials will be treated on the next chapter, for more details on the fabrication the reader can refer to Passoni et al. ACS Nano (2014). [154]

Characterization

In this session a review is given on the methods used to characterize the materials and the devices presented in the thesis. Being nanostructured opto-electronic materials for photovoltaic the session will be divided in four major characterization field: morphology, optical, electronic and photovoltaic.

Morphology

Scanning Electron microscopy

High resolution imagining was performed with a field emission scanning electron microscpe *Zeiss Supra 40.* A

Transmission Electron Microscopy (in collaboration with University of Cambridge, Cambridge UK)

Transmission electron microscopy was accomplished with a FEI Tecnai F20-G2 FEGTEM with a 200 kV field emission gun.

Brunauer–Emmett–Teller (BET)

Specific surface area and pore size distribution were determined with the BET method and studying nitrogen adsorption–desorption at a temperature of 77 K. A Micromeritics TriStar 3000 Instrument was used. The porous material was deposited on simple alluminum foil substrate. The substrates with and without the film were weighted on a microbalance in order to measure the weight of the deposited thin films.

Computation of surface ratios

Images from top view have been processed. Firstly, the SEM image (1024 × 768 pixels) is converted in a black and white image, as shown in Figure 87.
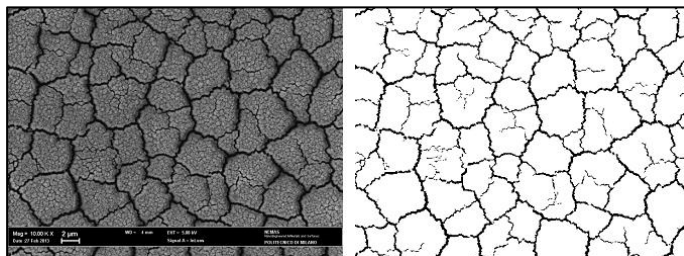
Figure 87 SEM image of a TiO$_2$ nanostructured film (b) The same image converted in black and white

Then, the black and white image is converted in a binary matrix. The island surface to total area ratio is given by dividing the total number of white pixels (elements 1 of the matrix) by the total number of pixels (786432). Moreover, when the surfaces exhibit a well-defined islands with a clear contour, image processing get information also about the island area distribution. As shown in Figure 88, sometimes the conversion to black and white set some pixels black even though they are inside island area. In order to properly include this points in the statistics counting, holes have to be filled, as shown in Figure 89(left). Eventually, islands are labelled, numbered as in Figure 89 (right) and statistically analysed. In order to properly compare all the samples, all SEM images for analysis have been selected at the same scale magnification (5000x)
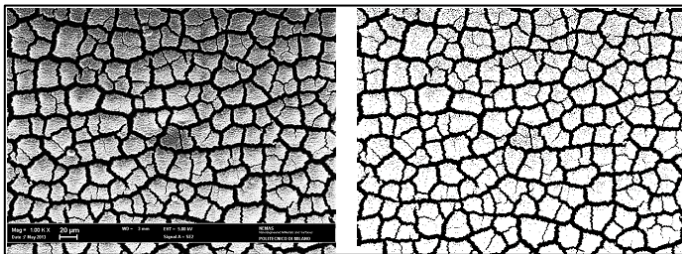
Figure 88 SEM image of a TiO$_2$ nanostructured film with clear island (b) The same image converted in black and white
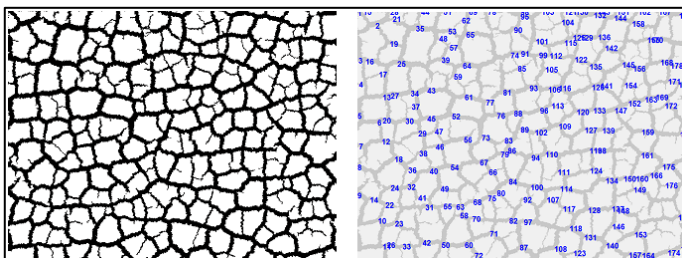
Figure 89 SEM image converted in black and white with holes filled (b)Label islands and numbering

All the calculations have been performed with a custom made code implemented in Matlab® exploiting dedicated functions of Image Analysis Tool Box.

X-ray diffraction spectroscopy

X-ray powder diffraction experiments were carried out on a Bruker D8 Advance diffractometer. It was operated in reflection mode with Ge-monochromated Cu KR1 radiation (λ = 1.5406 Å) and a linear position-sensitive detector, with a 2θ range of 20 to 80° and a step of 0.016°. The full width at half maximum of the diffraction peaks was used to estimate the crystalline size. Scherrer's equation (reported below) was used with shape factor equal to 0.9. [227]

$$\tau = \frac{K\lambda}{\beta cos\theta}$$

Where τ is the mean size of the crystalline domains, K is a dimensionless shape factor, β is the full width half maximum (FWHM) and θ is the angle of the Bragg diffraction.

Roughness Factor by Dye loading and unloading

Roughness factor (RF) is here defined as the ratio between the actual surface area of the nanostructured photoanode and the geometric surface area onto which it was deposited. The value is therefore a pure number and here is sometime presented per micrometre of photoanode thickness. It value was calculated by dye loading/unloading method. With this method the dye molar concentration in the solution used to unload it from the porous samples is estimated with Lambert-Beer's law from the chromatografic measure of its optical density. From the molar concentration, the number of molecules is calculated and, knowing the molecule surface area it is possible to retrieve the overall surface area of the sample available for dye chemisorption. For this purpose, the porous photoanode is dipped for 27 hours in a bath of 0.2 mM N719 dye in acetonitrile and tert-butanol (1:1) for dye molecule chemisorption. After 27 hours the photoanode is rinsed in acetonitrile to remove the excess dye not chemisorbed onto the porous surface. This is done to assume that just a dye monolayer is completely covering the surface. With a known quantity (4 ml) of 0.1 M water solution of NaOH, the dye was desorbed (unloading) from the surface and the optical absorbance of the solution used for desorption is measured.

Atomic force microscopy

The roughness was measured with an Agilent Technologies® Atomic Force Microscopy model 5500. Static tip deflection was used as a feedback signal. *Root Mean Square Roughness* R_{rms} was measured and evaluated as an average of nine measurements carried out on different sample spots.

Raman spectroscopy

A micro Raman confocal microscope (inVia Raman Microscope Renishaw, 50x objective) was used to acquire Raman shift spectra on samples as deposited and after different annealing time and temperatures. The second harmonic of an air-cooled Nd:YAG laser (wavelength = 532 nm) was used as excitation source. Laser power was kept below 0.1 % of the maximum power to avoid

laser annealing. Pure crystalline silicon was used to calibrate the instrument before every measurement. The spectral range subject of the analysis was from 0 to 1800 cm^{-1}. The signal was improved by running 50 acquisitions.

Optical

<u>UV/Vis spectrophotometer</u>
Optical measurements were performed in a UV/vis spectrophometer (SP, Perkin-Elmer Lambda 1050 spectrophotometer Xe lamp). In the assessment of thin film optical characteristics the SP was equipped with an integrating sphere to account for the diffuse light. To measure the transmittance, the samples are placed slightly within the integrated sphere to include the light diffused at high angles but, at the same time, avoiding contributions from the reflectance. The minimum angle ($\theta = 4°$) for considering the transmitted light as diffuse is an intrinsic value given by the geometry of the set-up. It was calculated by considering the aperture diameter ($a = 2.1$ cm) allowing the direct light to exit the integrated sphere and the distance ($d = 15$ cm) of the sample from this aperture.
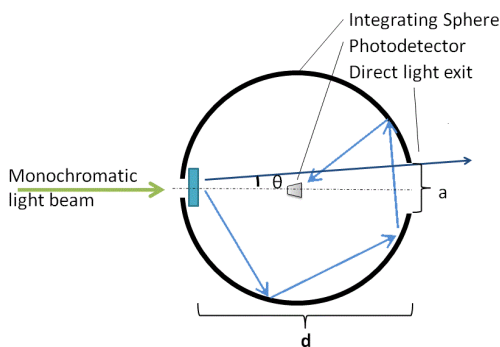
Figure 90 Schematic of the UV/Vis integrating sphere used to measure the optical characteristics of thin films
For chromatographic analysis used for roughness factor calculation a cuvette holder was put in place of the integrating sphere. Quartz cuvettes 1 cm where used.

The transfer matrix method (TMM) is employed to analyse the propagation of an electromagnetic wave trough a stratified medium. At every interface between two layers light is partially transmitted and partially reflected, therefore the total field results in an infinite sum of reflections. This phenomenon creates destructive and constructive interference that are taken into account in the numerical calculation performed by custom software. This takes as input the refractive index of the materials and the structural characteristic of the medium. For porous multilayers these parameters are namely the layers thickness and their effective refractive index (*i.e.* the refractive index of the material, weighted by the refractive index of the material present in the porous fraction). The same software is also used to retrieve information about the material through the input of other information. By measuring, for example at the SEM the thickness of the layers the fitting of the transmission spectrum is giving information about the materials refractive indexes. Despite a certain degree of approximation can be expected, this methods gives the possibly to relate the porosity of the material with its effective refractive index. It can therefore be used both as a method to engineer an optical device and as a method to retrieve information about the structure and optics of the materials.

Electronic

Photocurrent and photovoltage transient decay
For the transient photovoltage/photocurrent decay measurements, a white light bias was generated from an array of diodes. Red light pulse diodes (square pulse width, 100 nanosecond rise and fall time) controlled by a fast solid state switch were used as the perturbation source. The voltage dynamics were recorded on a PC interfaced Keithley 2602 source meter with a 500 µs response time. The light source used for the perturbation was set to a low level so to assume the system to be linear. The electron recombination lifetime could be measured over a range of applied biases by varying the white light bias intensity. A charge extraction routine was performed before switching to the next light intensity to measure the electron density in the film. In the charge extraction, the illumination source was turned off in less than 1 µs, while

simultaneously, the cell was short circuited. The current, while the device is returning to $V = 0$ and $J = 0$, is integrated to estimate the excess charge in the film at that V_{OC}.

Intensity modulated photo-spectroscopy

Autolab FRA32M frequency analyzer was connected to an LED driver kit which powered a 530 nm high-power LED for intensity modulated photocurrent spectroscopy (IMPS) and intensity modulated photovoltage spectroscopy (IMVS). A 10% modulation in light intensity was applied for a frequency range of 0.1Hz to 10^6 Hz. A calibrated Si-photodiode (THORLABS) was used to calibrate the light intensity that was in fact varied between 0.57 and 22.34 mW/cm^2. The charge transport time (τ_d) and the charge recombination time (τ_{rec}) of photogenerated charges were obtained from the frequency minimum in the Nyquist plot of IMVS and IMPS spectra by setting τ_d and τ_{rec} equal to the inverse of 2π times the minimum frequency measured by IMPS and IMVS measurements respectively. NOVA 1.11 software was used for data acquisition and analysys.

Electrochemical impedance spectroscopy

In the case of monolithic DSSC electrochemical impedance spectroscopy (EIS) was performed with a potentiostat/galvanostat (AUTOLAB, PGSTAT 302N) and a frequency analayzer (AUTOLAB, FRA32M). EIS was performed in dark condition and under illumination (AM 1.5 spectrum) in the range of frequency from 1 to 10^5 Hz with 20 mV$_{rms}$ AC amplitude. Superimposed DC voltage was set at the maximum power point of the devices, namely 0.48 V as derived from experimental current-voltage curve. All the impedance spectra were fitted using appropriate equivalent circuit model[228] built in NOVA 1.11 software as reported below. The time constants of the charge transfer (τd) and recombination (τrec) phenomena were estimated using the calculated resistive and capacitive components of the equivalent circuit reported above. The diffusion length (L), were obtained as it follows, according to the literature by Halme *et.al.* [228]
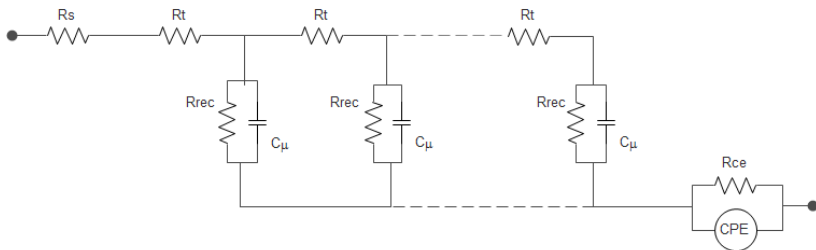
Figure 91 Equivalent circuit model used to fit the EIS spectra acquired for monolithic dye sensitized solar cells

$$\tau_d = R_t C_\mu \tag{1}$$

$$\tau_{rec} = R_{rec} C_\mu \tag{2}$$

$$D = \frac{d^2}{\tau_d} \tag{3}$$

$$L = \sqrt{D \, \tau_{rec}} \tag{4}$$

Hall-effect measurements

In the monolithic dye sensitized solar cells the indium tin oxide (ITO) electrical properties namely resistivity, carrier densities and Hall mobility were studied with a Hall effect analyzer (Microworld, HMS5300). The measurements were performed with a four-probe Van der Pauw method. A mean magnetic field intensity of 0.56 T and a probing current of 1 mA were used. The contacts were fabricated by thermal evaporating on the edges of each sample a thin film of silver that helped removing stray contact resistance between the ITO thin film and the instrument gold probes.

Photovoltaic

Solar simulator

For photovoltaic performance assessments of solid state, monolithic and photonic crystals dye sensitized solar cells a Newport Sun Simulator (Oriel Sol3A Class AAA) was used. The solar spectrum AM 1.5 was used to measure the current density curve. Photovoltaic performance, namely, open circuit voltage, short circuit current, fill factor and power conversion efficiency were retrieved from this measurement. The solar simulator have been previously calibrated in intensity with a NREL certified Oriel Si reference cell. For the spectral measurement, a 45W quartz-tungsten-halogen lamp from Newport was used to account for attenuation in the measurement system (at 1 sun the mismatch factor was found to be 0.994). The active surface area of solid state, monolithic and photonic crystals dye sensitized solar cells was limited by applying a black physical mask

Liquid state dye sensitized solar cells current voltage curves were acquired in collaboration with *Ecole Politechnique Federele de Lausanne* in Switzerland at the Laboratory of Photonics and Interfaces with solar simulator comprising a 450 W xenon lamp (Oriel, USA) light source. A Schott K113 Tempax sunlight filter (Präzisions Glas & Optik GmbH, Germany) was employed to reduce the simulated and actual solar spectrum the mismatch to less than 2%. For data acquisition a Keithley model 2400 digital source meter (Keithley, USA) was used. The photoactive area of was limited to 0.16 cm^2 by placing a black mask of 4×4 mm^2

External quantum Efficiency

The external quantum efficiency of solid state, monolithic and photonic crystals dye sensitized solar cells was measured with a Newport setup operating in dc mode without bias and in a dark environment.

Liquid state dye sensitized solar cells were measured with a monochromatic light of a Gemini-180 double monochromator Jobin Yvon Ltd. (UK), powered by a 300 W xenon light source (ILC Technology, USA) superimposed on a 10 mW cm^{-2} LED light. The monochromatic incident light was passed through a chopper running at 1.8 Hz frequency.

REFERENCE

1.   Richard, F. There's plenty of space at the bottom. *Conference paper, Calthec University* (1959).
2.   Freestone, I., Meeks, N., Sax, M. & Higgitt, C. The Lycurgus Cup - A Roman nanotechnology. *Gold Bulletin* **40**, 270-277 (2007).
3.   Kochmann, W. et al. Nanowires in ancient Damascus steel. *Journal of Alloys and Compounds* **372**, L15-L19 (2004).
4.   Salvador, A., Pascual-Martí, M.C., Adell, J.R., Requeni, A. & March, J.G. Analytical methodologies for atomic spectrometric determination of metallic oxides in UV sunscreen creams. *Journal of Pharmaceutical and Biomedical Analysis* **22**, 301-306 (2000).
5.   Pfaff, G. & Reynders, P. Angle-Dependent Optical Effects Deriving from Submicron Structures of Films and Pigments. *Chemical Reviews* **99**, 1963-1982 (1999).
6.   Braun, J.H., Baidins, A. & Marganski, R.E. TiO2 pigment technology: a review. *Progress in Organic Coatings* **20**, 105-138 (1992).
7.   Diebold, U. The surface science of titanium dioxide. *Surface Science Reports* **48**, 53-229 (2003).
8.   Fujishima, A. & Honda, K. Electrochemical Photolysis of Water at a Semiconductor Electrode. *Nature* **238**, 37-38 (1972).
9.   Gholipour, M.R., Dinh, C.T., Beland, F. & Do, T.O. Nanocomposite heterojunctions as sunlight-driven photocatalysts for hydrogen production from water splitting. *Nanoscale* **7**, 8187-8208 (2015).
10.   Chawla, P. & Tripathi, M. Novel improvements in the sensitizers of dye-sensitized solar cells for enhancement in efficiencya review. *International Journal of Energy Research* **39**, 1579-1596 (2015).
11.   Bavykin, D.V., Friedrich, J.M. & Walsh, F.C. Protonated titanates and TiO2 nanostructured materials: Synthesis, properties, and applications. *Advanced Materials* **18**, 2807-2824 (2006).
12.   Bai, Y., Mora-Sero, I., De Angelis, F., Bisquert, J. & Wang, P. Titanium Dioxide Nanomaterials for Photovoltaic Applications. *Chemical Reviews* **114**, 10095-10130 (2014).
13.   Bai, J. & Zhou, B.X. Titanium Dioxide Nanomaterials for Sensor Applications. *Chemical Reviews* **114**, 10131-10176 (2014).
14.   Qu, X.L., Brame, J., Li, Q.L. & Alvarez, P.J.J. Nanotechnology for a Safe and Sustainable Water Supply: Enabling Integrated Water Treatment and Reuse. *Accounts of Chemical Research* **46**, 834-843 (2013).

15. Chen, X. & Mao, S.S. Titanium dioxide nanomaterials: Synthesis, properties, modifications, and applications. *Chemical Reviews* **107**, 2891-2959 (2007).

16. Yang, S. et al. Crystal shape engineering of anatase TiO2 and its biomedical applications. *CrystEngComm* **17**, 6617-6631 (2015).

17. Pan, J., Liu, G., Lu, G.Q. & Cheng, H.-M. On the True Photoreactivity Order of {001}, {010}, and {101} Facets of Anatase TiO2 Crystals. *Angewandte Chemie International Edition* **50**, 2133-2137 (2011).

18. Shiu, J.W. et al. Size-Controlled Anatase Titania Single Crystals with Octahedron-like Morphology for Dye-Sensitized Solar Cells. *ACS Nano* **6**, 10862-10873 (2012).

19. Buonsanti, R. et al. Hyperbranched Anatase TiO2 Nanocrystals: Nonaqueous Synthesis, Growth Mechanism, and Exploitation in Dye-Sensitized Solar Cells. *Journal of the American Chemical Society* **133**, 19216-19239 (2011).

20. Carp, O., Huisman, C.L. & Reller, A. Photoinduced reactivity of titanium dioxide. *Progress in Solid State Chemistry* **32**, 33-177 (2004).

21. van de Lagemaat, J., Benkstein, K.D. & Frank, A.J. Relation between Particle Coordination Number and Porosity in Nanoparticle Films: Implications to Dye-Sensitized Solar Cells. *The Journal of Physical Chemistry B* **105**, 12433-12436 (2001).

22. Seyed-Razavi, A., Snook, I.K. & Barnard, A.S. Origin of nanomorphology: does a complete theory of nanoparticle evolution exist? *Journal of Materials Chemistry* **20**, 416-421 (2010).

23. Scanlon, D.O. et al. Band alignment of rutile and anatase TiO2. *Nature Materials* **12**, 798-801 (2013).

24. Ravindra, N.M., Ganapathy, P. & Choi, J. Energy gap–refractive index relations in semiconductors – An overview. *Infrared Physics & Technology* **50**, 21-29 (2007).

25. Moss, T.S. Photoconductivity in the Elements. *Proceedings of the Physical Society. Section A* **64**, 590 (1951).

26. Gopal, V. Energy gap-refractive index interrelation. *Infrared Physics* **22**, 255-257 (1982).

27. Mosaddeq-ur-Rahman, M. et al. Refractive index and degree of inhomogeneity of nanocrystalline TiO2 thin films: Effects of substrate and annealing temperature. *Journal of Applied Physics* **88**, 4634-4641 (2000).

28. Jellison, G.E., Boatner, L.A., Budai, J.D., Jeong, B.-S. & Norton, D.P. Spectroscopic ellipsometry of thin film and bulk anatase (TiO2). *Journal of Applied Physics* **93**, 9537-9541 (2003).

29. Park, N.G., van de Lagemaat, J. & Frank, A.J. Comparison of dye-sensitized rutile- and anatase-based TiO2 solar cells. *Journal of Physical Chemistry B* **104**, 8989-8994 (2000).

30. Benkstein, K.D., Kopidakis, N., van de Lagemaat, J. & Frank, A.J. Influence of the Percolation Network Geometry on Electron Transport in Dye-Sensitized Titanium Dioxide Solar Cells. *The Journal of Physical Chemistry B* **107**, 7759-7767 (2003).

31. Kopidakis, N., Benkstein, K.D., van de Lagemaat, J. & Frank, A.J. Transport-Limited Recombination of Photocarriers in Dye-Sensitized Nanocrystalline TiO2 Solar Cells. *The Journal of Physical Chemistry B* **107**, 11307-11315 (2003).

32. Zhang, Q. & Cao, G. Nanostructured photoelectrodes for dye-sensitized solar cells. *Nano Today* **6**, 91-109 (2011).

33. Wang, J. & Lin, Z. Dye-Sensitized TiO2 Nanotube Solar Cells: Rational Structural and Surface Engineering on TiO2 Nanotubes. *Chemistry – An Asian Journal* **7**, 2754-2762 (2012).

34. Kim, D., Ghicov, A., Albu, S.P. & Schmuki, a.P. Bamboo-Type TiO2 Nanotubes: Improved Conversion Efficiency in Dye-Sensitized Solar Cells. *Journal of American Chem Soc*, 16454–16455 (2008).

35. Galstyan, V. et al. Vertically Aligned TiO2 Nanotubes on Plastic Substrates for Flexible Solar Cells. *Small* **7**, 2437-2442 (2011).

36. Vomiero, A. et al. Flexible dye sensitized solar cells using TiO2 nanotubes. *Energy & Environmental Science* **4**, 3408-3413 (2011).

37. Law, M., Greene, L.E., Johnson, J.C. & Yang, R.s.a.P. Nanowire dye-sensitized solar cells. *Nature Materials* **4**, 455-459 (2005).

38. Frank, A.J., Kopidakis, N. & Lagemaat, J.v.d. Electrons in nanostructured TiO2 solar cells: transport, recombination and photovoltaic properties. *Coordination Chemistry Reviews*, 1165–1179 (2004).

39. Feng, X. et al. Vertically Aligned Single Crystal TiO2 Nanowire Arrays Grown Directly on Transparent Conducting Oxide Coated Glass: Synthesis Details and Applications. *Nano Letters* **8**, 3781-3786 (2008).

40. Tétreault, N. et al. High-Efficiency Solid-State Dye-Sensitized Solar Cells: Fast Charge Extraction through Self-Assembled 3D Fibrous Network of Crystalline TiO2 Nanowires. *American Chemical Society Nano* **4**, 7644-7650 (2010).

41. Shalan, A.E., Rashad, M.M., Yu, Y., Lira-Cantú, M. & Abdel-Mottaleb, M.S.A. A facile low temperature synthesis of TiO2 nanorods for high efficiency dye sensitized solar cells. *Applied Physics A* **110**, 111-122 (2013).

42. Sauvage, F. et al. Hierarchical TiO2 Photoanode for Dye-Sensitized Solar Cells. *Nanoletters*, 2562-2567 (2010).

43. Di Fonzo, F. et al. Growth regimes in pulsed laser deposition of aluminum oxide films. *Applied Physics A: Materials Science & Processing* **93**, 765-769 (2008).

44. Ghosh, R. et al. Nanoforest Nb2O5 Photoanodes for Dye-Sensitized Solar Cells by Pulsed Laser Deposition. *Applied Material & Interfaces*, 3929-3935 (2011).

45. Ko, S.H. et al. Nanoforest of Hydrothermally Grown Hierarchical ZnO Nanowires for a High Efficiency Dye-Sensitized Solar Cell. *Nanoletters*, 666–671 (2011).

46. Wu, C.-H.K.a.J.-J. Chemical bath deposition of ZnO nanowire–nanoparticle composite electrodes for use in dye-sensitized solar cells. *Nanotechnology* (2007).

47. Yodyingyong, S. et al. ZnO nanoparticles and nanowire array hybrid photoanodes for dye-sensitized solar cells. *Applied Physics Letters* (2010).

48. Chen, S.G., Chappel, S., Diamant, Y. & Zaban, A. Preparation of Nb2O5 Coated TiO2 Nanoporous Electrodes and Their Application in Dye-Sensitized Solar Cells. *Chem. Mater*, 4629-4634 (2001).

49. Diamant, Y., Chappel, S., Chen, S.G., Melamed, O. & Zaban, A. Core–shell nanoporous electrode for dye sensitized solar cells: the effect of shell characteristics on the electronic properties of the electrode. *Coordination Chemistry Reviews*, 1271–1276 (2004).

50. Linic, S., Christopher, P. & Ingram, D.B. Plasmonic-metal nanostructures for efficient conversion of solar to chemical energy. *Nature Materials* **10**, 911-922 (2011).

51. Jeong, N.C., Prasittichai, C. & Hupp, a.J.T. Photocurrent Enhancement by Surface Plasmon Resonance of Silver Nanoparticles in Highly Porous Dye-Sensitized Solar Cells. *Langmuir* **27**, 14609–14614 (2011).

52. Qi, J., Dang, X., Hammond, P.T. & Belcher, A.M. Highly Efficient Plasmon-Enhanced Dye-Sensitized Solar Cells through Metal@Oxide Core ShellNanostructure. *ACSNano* **5**, 7108–7116 (2011).

53. Willmott, P.R. & Huber, J.R. Pulsed laser vaporization and deposition. *Reviews of Modern Physics* **72**, 315-328 (2000).

54. Boyd, I. in Laser in der Technik / Laser in Engineering (ed. Waidelich, W.) 349-359 (Springer Berlin Heidelberg, 1994).

55. Zheng, J.P., Huang, Z.Q., Shaw, D.T. & Kwok, H.S. GENERATION OF HIGH-ENERGY ATOMIC-BEAMS IN LASER-SUPERCONDUCTING TARGET INTERACTIONS. *Applied Physics Letters* **54**, 280-282 (1989).

56. Venkatesan, T., Wu, X., Inam, A. & Wachtman, J. Observation of two distinct components during pulsed laser deposition of high Tc superconducting films. *Applied Physics Letters* **52**, 1193-1195 (1988).

57. Dave, H.A.B., Matthijn, D. & Guus, R. Pulsed laser deposition in Twente: from research tool towards industrial deposition. *Journal of Physics D: Applied Physics* **47**, 034006 (2014).

58. Boyd, I.W. et al. Beam Processing and Laser ChemistryGeometric optimisation for the deposition of high temperature superconductors. *Applied Surface Science* **43**, 382-386 (1989).

59. Marine, W., Peray, M., Mathey, Y. & Pailharey, D. Deposition of Y-Ba-Cu oxide superconducting thin films by Nd:YAG laser evaporation. *Applied Surface Science* **43**, 377-381 (1989).

60. Di Fonzo, F. et al. Growth regimes in pulsed laser deposition of aluminum oxide films. *Applied Physics A: Materials Science & Processing* **93**, 765-769 (2008).

61. Fonzo, F.D. et al. Hierarchically organized nanostructured TiO_2 for photocatalysis applications. *Nanotechnology* **20**, 015604 (2009).

62. Sauvage, F. et al. Hierarchical TiO2 Photoanode for Dye-Sensitized Solar Cells. *Nano Letters* **10**, 2562-2567 (2010).

63. Gonzalez-Garcia, L., Gonzalez-Valls, I., Lira-Cantu, M., Barranco, A. & Gonzalez-Elipe, A.R. Aligned TiO2 nanocolumnar layers prepared by PVD-GLAD for transparent dye sensitized solar cells. *Energy & Environmental Science* **4**, 3426-3435 (2011).

64. Li, K.-l., Xie, Z.-b. & Adams, S. A reliable TiO2 nanotube membrane transfer method and its application in photovoltaic devices. *Electrochimica Acta* **62**, 116-123 (2012).

65. Noh, J.H. et al. Aligned Photoelectrodes with Large Surface Area Prepared by Pulsed Laser Deposition. *The Journal of Physical Chemistry C* **116**, 8102-8110 (2012).

66. Ghosh, R. et al. Increasing Photocurrents in Dye Sensitized Solar Cells with Tantalum-Doped Titanium Oxide Photoanodes Obtained by Laser Ablation. *ACS APPLIED MATERIALS & INTERFACES* **4**, 4566-4570 (2012).

67. Shirolkar, M.M. et al. Relation between crystallinity and chemical nature of surface on wettability: A study on pulsed laser deposited TiO[sub 2] thin films. *Journal of Applied Physics* **109**, 123512-10 (2011).

68. Syarif, D.G. et al. Preparation of anatase and rutile thin films by controlling oxygen partial pressure. *Applied Surface Science* **193**, 287-292 (2002).

69.   Tetreault, N. & Gratzel, M. Novel nanostructures for next generation dye-sensitized solar cells. *Energy & Environmental Science* **5**, 8506-8516 (2012).

70.   Passoni, L. et al. Hyperbranched Quasi-1D Nanostructures for Solid-State Dye-Sensitized Solar Cells. *ACS Nano* (2013).

71.   Bailini, A., Ossi, P.M. & Rivolta, A. Plume propagation through a buffer gas and cluster size prediction. *Applied Surface Science* **253**, 7682-7685 (2007).

72.   Czanderna, A.W., Rao, C.N.R. & Honig, J.M. The anatase-rutile transition. Part 1.-Kinetics of the transformation of pure anatase. *Transactions of the Faraday Society* **54**, 1069-1073 (1958).

73.   Fusi, M. et al. Island Organization of TiO2 Hierarchical Nanostructures Induced by Surface Wetting and Drying. *Langmuir* **27**, 1935-1941 (2011).

74.   Passoni, L. et al. Multiscale Effect of Hierarchical Self-Assembled Nanostructures on Superhydrophobic Surface. *Langmuir* **30**, 13581-13587 (2014).

75.   Jalava, J.-P. et al. Modeling TiO2's refractive index function from bulk to nanoparticles. *Journal of Quantitative Spectroscopy and Radiative Transfer* **167**, 105-118 (2015).

76.   Adhikari, D.C., Yanying. Energy Consumption and Economic Growth: A Panel Cointegration Analysis for Developing Countries. *Review of Economics Finance* (2013).

77.   Jaunky, V.C. The CO2 emissions-income nexus: Evidence from rich countries. *Energy Policy* **39**, 1228-1240 (2011).

78.   Acaravci, A. & Ozturk, I. On the relationship between energy consumption, CO2 emissions and economic growth in Europe. *Energy* **35**, 5412-5420 (2010).

79.   Wang, K.-M. The relationship between carbon dioxide emissions and economic growth: quantile panel-type analysis. *Quality & Quantity* **47**, 1337-1366 (2013).

80.   Felt, U. & Wynne, B. Taking European knowledge society seriously. *Luxembourg: DG for Research. EUR* **22**, 700 (2007).

81.   Höök, M. & Tang, X. Depletion of fossil fuels and anthropogenic climate change—A review. *Energy Policy* **52**, 797-809 (2013).

82.   O'Regan, B. & Gratzel, M. A low-cost, high-efficiency solar cell based on dye-sensitized colloidal TiO2 films. *Nature* **353**, 737-740 (1991).

83.   Mathew, S. et al. Dye-sensitized solar cells with 13% efficiency achieved through the molecular engineering of porphyrin sensitizers. *Nat Chem* **6**, 242-247 (2014).

84. Pettersson, H. et al. Parallel-connected monolithic dye-sensitised solar modules. *Progress in Photovoltaics* **18**, 340-345 (2010).

85. London, I.A. (2013).

86. Li, L.-L. & Diau, E.W.-G. Porphyrin-sensitized solar cells. *Chemical Society Reviews* **42**, 291-304 (2013).

87. Hwang, S. et al. A highly efficient organic sensitizer for dye-sensitized solar cells. *Chemical Communications*, 4887-4889 (2007).

88. Liang, W.Y. Excitons. *Physics Education* **5**, 226 (1970).

89. Kim, B.-G., Zhen, C.-G., Jeong, E.J., Kieffer, J. & Kim, J. Organic Dye Design Tools for Efficient Photocurrent Generation in Dye-Sensitized Solar Cells: Exciton Binding Energy and Electron Acceptors. *Advanced Functional Materials* **22**, 1606-1612 (2012).

90. Docampo, P., Guldin, S., Steiner, U. & Snaith, H.J. Charge Transport Limitations in Self-Assembled TiO2 Photoanodes for Dye-Sensitized Solar Cells. *The Journal of Physical Chemistry Letters*, 698-703 (2013).

91. Wang, X. et al. Transient photocurrent and photovoltage studies on charge transport in dye sensitized solar cells made from the composites of TiO[sub 2] nanofibers and nanoparticles. *Applied Physics Letters* **98**, 082114-3 (2011).

92. Haque, S.A. et al. Charge Separation versus Recombination in Dye-Sensitized Nanocrystalline Solar Cells: the Minimization of Kinetic Redundancy. *Journal of the American Chemical Society* **127**, 3456-3462 (2005).

93. Wang, M., Chen, P., Humphry-Baker, R., Zakeeruddin, S.M. & Grätzel, M. The Influence of Charge Transport and Recombination on the Performance of Dye-Sensitized Solar Cells. *ChemPhysChem* **10**, 290-299 (2009).

94. Boschloo, G. & Hagfeldt, A. Characteristics of the Iodide/Triiodide Redox Mediator in Dye-Sensitized Solar Cells. *Accounts of Chemical Research* **42**, 1819-1826 (2009).

95. Prezhdo, O.V., Duncan, W.R. & Prezhdo, V.V. Dynamics of the Photoexcited Electron at the Chromophore–Semiconductor Interface. *Accounts of Chemical Research* **41**, 339-348 (2008).

96. Passoni, L., Giordano, F., Zakeeruddin, S.M., Gratzel, M. & Di Fonzo, F. Hyperbranched self-assembled photoanode for high efficiency dye-sensitized solar cells. *RSC Advances* **5**, 93180-93186 (2015).

97. T, Y., T, S. & O, I. Polymer-electrolyte-based photoelectrochemical solar energy conversion with poly(3-methylthiophene) photoactive electrode. *Synthetic Metals* **82**, 215-220 (1996).

98.   Yella, A. et al. Porphyrin-Sensitized Solar Cells with Cobalt (II/III)-Based Redox Electrolyte Exceed 12 Percent Efficiency. *Science* **334**, 629-634 (2011).

99.   Feng, W., Umeda, T., Fujii, A. & Yoshino, X.W.a.K. Enhancement of Photoresponse by Enlarging the Effective Interface between Conducting Polymer and Titanium Oxide in Photovoltaic Device. *Japanese Journal of Applied Physics* **43**, 3473-3478 (2004).

100. Ding, I.-K. et al. Pore-Filling of Spiro-OMeTAD in Solid-State Dye Sensitized Solar Cells: Quantification, Mechanism, and Consequences for Device Performance. *Advanced Functional Material* **19**, 2431–2436 (2009).

101. Melas-Kyriazi, J. et al. The Effect of Hole Transport Material Pore Filling on Photovoltaic Performance in Solid-State Dye-Sensitized Solar Cells. *Advanced Functional Material* **1**, 407–414 (2011).

102. Schmidt-Mende, L. & Gratzel, M. TiO2 pore-filling and its effect on the efficiency of solid-state dye-sensitized solar cells. *Thin Solid Films* **500**, 296 – 301 (2006).

103. Docampo, P. et al. Pore Filling of Spiro-OMeTAD in Solid-State Dye-Sensitized Solar Cells Determined Via Optical Reflectometry. *Advanced Functional Materials* **22**, 5010-5019 (2012).

104. Chung, I., Lee, B., He, J., Chang, R.P.H. & Kanatzidis, M.G. All-solid-state dye-sensitized solar cells with high efficiency. *Nature* **485**, 486-489 (2012).

105. Bach, U. et al. Solid-state dye-sensitized mesoporous TiO2 solar cells with high photon-to-electron conversion efficiencies. *Nature* **395**, 583-585 (1998).

106. In, C., Byunghong, L., Jiaqing, H., Robert, P.H.C. & Mercouri, G.K. All-solid-state dye-sensitized solar cells with high efficiency. *Nature* **485**, 486-489 (2012).

107. Bouclé, J. & Ackermann, J. Solid-state dye-sensitized and bulk heterojunction solar cells using TiO_2 and ZnO nanostructures: recent progress and new concepts at the borderline. *Polymer International* **61**, 355-373 (2012).

108. Cai, N. et al. An Organic D-π-A Dye for Record Efficiency Solid-State Sensitized Heterojunction Solar Cells. *Nano Letters* **11**, 1452-1456 (2011).

109. Snaith, H.J. et al. High Extinction Coefficient "Antenna" Dye in Solid-State Dye-Sensitized Solar Cells: A Photophysical and Electronic Study. *The Journal of Physical Chemistry C* **112**, 7562-7566 (2008).

110. Park, N.-G. Light management in dye-sensitized solar cell. *Korean Journal of Chemical Engineering* **27**, 375-384 (2010).

111. Ito, S. et al. High-Efficiency Organic-Dye- Sensitized Solar Cells Controlled by Nanocrystalline-TiO2 Electrode Thickness. *Advanced Materials* **18**, 1202-1205 (2006).

112. Kim, D.H. et al. Stable anatase TiO2 coating on quartz fibers by atomic layer deposition for photoactive light-scattering in dye-sensitized solar cells. *Nanoscale* **4**, 4731-4738 (2012).

113. Tu, W.-K., Lin, C.-J., Chatterjee, A., Shiau, G.-H. & Chien, S.-H. A novel nanocomposite TiO2 photoanode for highly efficient dye-sensitized solar cells. *Journal of Power Sources* **203**, 297-301 (2012).

114. Zheng, Q. et al. Hierarchical Construction of Self-Standing Anodized Titania Nanotube Arrays and Nanoparticles for Efficient and Cost-Effective Front-Illuminated Dye-Sensitized Solar Cells. *ACS Nano* **5**, 5088-5093 (2011).

115. Koo, H.J. et al. Nano-embossed Hollow Spherical TiO2 as Bifunctional Material for High-Efficiency Dye-Sensitized Solar Cells. *Advanced Materials* **20**, 195-199 (2008).

116. Kang, S.H. et al. Influence of light scattering particles in the TiO2 photoelectrode for solid-state dye-sensitized solar cell. *Journal of Photochemistry and Photobiology A: Chemistry* **200**, 294-300 (2008).

117. Kang, S.H. et al. Nanorod-Based Dye-Sensitized Solar Cells with Improved Charge Collection Efficiency. *Advanced Materials* **20**, 54-58 (2008).

118. Matt, L., Lori, E.G., Justin, C.J., Richard, S. & Peidong, Y. Nanowire dye-sensitized solar cells. *Nature Materials* **4**, 455-459 (2005).

119. Haase, C. & Stiebig, H. Optical properties of thin-film silicon solar cells with grating couplers. *Progress in Photovoltaics: Research and Applications* **14**, 629-641 (2006).

120. Abrusci, A. et al. Influence of Ion Induced Local Coulomb Field and Polarity on Charge Generation and Efficiency in Poly(3-Hexylthiophene)-Based Solid-State Dye-Sensitized Solar Cells. *Advanced Functional Materials* **21**, 2571-2579 (2011).

121. Jiang, C.Y. et al. Low temperature processing solid-state dye sensitized solar cells. *Applied Physics Letters* **100**, 113901-4 (2012).

122. Crossland, E.J.W. et al. Mesoporous TiO2 single crystals delivering enhanced mobility and optoelectronic device performance. *Nature* **495**, 215-219 (2013).

123. Zhang, K. et al. High-Performance, Transparent, Dye-Sensitized Solar Cells for See-Through Photovoltaic Windows. *Advanced Energy Materials* **4**, 1301966 (2014).

124. Goncalves, L.M., de Zea Bermudez, V., Ribeiro, H.A. & Mendes, A.M. Dye-sensitized solar cells: A safe bet for the future. *Energy & Environmental Science* **1**, 655 (2008).

125. Barber, G.D. et al. Utilization of Direct and Diffuse Sunlight in a Dye-Sensitized Solar Cell - Silicon Photovoltaic Hybrid Concentrator System. *The Journal of Physical Chemistry Letters* **2**, 581 (2011).

126. Kim, J.H., Moon, K.J., Kim, J.M., Lee, D. & Kim, S.H. Effects of various light-intensity and temperature environments on the photovoltaic performance of dye-sensitized solar cells. *Solar Energy* **113**, 251 (2015).

127. Hagfeldt, A., Boschloo, G., Sun, L., Kloo, L. & Pettersson, H. Dye-Sensitized Solar Cells. *Chemical Reviews* **110**, 6595 (2010).

128. Mathew, S. et al. Dye-sensitized solar cells with 13% efficiency achieved through the molecular engineering of porphyrin sensitizers. *Nat Chem* **6**, 242 (2014).

129. Thompson, S.J., Duffy, N.W., Bach, U. & Cheng, Y.-B. On the Role of the Spacer Layer in Monolithic Dye-Sensitized Solar Cells. *The Journal of Physical Chemistry C* **114**, 2365-2369 (2010).

130. Parisi, M.L., Maranghi, S. & Basosi, R. The evolution of the dye sensitized solar cells from Grätzel prototype to up-scaled solar applications: A life cycle assessment approach. *Renewable and Sustainable Energy Reviews* **39**, 124-138 (2014).

131. Parisi, M.L., Maranghi, S. & Basosi, R. The evolution of the dye sensitized solar cells from Graetzel prototype to up-scaled solar applications: A life cycle assessment approach. *Renewable and Sustainable Energy Reviews* **39**, 124 (2014).

132. Kay, A. & Grätzel, M. Low cost photovoltaic modules based on dye sensitized nanocrystalline titanium dioxide and carbon powder. *Solar Energy Materials and Solar Cells* **44**, 99-117 (1996).

133. Pettersson, H. et al. Parallel-connected monolithic dye-sensitised solar modules. *Progress in Photovoltaics: Research and Applications* **18**, 340-345 (2010).

134. Pettersson, H. et al. The monolithic multicell: a tool for testing material components in dye-sensitized solar cells. *Progress in Photovoltaics: Research and Applications* **15**, 113-121 (2007).

135. Pettersson, H., Gruszecki, T., Johansson, L.-H. & Johander, P. Manufacturing method for monolithic dye-sensitised solar cells

permitting long-term stable low-power modules. *Solar Energy Materials and Solar Cells* **77**, 405-413 (2003).

136. Han, H., Bach, U., Cheng, Y.-B. & Caruso, R.A. Increased nanopore filling: Effect on monolithic all-solid-state dye-sensitized solar cells. *Applied Physics Letters* **90**, 213510 (2007).

137. Chiang, Y.-F., Tsai, C.-H., Chen, P. & Guo, T.-F. Bifacial transparent solid-state dye-sensitized solar cell with sputtered indium-tin-oxide counter electrode. *Solar Energy* **86**, 1967-1972 (2012).

138. Yang, Y. et al. Fully printable transparent monolithic solid-state dye-sensitized solar cell with mesoscopic indium tin oxide counter electrode. *Physical Chemistry Chemical Physics* **16**, 17743-17747 (2014).

139. Chiang, Y.F., Tsai, C.H., Chen, P. & Guo, T.F. Bifacial transparent solid-state dye-sensitized solar cell with sputtered indium-tin-oxide counter electrode. *Solar Energy* **86**, 1967 (2012).

140. Docampo, P. et al. Lessons Learned: From Dye-Sensitized Solar Cells to All-Solid-State Hybrid Devices. *Advanced Materials* **26**, 4013 (2014).

141. Ghadirzadeh, A. et al. Hyperbranched Quasi-1D TiO2 Nanostructure for Hybrid Organic - Inorganic Solar Cells. *ACS Applied Materials & Interfaces* **7**, 7451 (2015).

142. Passoni, L. et al. Hyperbranched Quasi-1D Nanostructures for Solid-State Dye-Sensitized Solar Cells. *ACS Nano* **7**, 10023-10031 (2013).

143. Di Fonzo, F. et al. Growth regimes in pulsed laser deposition of aluminum oxide films. *Applied Physics A* **93**, 765-769 (2008).

144. Kelly, P.J. & Arnell, R.D. Magnetron sputtering: a review of recent developments and applications. *Vacuum* **56**, 159 (2000).

145. Delmdahl, R. & Rainer, P. Excimer laser technology trends. *Journal of Physics D: Applied Physics* **47**, 034004 (2014).

146. Kuzanyan, A.S., Petrosyan, V.A., Pilosyan, S.K. & Nesterov, V.M. Laser deposition of large-area thin films. *Quantum Electronics* **41**, 253 (2011).

147. Blank, D., Dekkers, M. & Rijnders, G. Pulsed laser deposition in Twente: from research tool towards industrial deposition. *Journal of Physics D: Applied Physics* **47**, 034006 (2014).

148. Fumagalli, F., Martì-Rujas, J. & Di Fonzo, F. Room temperature deposition of high figure of merit Al-doped zinc oxide by pulsed-direct current magnetron sputtering: Influence of energetic negative ion bombardment on film's optoelectronic properties. *Thin Solid Films* **569**, 44-51 (2014).

149. Gordon, R.G. Criteria for Choosing Transparent Conductors. *MRS Bulletin* **25**, 52 (2000).

150. Dloczik, L. et al. Dynamic Response of Dye-Sensitized Nanocrystalline Solar Cells: Characterization by Intensity-Modulated Photocurrent Spectroscopy. *The Journal of Physical Chemistry B* **101**, 10281 (1997).

151. Park, J. et al. Panchromatic symmetrical squaraines: a step forward in the molecular engineering of low cost blue-greenish sensitizers for dye-sensitized solar cells. *Physical Chemistry Chemical Physics* **16**, 24173 (2014).

152. Chae, Y., Kim, S.J., Kim, J.H. & Kim, E. Metal-free organic-dye-based flexible dye-sensitized solar textiles with panchromatic effect. *Dyes and Pigments* **113**, 378 (2015).

153. Amasawa, E., Sasagawa, N., Kimura, M. & Taya, M. Design of a New Energy-Harvesting Electrochromic Window Based on an Organic Polymeric Dye, a Cobalt Couple, and PProDOT-Me2. *Advanced Energy Materials* **4**, 1400279 (2014).

154. Passoni, L. et al. Self-Assembled Hierarchical Nanostructures for High-Efficiency Porous Photonic Crystals. *ACS Nano* **8**, 12167-12174 (2014).

155. Yablonovitch, E. Inhibited Spontaneous Emission in Solid-State Physics and Electronics. *Physical Review Letters* **58**, 2059-2062 (1987).

156. Joannopoulos, J.D., Villeneuve, P.R. & Fan, S. Photonic crystals: putting a new twist on light. *Nature* **386**, 143-149 (1997).

157. John, S. Strong localization of photons in certain disordered dielectric superlattices. *Physical Review Letters* **58**, 2486-2489 (1987).

158. Sakoda, K. Optical Properties of Photonic Crystals (Springer, Berlin, 2005).

159. Galisteo-López, J.F. et al. Self-Assembled Photonic Structures. *Advanced Materials* **23**, 30-69 (2011).

160. Lee, J.-H., Singer, J.P. & Thomas, E.L. Micro-/Nanostructured Mechanical Metamaterials. *Advanced Materials* **24**, 4782-4810 (2012).

161. López, C. Materials Aspects of Photonic Crystals. *Advanced Materials* **15**, 1679-1704 (2003).

162. Smirnov, J.R.C., Calvo, M.E. & Míguez, H. Selective UV Reflecting Mirrors Based on Nanoparticle Multilayers. *Advanced Functional Materials* **23**, 2805-2811 (2013).

163. Yang, Q. et al. Bioinspired Fabrication of Hierarchically Structured, pH-Tunable Photonic Crystals with Unique Transition. *ACS Nano* **7**, 4911-4918 (2013).

164. Kim, M.H., Im, S.H. & Park, O.O. Rapid Fabrication of Two- and Three-Dimensional Colloidal Crystal Films via Confined Convective Assembly. *Advanced Functional Materials* **15**, 1329-1335 (2005).

165. Bonifacio, L.D., Lotsch, B.V., Puzzo, D.P., Scotognella, F. & Ozin, G.A. Stacking the Nanochemistry Deck: Structural and Compositional Diversity in One-Dimensional Photonic Crystals. *Advanced Materials* **21**, 1641-1646 (2009).

166. Wijnhoven, J.E.G.J. & Vos, W.L. Preparation of Photonic Crystals Made of Air Spheres in Titania. *Science* **281**, 802-804 (1998).

167. Colodrero, S., Ocana, M. & Miguez, H. Nanoparticle-Based One-Dimensional Photonic Crystals. *Langmuir* **24**, 4430-4434 (2008).

168. Colodrero, S., Ocaña, M., González-Elipe, A.R. & Míguez, H. Response of Nanoparticle-Based One-Dimensional Photonic Crystals to Ambient Vapor Pressure. *Langmuir* **24**, 9135-9139 (2008).

169. von Freymann, G., Kitaev, V., Lotsch, B.V. & Ozin, G.A. Bottom-up assembly of photonic crystals. *Chemical Society Reviews* **42**, 2528-2554 (2013).

170. Turner, D.R. Electropolishing Silicon in Hydrofluoric Acid Solutions. *Journal of The Electrochemical Society* **105**, 402-408 (1958).

171. Guo, D.-L., Fan, L.-X., Wang, F.-H., Huang, S.-Y. & Zou, X.-W. Porous Anodic Aluminum Oxide Bragg Stacks as Chemical Sensors. *The Journal of Physical Chemistry C* **112**, 17952-17956 (2008).

172. Unagami, T. Formation Mechanism of Porous Silicon Layer by Anodization in HF Solution. *Journal of The Electrochemical Society* **127**, 476-483 (1980).

173. Vincent, G. Optical properties of porous silicon superlattices. *Applied Physics Letters* **64**, 2367-2369 (1994).

174. Frohnhoff, S. & Berger, M.G. Porous silicon superlattices. *Advanced Materials* **6**, 963-965 (1994).

175. Singer, K.D. et al. Melt-processed all-polymer distributed Bragg reflector laser. *Opt. Express* **16**, 10358-10363 (2008).

176. Puzzo, D.P. et al. Color from colorless nanomaterials: Bragg reflectors made of nanoparticles. *Journal of Materials Chemistry* **19**, 3500-3506 (2009).

177. Floch, H.G., Priotton, J.-J. & Thomas, I.M. Optical coatings prepared from colloidal media. *Thin Solid Films* **175**, 173-178 (1989).

178. Thomas, I.M. Single-layer TiO2 and multilayer TiO2-SiO2 optical coatings prepared from colloidal suspensions. *Appl. Opt.* **26**, 4688-4691 (1987).

179. Steele, J.J., van Popta, A.C., Hawkeye, M.M., Sit, J.C. & Brett, M.J. Nanostructured gradient index optical filter for high-speed humidity sensing. *Sensors and Actuators B: Chemical* **120**, 213-219 (2006).

180. Schubert, M.F., Xi, J.Q., Kim, J.K. & Schubert, E.F. Distributed Bragg reflector consisting of high- and low-refractive-index thin film layers made of the same material. *Applied Physics Letters* **90**, 141115-3 (2007).

181. Parker, A.R. & Townley, H.E. Biomimetics of photonic nanostructures. *Nat Nano* **2**, 347-353 (2007).

182. Cunin, F. et al. Biomolecular screening with encoded porous-silicon photonic crystals. *Nat Mater* **1**, 39-41 (2002).

183. Fonzo, F.D. et al. Hierarchically organized nanostructured TiO 2 for photocatalysis applications. *Nanotechnology* **20**, 015604 (2009).

184. Dellasega, D. et al. Nanostructured Ag 4 O 4 films with enhanced antibacterial activity. *Nanotechnology* **19**, 475602 (2008).

185. Zhang, Z. et al. Microwave-Assisted Self-Doping of TiO2 Photonic Crystals for Efficient Photoelectrochemical Water Splitting. *ACS Applied Materials & Interfaces* **6**, 691-696 (2013).

186. Kobler, J., Lotsch, B.V., Ozin, G.A. & Bein, T. Vapor-Sensitive Bragg Mirrors and Optical Isotherms from Mesoporous Nanoparticle Suspensions. *ACS Nano* **3**, 1669-1676 (2009).

187. Varghese, L.T. et al. Enhanced Photon Management of Thin-Film Silicon Solar Cells Using Inverse Opal Photonic Crystals with 3D Photonic Bandgaps. *Advanced Optical Materials* **1**, 692-698 (2013).

188. Varghese, L.T. et al. Photonic Crystals: Enhanced Photon Management of Thin-Film Silicon Solar Cells Using Inverse Opal Photonic Crystals with 3D Photonic Bandgaps (Advanced Optical Materials 10/2013). *Advanced Optical Materials* **1**, 680-680 (2013).

189. Arsenault, A.C., Puzzo, D.P., Manners, I. & Ozin, G.A. Photonic-crystal full-colour displays. *Nat Photon* **1**, 468-472 (2007).

190. Hagfeldt, A. & Graetzel, M. Light-Induced Redox Reactions in Nanocrystalline Systems. *Chemical Reviews* **95**, 49-68 (1995).

191. Holliman, P.J., Jones, E.W., Connell, A., Furnell, L. & Davies, M.L. Photovoltaic product form and importance of colour. *Materials Research Innovations* **18**, 486-489 (2014).

192. Gálvez, F.E., Kemppainen, E., Míguez, H. & Halme, J. Effect of Diffuse Light Scattering Designs on the Efficiency of Dye Solar Cells: An

Integral Optical and Electrical Description. *The Journal of Physical Chemistry C* **116**, 11426-11433 (2012).

193. Colodrero, S. et al. Efficient Transparent Thin Dye Solar Cells Based on Highly Porous 1D Photonic Crystals. *Advanced Functional Materials* **22**, 1303-1310 (2012).

194. Heiniger, L.-P. et al. See-Through Dye-Sensitized Solar Cells: Photonic Reflectors for Tandem and Building Integrated Photovoltaics. *Advanced Materials* **25**, 5734-5741 (2013).

195. Anaya, M., Calvo, M.E., Luque-Raigón, J.M. & Míguez, H. Resonant Photocurrent Generation in Dye-Sensitized Periodically Nanostructured Photoconductors by Optical Field Confinement Effects. *Journal of the American Chemical Society* **135**, 7803-7806 (2013).

196. Guldin, S. et al. Dye-Sensitized Solar Cell Based on a Three-Dimensional Photonic Crystal. *Nano Letters* **10**, 2303-2309 (2010).

197. Halaoui, L.I., Abrams, N.M. & Mallouk, T.E. Increasing the Conversion Efficiency of Dye-Sensitized TiO2 Photoelectrochemical Cells by Coupling to Photonic Crystals. *The Journal of Physical Chemistry B* **109**, 6334-6342 (2005).

198. Lee, J. & Lee, M. Diffraction-Grating-Embedded Dye-Sensitized Solar Cells with Good Light Harvesting. *Advanced Energy Materials* **4**, n/a-n/a (2014).

199. Zhang, X., Liu, H., Huang, X. & Jiang, H. One-step femtosecond laser patterning of light-trapping structure on dye-sensitized solar cell photoelectrodes. *Journal of Materials Chemistry C* **3**, 3336-3341 (2015).

200. Lozano, G., Colodrero, S., Caulier, O., Calvo, M.E. & Míguez, H. Theoretical Analysis of the Performance of One-Dimensional Photonic Crystal-Based Dye-Sensitized Solar Cells. *The Journal of Physical Chemistry C* **114**, 3681-3687 (2010).

201. Colodrero, S. et al. Porous One-Dimensional Photonic Crystals Improve the Power-Conversion Efficiency of Dye-Sensitized Solar Cells. *Advanced Materials* **21**, 764-770 (2009).

202. Colodrero, S., Mihi, A., Anta, J.A., Ocaña, M. & Míguez, H. Experimental Demonstration of the Mechanism of Light Harvesting Enhancement in Photonic-Crystal-Based Dye-Sensitized Solar Cells. *The Journal of Physical Chemistry C* **113**, 1150-1154 (2009).

203. Colonna, D., Colodrero, S., Lindstrom, H., Di Carlo, A. & Miguez, H. Introducing structural colour in DSCs by using photonic crystals:

interplay between conversion efficiency and optical properties. *Energy & Environmental Science* **5**, 8238-8243 (2012).

204. Pendry, J.B. Symmetry and transport of waves in one-dimensional disordered systems. *Advances in Physics* **43**, 461-542 (1994).

205. Wong, T.-S. et al. Bioinspired self-repairing slippery surfaces with pressure-stable omniphobicity. *Nature* **477**, 443-447 (2011).

206. Ledesma-Aguilar, R., Nistal, R., Hernández-Machado, A. & Pagonabarraga, I. Controlled drop emission by wetting properties in driven liquid filaments. *Nat Mater* **10**, 367-371 (2011).

207. Mumm, F., van Helvoort, A.T.J. & Sikorski, P. Easy Route to Superhydrophobic Copper-Based Wire-Guided Droplet Microfluidic Systems. *ACS Nano* **3**, 2647-2652 (2009).

208. Pompano, R.R., Platt, C.E., Karymov, M.A. & Ismagilov, R.F. Control of Initiation, Rate, and Routing of Spontaneous Capillary-Driven Flow of Liquid Droplets through Microfluidic Channels on SlipChip. *Langmuir* **28**, 1931-1941 (2012).

209. Bahadur, V. et al. Predictive Model for Ice Formation on Superhydrophobic Surfaces. *Langmuir* **27**, 14143-14150 (2011).

210. Meuler, A.J., McKinley, G.H. & Cohen, R.E. Exploiting Topographical Texture To Impart Icephobicity. *ACS Nano* **4**, 7048-7052 (2010).

211. Boreyko, J.B. & Collier, C.P. Delayed Frost Growth on Jumping-Drop Superhydrophobic Surfaces. *ACS Nano* **7**, 1618-1627 (2013).

212. Kim, P. et al. Liquid-Infused Nanostructured Surfaces with Extreme Anti-Ice and Anti-Frost Performance. *ACS Nano* **6**, 6569-6577 (2012).

213. Lee, H., Alcaraz, M.L., Rubner, M.F. & Cohen, R.E. Zwitter-Wettability and Antifogging Coatings with Frost-Resisting Capabilities. *ACS Nano* **7**, 2172-2185 (2013).

214. Yan, Y.Y., Gao, N. & Barthlott, W. Mimicking natural superhydrophobic surfaces and grasping the wetting process: A review on recent progress in preparing superhydrophobic surfaces. *Advances in Colloid and Interface Science* **169**, 80-105 (2011).

215. Dorrer, C. & Ruhe, J. Drops on microstructured surfaces coated with hydrophilic polymers: Wenzel's model and beyond. *Langmuir* **24**, 1959-1964 (2008).

216. Giacomello, A., Meloni, S., Chinappi, M. & Casciola, C.M. Cassie-Baxter and Wenzel States on a Nanostructured Surface: Phase Diagram, Metastabilities, and Transition Mechanism by Atomistic Free Energy Calculations. *Langmuir* **28**, 10764-10772 (2012).

217. Cortese, B. et al. Superhydrophobicity due to the hierarchical scale roughness of PDMS surfaces. *Langmuir* **24**, 2712-2718 (2008).

218. Roach, P., Shirtcliffe, N.J. & Newton, M.I. Progess in superhydrophobic surface development. *Soft Matter* **4**, 224-240 (2008).

219. Deng, X. et al. Transparent, Thermally Stable and Mechanically Robust Superhydrophobic Surfaces Made from Porous Silica Capsules. *Advanced Materials* **23**, 2962-2965 (2011).

220. Deng, X., Mammen, L., Butt, H.J. & Vollmer, D. Candle Soot as a Template for a Transparent Robust Superamphiphobic Coating. *Science* **335**, 67-70 (2012).

221. Park, H.K., Yoon, S.W. & Do, Y.R. Superhydrophobicity of 2D SiO2 hierarchical micro/nanorod structures fabricated using a two-step micro/nanosphere lithography. *Journal of Materials Chemistry* **22**, 14035-14041 (2012).

222. Park, K.-C. et al. Nanotextured Silica Surfaces with Robust Superhydrophobicity and Omnidirectional Broadband Supertransmissivity. *ACS Nano* **6**, 3789-3799 (2012).

223. Kota, A.K., Li, Y.X., Mabry, J.M. & Tuteja, A. Hierarchically Structured Superoleophobic Surfaces with Ultralow Contact Angle Hysteresis. *Advanced Materials* **24**, 5838-5843 (2012).

224. Feng, J., Tuominen, M.T. & Rothstein, J.P. Hierarchical Superhydrophobic Surfaces Fabricated by Dual-Scale Electron-Beam-Lithography with Well-Ordered Secondary Nanostructures. *Advanced Functional Materials* **21**, 3715-3722 (2011).

225. Guo, Z., Chen, X., Li, J., Liu, J.H. & Huang, X.J. ZnO/CuO Hetero-Hierarchical Nanotrees Array: Hydrothermal Preparation and Self-Cleaning Properties. *Langmuir* **27**, 6193-6200 (2011).

226. Criante, L. et al. 95580O-95580O-12 (2015).

227. Holzwarth, U. & Gibson, N. The Scherrer equation versus the 'Debye-Scherrer equation'. *Nat Nano* **6**, 534-534 (2011).

228. Halme, J., Vahermaa, P., Miettunen, K. & Lund, P. Device Physics of Dye Solar Cells. *Advanced Materials* **22**, E210-E234 (2010).